Dynamics of corner flows driven by wettability

Vom Fachbereich Maschinenbau
an der Technischen Universität Darmstadt
zur
Erlangung des Grades eines Doktor-Ingenieurs (Dr.-Ing.)
genehmigte

D i s s e r t a t i o n

vorgelegt von

Vignesh Thammanna Gurumurthy, M.Sc.

aus Chennai, India

Berichterstatter:	Prof. Dr.-Ing. Cameron Tropea
Mitberichterstatter:	Prof. Stephen Garoff
	Apl. Prof. Dr.-Ing. Ilia V. Roisman
Tag der Einreichung:	18.06.2014
Tag der mündlichen Prüfung:	24.08.2018

Darmstadt 2018
D17 (Diss. Darmstadt)

Thammanna Gurumurthy, Vignesh:
Dynamics of corner flows driven by wettability
Jahr der Veröffentlichung der Dissertation auf TUprints: 2018
URN:urn:nbn:de:tuda-tuprints-80565
Tag der mündlichen Prüfung:24.08.2018

To my parents
Sivasakthi *and* ***Gurumurthy***

Abstract

Capillary driven flows in confined spaces such as grooves, microchannels and in polygonal containers arise in numerous contexts found in microfluidic devices, porous media, coating of textured surfaces, etc. The interior corners in these geometries enhance the capillary effects resulting in the rise of rivulets in the corner. These rivulets are known to affect the performance of the devices simply by influencing the amount of liquid in different regions of the channel or groove. Understanding the behaviour and optimizing the performance in aforementioned applications requires quantitative modelling of the dynamics of capillary flows in corners.

The objective of this thesis is to understand the dynamics of fluid flows in the corners, and their influence on the bulk flow using numerical simulations and theoretical analyses. Within this framework, three studies investigating the spontaneous and forced wetting flows in two model geometries under the influence of gravity are carried out. The spontaneous wetting of rivulets in the interior corners of a square capillary is investigated using numerical simulations. The shape of the rivulet and the flow inside the rivulet is also studied using lubrication theory. The spontaneous rise in an array of connected open rectangular channels is studied using numerical simulations. Here, the dynamics of fluid flow inside the channel (bulk flow), on the outer face and on the outer corner are also investigated, in addition to the rivulets inside the channel. The dynamics of bulk flow are compared with the capillary rise model extended for the open channels. Two types of forced wetting - immersion and pumping - are investigated in a square capillary, where the behavior of the bulk flow and the rivulet in the corner are studied separately.

Results from the spontaneous wetting simulations in both geometries show that at long times, the rivulets rise according to the one-third power-law, and their rise rate is weakly dependent on the geometry. A similarity solution is obtained using the lubrication approximation of the flow inside the rivulet, which matches the simulations in describing the rivulet profile. Also, a scaling relation based on the similarity solution for the non-dimensional growth rate is proposed. The simulations in the open

rectangular channel reveals that the typical cusp formation at the outer corner smoothens out when the channel dimensions are smaller than the capillary length of the liquid. In addition, the simulations also highlight the limitations of the capillary rise model when extended to describe the bulk flow in open channels, and also indicate the similarities between the spontaneous wetting of the outer face and a planar wall. The forced wetting experiments of the bulk flow reveals that the liquid column starts falling down at a steady speed, which is predicted by the extended capillary rise model with sufficient accuracy. The rivulets under forced wetting reaches a fixed length, which decreases with increasing capillary number, eventually leading to air entrainment. The lubrication approximation for the rivulet flow is able to predict its shape accurately.

Kurzfassung

Von Kapillarkräften getriebene Strömungen in Rillen, Mikrokanälen und mehreckigen Behältnissen treten in vielfältingen Anwendungen der Mikrofluidik auf, so z.B. in porösen Medien oder während der Beschichtung konturierter Oberflächen. Konkave Ecken dieser Geometrien verstärken den Kapillareffekt und führen zu einer verstärkten Rinnsalströmung entlang der Ecken.Es ist bekannt, dass diese Rinnsale das Verhalten der spezifischen Anwendung beeinflussen, da sie zu einer ungleichmäßigen Verteilung der Flüssigkeit in verschiedenen Bereichen führen.

Daher ist das Verständnis kapillargetriebener Strömungen in Mikrokanälen und Rillen von entscheidender Bedeutung für die Auslegung der zuvor genannten Anwendungen, und bildet das Ziel der hier vorliegenden Arbeit.Im Rahmen dieser Arbeit werden drei verschiedene Studien zur Strömung während der spontanen und erzwungenen Benetzung in zwei verschiedenen Modellgeometrien durchgeführt. Zunächst wird die spontane Benetzung in den Ecken einer quadratischen Kapillare unter Einfluss der Gravitation numerisch untersucht. Dabei werden die Form der Rinnsale sowie die Fluidströmung im Inneren eines Rinnsals basierend auf der Schmierfilmannäherung beschrieben. Dann wird die spontane Benetzung innerhalb einer Anordnung von miteinander verbundenen rechteckigen Kanälen wird numerisch untersucht. Hierbei werden neben der Ausbreitung der Rinnsale innerhalb der Ecken der Kanäle auch die Fluidströmung in den Kanälen sowie an deren Außenseiten und äußeren Ecken untersucht. Die Strömung innerhalb der Kanäle wird dabei mit der Theorie zum Flüssigkeitsanstieg innerhalb einer Kapillare, die für offene Kanäle erweitert wurde, verglichen. Das Verhalten eines Rinnsals in den Ecken sowie die Strömung im Zentrum einer Kapillare während der erzwungenen Benetzung werden separat mithilfe von Experimenten, Simulationen und theoretisch untersucht.

Ergebnisse der Simulationen zur spontanen Benetzung in beiden Geometrien zeigen, dass der Anstieg der Rinnsale über lange Zeiten dem Ein-Drittel Potenzgesetz folgt, wobei die Anstiegsrate dabei nur schwach von der Geometrie beeinflusst wird. Eine auf der Schmierfilmtheorie basieren-

den Ähnlichkeitslösung für die Strömung innerhalb eines Rinnsals ist in guter Übereinstimmung mit den Simulationsergebnissen. Basierend auf der Ähnlichkeitslösung wird außerdem ein Skalierungsgesetz für die dimensionslose Anstiegsrate vorgeschlagen. Die Simulationen der Strömung im offenen rechteckigen Kanal zeigen zusätzlich, dass sich die typische Meniskus-Spitzen an den äußeren Ecken glätten, wenn die Kanalbreite kleiner ist, als die kapillare Länge der Flüssigkeit. Weiterhin werden in den Simulationen sowol die Modell-Limits des Kapillaranstiegs abgebildet als auch die Ähnlichkeiten zwischen der spontanen Benetzung einer äußeren Kanalwand und einer ebenen Oberfläche. Die Experimente zur erzwungenen Benetzung zeigen, dass sich die Flüssigkeitssäule mit einer konstanten Geschwindigkeit absenkt, was auch mithilfe des erweiterten Modells zum Anstieg in einer Kapillare mit ausreichender Genauigkeit beschrieben werden kann. Die Rinnsale erreichen im Falle der erzwungener Benetzung eine konstante Länge, welche mit zunehmender Kapillarzahl abnimmt, wobei eine zunehmende Kapillarzahl zu Lufteinschlüssen führen kann. Die Schmierfilmannäherung erlaubt also eine genaue Vorraussage der Strömung und From der Rinnsale.

Acknowledgements

Four years ago, I embarked upon a journey into the world of scientific research, which is nearing its end, and it is time to thank everyone who have supported, motivated and guided me to reach the end.

First, I would like to thank **Apl. Prof. Tatiana Gambaryan-Roisman** for informing me about this PhD position, when i contacted her. I also thank the Marie-Curie funding program, *Complex Wetting* (**CoWet**) an Initial Training Network for providing the fellowship.

I sincerely thank **Prof. Cameron Tropea** for providing a stimulating environment to carry out research. I really appreciate his prompt response in reading the manuscripts and providing critiques, which has improved my writing skill.

I am grateful to have **Apl. Prof. Ilia V. Roisman** as my supervisor, who kept his office doors open for discussions at any time. The innumerable discussions we had on research, has greatly helped me to improve my analytical and presentation skills. I really appreciate your immense patience at the beginning, and also for generously extending my contract after the end of the fellowship.

I also like thank **Prof. Stephen Garoff** (Carnegie Mellon University) for guiding with the research. At the end of every Skype discussion, my insecurities and reluctance when delving into a new topic dissolves. I am amazed at the meticulousness you show into each topic no matter how small it is, and after working with you it has imbibed into me as well.

This work would not have been possible without **Daniel Rettenmaier** who shared his code and also provided his assistance whenever needed. I also thank my ex-colleagues **Nicklas Linder** and **Daniel Kintea** for helping me in learning OpenFOAM at the start.

It is generally said that the environment plays a huge role in shaping a person. In my case, during this four years, it happened through my colleagues: **Markus Schremb**, **Benjamin Krumbien**, **Hannah Kittel**, **Sebastian Brulin** , **Lucas Kutlej**. I cherish the informal discussions we

had at several venues: at your office, common kitchen, Biergarten, etc.

Special thanks to **Daniel Rettenmaier** and **Markus Schremb** for translating the abstract into German. I also thank **Sebastian Brulin**, **Ramakrishnan A. Sankaran** and **Abhijeet Kumar** for proof reading the thesis.

I would also like to thank our institute secretaries **Birgit Neuthe** and **Stephanie Lath** for assisting me with the bureaucratic activities. Special thanks to **Monika Medina**, our CoWet coordinator, for helping me in several administrative tasks.

The several workshops that I attended in different countries organised by CoWet, provided me an opportunity to interact with several experts - **Prof. Hans Jurgen Butt**, **Pierre Collinet**, **Prof.Günter K. Auernhammer** which gave me a perspective into different research topics and also served as a platform for networking.

Friends are the family you choose, and in Germany I am fortunate to have found **Ramji**, **Raja**, **Sharan**, **Abhijeet**, **Ehsan Arun** and **Divya** as friends, who have always motivated me and provided moral support.

Everything I have accomplished till this date is entirely due to my parents upbringing. I would like to thank especially my mother **Sivasakthi Gurumurthy** for being a pillar of support in the past three years despite going through the hardships that she faced in India all alone after the sudden demise of my father.

Nomenclature

Latin Letters, upper case

Symbol	Description	Unit
A	Constant	-
B	Friction coefficient	-
Bo	Bond number	-
Ca	Capillary number	-
Co	Courant number	-
D	Depth of the channel	m
E	Surface free energy	J
F	Outer face width	m
F_σ	Capillary force	N
F_P	Force due to pressure loss	N
F_a	Force due to added mass	N
F_μ	Viscous friction	N
F_g	Gravitational force	N
K	Non-dimensional rivulet growth rate	-
M_r	Mass of the rivulet	kg
Oh	Ohnesorge number	-
P	Pressure field	N/m^2
R	Radius of curvature	m
Re	Reynolds number	-
R_o	Radius of curvature of the bulk meniscus	m

Symbol	Description	Unit
S	Spreading parameter	-
S_r	Surface area of the rivulet	m^2
$\mathbf{S_p}$	cell-face surface normal vector	m
T	Time in the new coordinate	s
$\mathbf{U}$	Velocity field	m/s
U_a	speed of the meniscus/liquid column	m/s
U_o	external forcing speed	m/s
We	Weber number	-
W	Width of the channel	m

Latin letters, lower case

Symbol	Description	Unit
a	capillary length	m
$b_1,\ b_2$	constant coefficients	variable dependent
c	fitting coefficient	-
$c_1,\ c_2$	constant coefficients	variable dependent
$\mathbf{d}$	distance vector	m
f_o	average frequency of molecular displacements	Hz
g	acceleration due to gravity	m/s^2
h	meniscus height	m
h_a	height of the liquid column above the pool	m
h_o	equilibrium height	m
h_b	height of the liquid column below the pool	m
k	viscous friction coefficient	-
l_o	outer length scale characterizing the geometry	m
l_s	slip length	m
m	mass of the liquid column	kg
$\mathbf{n}$	unit interface normal	-
$\mathbf{n}_w$	unit wall normal	-
r	radius of the capillary	m
r_s	roughness of the surface	m
U	forcing speed	m/s
w	capillary width	m
$\mathbf{x}$	vertex vector	m
$\mathbf{x_p}$	position vector	m

Greek Letters

Symbol	Description	Unit
α	inner corner half-angle	[deg]
α_o	outer corner half-angle	[deg]
γ	volume fraction	-
δ	rivulet thickness	m
δ_o	rivulet thickness close to the bulk meniscus	m
ϵ	channel aspect ratio	-
θ_{eq}	equilibrium contact angle	[deg]
θ_s	microscopic contact angle	[deg]
θ_D	apparent contact angle	[deg]
θ_A	static advancing contact angle	[deg]
θ_R	static receding contact angle	[deg]
θ_{eq}	equilibrium contact angle	[deg]
κ	curvature	m^{-1}
μ	viscosity	Pa s
ϕ	variable	variable dependent
σ	surface tension	N/m
ρ	density	kg/m^3

Abbreviations

Abbrevation	Description
AMR	Adaptive Mesh Refinement
CFD	Computational Fluid dynamics
CSF	Continuum Surface Force model
DNS	Direct Numerical Simulation
FVM	Finite Volume Method
HT	Hydrodynamic Theory
MKT	Molecular Kinetic Theory
MPI	Message Passing Interface
MS-P	Meyer Stowe-Princen theory
MULES	Mutli-dimensional Universal Limiter of Explicit Solution
PDMS	Polydimethylsiloxane
PISO	Pressure-Implicit Split Operator
PLIC	Piecewiese Linear Interface Calculation
VOF	Volume-of-Fluid method

Contents

To study, and when the occasion arises to put what one has learned into practice - is that not deeply satisfying ?

Confucius, Analects 1.1.1

1 Introduction

1.1 Motivation

Flows driven by surface tension are called as capillary flows. We often come across them in our daily life whenever we write with a pen, clean a surface with a towel, watch water drops rolling over glass windows, etc. These events are so familiar that we fail to take notice their intricate complexity. A close observation of such events will show that they typically involve the spreading of a liquid over a solid surface, where it displaces another liquid or gas as it moves.

The study of spreading of liquids on a solid substrate is called wetting. Wetting processes are identified by the contact line, which is the boundary where the three phases meet or the line that separates wet and dry regions. A water drop placed on a clean glass surface spreads into a film, while the same drop on a plastic surface forms a spherical cap. This simple example clearly illustrates the multi-scale nature of the wetting processes, i.e., the adhesive and cohesive interactions between the three phases at the molecular level, occurring in the vicinity of the contact line, affects the hydrodynamics of the entire process. It plays a huge role in a wide range of applications related to fields such as coating, porous media, microfluidics, etc.

The spreading of liquids observed in these applications can be entirely spontaneous (driven by capillary action) or forced (driven by external means). Also, the different forms of wetting processes observed in the aforementioned applications typically fall into two categories. The first category involves liquids spreading on open surfaces such as drop spreading on a substrate, liquid film rising over a surface, etc. Liquids spreading in confined spaces - inside thin tubes, channels, slits or wedges - comes under the second category. The fluid flows in the second category is of specific interest in the present study and its importance is stressed using the following examples.

- In **microfluidics**, passive driving of the liquid by capillary action is

often preferred over conventional means like micro-pumps or other alternatives such as electrowetting, since it requires no additional equipment. For instance, applications related to disposable diagnostic systems used in healthcare industries are made affordable using capillary action [1, 2].

- Under zero-gravity conditions, where capillary forces are dominant, holding the liquid at the bottom of the tanks or in a coffee cup in spacecraft, becomes a challenging issue. In such cases, corners are used actually to guide the liquid in the preferred direction.
- In the case of **porous media**, where the pores are of different shapes with varying corner geometries, the fluid imbibition is influenced significantly by the flows in the corners of the pores [3–7].
- In applications like gravure printing [8] and in printing of electronic circuits, the flow observed in textured surfaces can be conceptually modelled as a network of parallel, connected channels of different cross-sections. Moreover, the flow over a rough surface can be understood by modelling it as a flow over a network of interlocking grooves.

Thus, understanding the behaviour of the capillary driven flows in confined spaces is crucial in the design of a multitude of applications. Fundamentals of wetting is essential for understanding capillary driven flows, which is reviewed in the next section.

1.2 Fundamentals of wetting

The degree of interaction between the three phases during wetting is characterized by contact angle, which is defined as the angle between the tangent to the liquid-gas interface and the solid surface at the contact line (see Figure 1.1). In the following subsections, an overview of the statics and the dynamics of wetting are presented.

1.2.1 Young-Laplace equation

The Young-Laplace equation relates the pressure difference ΔP across the interface between two static fluids to the shape of the interface, i.e., its curvature. It is the result of the normal stress balance at the interface

between the fluids at rest,

$$\Delta P = \sigma \left(\frac{1}{R_1} + \frac{1}{R_2} \right). \tag{1.1}$$

Here, σ is the surface tension, R_1 and R_2 are the principal radii of curvature.

1.2.2 Statics: Definition of equilibrium contact angle

Young's equation for ideal substrates Consider a liquid drop at rest on a smooth, flat, and chemically homogeneous solid substrate as shown in the Figure 1.1. At equilibrium the force balance at the contact line yields,

$$\sigma_{SG} - \sigma_{SL} = \sigma \cos \theta_{eq}. \tag{1.2}$$

The variables σ_{SL}, σ_{SG} are the interfacial tensions of the solid-liquid

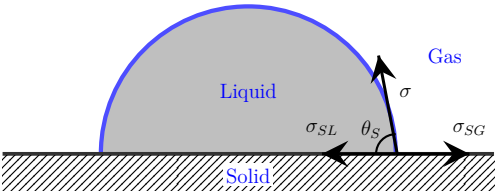

Figure 1.1: Force balance at the contact line.

and solid-gas interfaces respectively. This equation which relates the three interfacial tensions, is also called Young's equation and the term θ_{eq} refers to the equilibrium contact angle.

A drop placed on a substrate either spreads into a film or forms a spherical cap. These two states can be theoretically identified by the spreading parameter S. It is defined as the difference in surface energy of the substrate when dry (σ_{SG}) and wet ($\sigma_{SL} + \sigma$):

$$S = \sigma_{SG} - (\sigma_{SL} + \sigma) = \sigma(\cos \theta_{eq} - 1) \tag{1.3}$$

When $S \geq 0$, the drop spreads completely forming a thin film, or when $S < 0$, a spherical cap results. These two states are often referred as complete wetting and partial wetting states. When $\theta_{eq} \leq \pi/2$, the substrate is said to be "mostly wetting", and "mostly non-wetting" when $\theta_{eq} > \pi/2$.

On rough surfaces: contact angle hysteresis The ideal substrate assumed when deriving the Young's equation (1.2) never exists in reality; even the cleanest, smoothest solid surfaces are contaminated and rough to a certain degree. The manifestation of such spatial and chemical inhomogeneities results in contact angle hysteresis, i.e., an interval of contact angles $[\theta_A,\ \theta_R]$ in which the drop is in static equilibrium, instead of the unique value θ_{eq} predicted by Young's equation (1.2). This range of contact angles is called the hysteresis of the surface.

The hysteresis can be quantified by either inflating or deflating a drop placed on substrate from the bottom. During this process, the stationary drop after reaching a critical volume, starts to move. The angle at which it starts to advance is called the static advancing angle θ_A, and the angle at which it starts to recede is called the static receding angle θ_R.

The effect of roughness on the statics of wetting can be understood using the Wenzel and Cassie-Baxter models, which are explained below.

Wenzel model for rough substrates On a rough but chemically homogeneous surface, the equilibrium contact angle can be defined using Wenzel model. Consider a liquid drop at rest on a rough substrate as shown in the Figure 1.2. The roughness of the substrate is characterized by the parameter r_s, which is the ratio of actual surface area to the projected area of contact made with the substrate by the drop. For smooth surfaces $r_s = 1$, and $r_s > 1$ for rough surfaces. Minimizing the change in surface energy of this system when the drop moves a small distance shows,

$$\cos\theta^* = r_s \cos\theta_{eq}. \tag{1.4}$$

Here, θ^* is contact angle measured on the rough surface. Thus the above equation (1.4) shows that the roughness amplifies the substrate wettability.

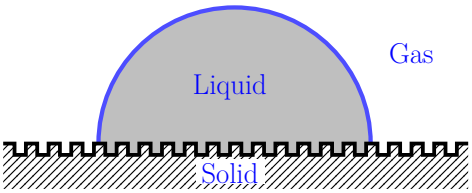

Figure 1.2: Wenzel state: Drop on a rough surface.

Cassie-Baxter model for chemically heterogeneous substrates On a smooth, chemically heterogeneous substrate, the equilibrium contact angle is defined using the Cassie-Baxter model. Assume a substrate made of two chemical species having contact angles θ_1 and θ_2 (see Figure 1.3). The fractional surface area of the liquid resting on each species is taken as f_1 and f_2 respectively. Note, $f_1 + f_2 = 1$ or in general for substrate made of several species, $\sum f_i = 1$. Minimizing the surface energy of the system when the drop moves a small distance, the contact angle θ^* on the rough surface can be related to the substrate wettability as,

$$\cos\theta^* = f_1 \cos\theta_1 + f_2 \cos\theta_2. \tag{1.5}$$

Thus the contact angle in a chemically heterogeneous substrate is the sum

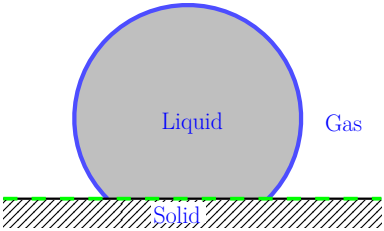

Figure 1.3: Cassie-Baxter state: Drop on a chemically heterogeneous substrate.

of the cosines of the corresponding angles weighted by their corresponding surface fractions.

1.2.3 Dynamics of wetting

When the contact line moves equation (1.2) is no longer satisfied, since there is an unbalanced force associated with the viscous drag near the contact line. Thus, the process of studying the dynamics of wetting boils down to identifying the relationship between the dynamic contact angle θ_D and the speed u with which the contact line moves relative to the substrate.

The commonly used systems for studying dynamic wetting are spontaneous spreading of a drop on a substrate, pushing liquid inside a capillary with a piston, pushing or pulling a vertical plate or fibre into or out of

a liquid pool. These experiments reveal that the contact angle increases when the contact line is advancing, and decreases when it is receding, indicating that this process is dissipative.

Depending upon the mode of dissipation accounted close to the moving contact line, two main theories can be identified: hydrodynamic theory (HT) and molecular kinetic theory (MKT). Before reviewing the dynamics of wetting, the non-dimensional numbers commonly used in wetting are defined in the Table 1.1 given below.

Table 1.1: Commonly used list of non-dimensional numbers in wetting.

Dimensionless number	Definition	Formula
Reynolds number (Re)	$\frac{\text{inertia}}{\text{viscous force}}$	$\frac{\rho u l}{\mu}$
Capillary number (Ca)	$\frac{\text{viscous force}}{\text{capillary force}}$	$\frac{\mu u}{\sigma}$
Weber number (We)	$\frac{\text{inertia}}{\text{capillary force}}$	$\frac{\rho u^2 l}{\sigma}$
Bond number (Bo)	$\frac{\text{gravitational force}}{\text{capillary force}}$	$\frac{\rho g l^2}{\sigma}$
Ohnesorge number (Oh)	$\frac{\text{viscous force}}{\text{inertia+capillary forces}}$	$\frac{\mu}{\sqrt{\rho \sigma l}}$

Note, here l and u are the characteristic length scale and velocity scale, which depend upon the given problem. The terms ρ, μ indicate the density and the viscosity of the liquid respectively.

1.2.3.1 Hydrodynamic theory

Approximating the contact line motion by a wedge flow and applying the no-slip boundary condition will result in a discontinuity in the velocity at the contact line i.e, the velocity becomes multivalued. This discontinuity causes the viscous stress $\mu u/(\theta x)$ to diverge and the rate of viscous dissipation $(\mu u^2/\theta) \ln x$ to become non-integrable at the contact line $x = 0$. Thus an infinite force is required to move the contact line; in Huh and Scriven's words [9] *Not even Herakles could sink a solid.* This singularity is mathematical; in reality the liquid moves freely on the substrate.

This stress singularity is overcome artificially either by introducing a slip or cutting off the region close to the solid and limiting the solution only above this length. While this solution overcomes the stress singularity, the pressure is still logarithmically diverging at the contact line. Assuming a precursor film of nanoscopic thickness, moving in front of the contact line avoids the notion of contact line, thereby avoiding its associated singularities. But the precursor films have been observed only in spreading of volatile liquids and in complete wetting surfaces [10].

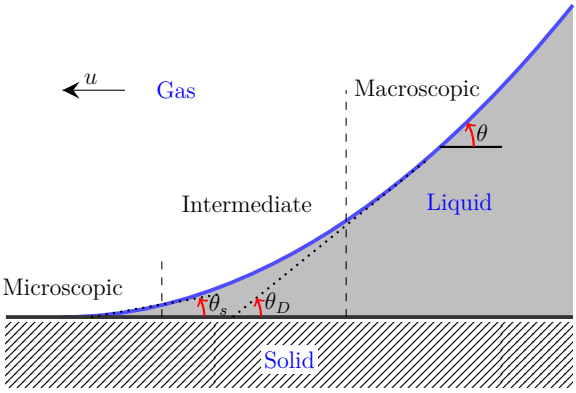

Figure 1.4: Schematic showing the three regions in the vicinity of a moving contact line.

For slow contact line motion ($Ca \ll 1$), the hydrodynamic theory considers three regions in the moving wedge [11]: microscopic, intermediate and macroscopic as shown in the Figure 1.4. In the microscopic (inner) region, a wedge flow is assumed and the interface is planar, where the angle it makes with the wall can be taken the static contact angle θ_s. In the intermediate region, the interface deforms due to viscous bending, and the flow in this region is described by applying lubrication approximation. In the macroscopic (outer) region, the interface is unaffected by the viscous forces and depends on the geometry of the system. Both the inner and intermediate regions are independent of the geometry. Matching the individual asymptotic solutions in these three regions yields [12],

$$G(\theta) = G(\theta_s) + Ca \left[\ln \left(\frac{l_o}{l_s} \right) + (Q_i - Q_o) \right], \tag{1.6}$$

where

$$G(\theta) = \int_0^{\theta} \frac{x - \sin x \cos x}{2 \sin x} dx. \tag{1.7}$$

The terms l_o, l_s are the typical length scales which characterize the macroscopic and the microscopic regions respectively. The parameters Q_i and Q_o depend on the inner scale model and the geometry of the problem respectively. The solution provided by equation (1.6) describes the shape of interface in the intermediate region and its overlap with the inner and outer regions. It is valid when the viscosity of the displaced fluid is negligible compared with the liquid. Experiments [13] have confirmed that this solution (1.6) accurately describes the interface shape up to 200 μm from the contact line for $Ca \leq 0.1$.

A simplified form of the solution often used in applications can be obtained from equation (1.6) for $\theta < 3\pi/4$ [14], which is given below

$$\theta_D^3 = \theta_s^3 + 9Ca \ln\left(\frac{l_o}{l_s}\right). \tag{1.8}$$

Here, the term θ_D refers to the apparent contact angle as shown in Figure 1.4, which is usually calculated by extrapolating the static shape of the interface all the way down to the substrate. As observed in [10], this definition of apparent contact angle is limited to systems, where a static shape of the interface is available, such as meniscus in a capillary, meniscus near a cylindrical rod/fibre or a flat plate, semi-circular drop. In other cases (such as drop impact, liquid bridges, early stage of drop spreading), the apparent contact angle is obtained using the tangent to the interface at the contact line, which is resolution dependent.

1.2.3.2 Molecular kinetic theory

The molecular kinetic theory is based on a statistical description of the transport process developed by Eyring and co-workers [15, 16]. In this approach, the contact line moves by small jumps induced by thermal fluctuations, and these jumps depend on the net frequency f of the forward and backward molecular displacements within the three phase region. For the contact line to advance, the molecular displacements in the forward direction must be higher than in the backward direction. The driving force for the contact line is the unbalanced capillary force $F = \sigma(\cos\theta_S - \cos\theta_D)$.

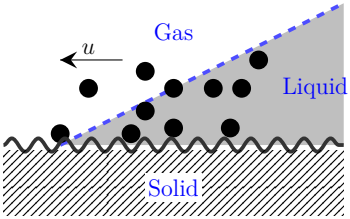

Figure 1.5: Schematic showing the molecular displacements in the vicinity of a moving contact line.

Equating this unbalanced work per unit length to the work required for molecular displacement results in the expression,

$$u = 2f_o\lambda \sinh\left[\frac{\sigma(\cos\theta_s - \cos\theta_D)}{2nkT}\right] \tag{1.9}$$

The terms f_o, λ, k and T represent the average displacement frequency, molecular displacement at equilibrium, Boltzmann constant and the absolute temperature respectively. If the argument of the sinh function is small, it predicts a linear dependence, conversely an exponential dependence for higher contact angles.

1.2.3.3 Other models and empirical correlations

The MKT model is limited to small capillary numbers, close to the threshold of depinning, where the molecular-scale processes are dominant [17]. Beyond this threshold, the contact line motion is dominated by the dissipation in the bulk, which is best described by the hydrodynamic theory. Several studies [13, 17, 18] show that the microscopic contact angle is also velocity dependent, which is assumed constant in HT.

Combining the two models seems to agree with a wide range of experiments as well as addressing their drawbacks. Among the several hybrid models proposed in the literature, two variants are popular. The first one [18] considers the that velocity dependent microscopic contact angle is described by MKT in hydrodynamic theory, while the second one [19] combines the two modes of dissipation at the contact line to describe the dynamic contact angle.

In addition to theories described above, there are several empirical cor-

relations, which relate the apparent contact angle to the capillary number. Hoffman [20] studied experimentally the apparent contact angle of the advancing liquid in capillary for wide range of speeds ($4 \times 10^{-5} < Ca < 36$). He showed that the apparent contact angle can be correlated as a function of capillary number plus a shift factor, which depends on the microscopic contact angle, when the capillary and visocus forces are the dominant factors controlling the system. Two different correlations based on Hoffman's data are commonly used in the literature, which are given below.

Jiang's Correlation [21]: Fitting Hoffman's data with the least-squares method results in the equation of the form,

$$\frac{\cos\theta_s - \cos\theta_D}{\cos\theta_s + 1} = \tanh\left(4.96 Ca^{0.702}\right) \tag{1.10}$$

Kistler's Correlation [22]: It is obtained by fitting Hoffman's data exclusively for completely wetting systems with high liquid viscosities, and slightly modified to improve the fit at large Ca values. This fit can also be used for partially wetting systems in the same fashion like the shift-factor introduced by Hoffman [20]. The equation is of the form,

$$\theta_D = f_{Hoff}\left[Ca + f_{Hoff}^{-1}\right], \tag{1.11}$$

where

$$f_{Hoff}\left(Ca\right) = \cos^{-1}\left\{1 - 2\tanh\left[5.16\left(\frac{Ca}{1 + 1.31 Ca^{0.99}}\right)^{0.706}\right]\right\} \tag{1.12}$$

When $Ca < O(0.1)$, equation (1.11) reduces to the form $\theta_D^3 \approx Ca$ for $\theta = 0^\circ$ which is the functional dependence of hydrodynamic theory.

Accounting for contact angle hysteresis The above dynamic contact angle models derived for an ideal substrate can be used for real surfaces by adopting the following convention. For surfaces with hysteresis, θ_A is used instead of θ_s for advancing contact line and θ_R instead of θ_s for receding contact line.

1.3 Capillary rise

Capillary driven flows in confined spaces occur mainly due to the combined influence of the geometry and the capillary forces. Depending upon the context of application studied, these flows are often referred as capillary rise or imbibition or wicking. In this section, the theory behind the rise and an overview of the related studies are presented.

1.3.1 Historical observations

The first observation of capillary rise dates back to Leonardo Da Vinci (1452-1719) [23], who recorded in his notes that the mountain springs are due to a network of capillaries capable of lifting water. Nearly two centuries later, Jacques Rohalt (1620-1675) [23] interpreted that the rise of liquids in narrow tubes is due to the vacuum created by the inability of air to invade the tubes. In the same century, the astronomer Gemniniano Montanari compared the rise of liquids to that of a sap in plant. The astronomer Giovanni Borelli (1608-1679)[23] demonstrated that the maximum height reached by the liquid is inversely proportional to the tube size.

The first systematic study of capillary rise was made by Francis Hauksbee [24–26], who carried out a series of experiments in glass capillaries, between two flat plates and in wedges, using coloured liquids. Based on the observations, he concluded the following:

- The capillary effect is not specific to cylindrical capillaries; it can also be observed in other geometries such as a wedge or between two flat plates separated by a small distance.
- The rise of liquids is due to the liquid's affinity to the solid walls. The liquids also rise in tubes when they are kept in vacuum, which refutes Rohault's theory.
- Thickness of the capillary has no influence on the rise inside the tube.

In 1710, the mathematician Brook Taylor [27] also confirmed Hauksbee's observations that the shape of the liquid rising in a wedge is a hyperbola. James Jurin [28] showed that the maximum height of the liquid ascent is inversely proportional to their radii. Newton also discussed Hauksbee's observations in his 31^{st} query of his famous treatise *Opticks*

[29].

While these early observations attribute the ascent of liquid in capillaries to the attraction with solid walls, a complete physical explanation was possible only after the Young-Laplace theory, put forward by Thomas Young [30] and Pierre Simon Laplace [31] in 1806. They related the pressure difference across the interface between two fluids to its shape.

1.3.2 Rise in cylindrical capillaries

As stated in section 1.3.1, the capillary rise were first analysed thoroughly for the cylindrical capillary, and extended to other geometries in the last decade. Both the statics and dynamics of rise are explained here using cylindrical capillary as a model geometry.

When a capillary is put into contact with a bath of wetting liquid ($\theta < \pi/2$), the free surface of the liquid touching the walls of the capillary depress, forming a meniscus. The low pressure formed due to the meniscus sucks the liquid into the capillary leading to a rise, which eventually reaches equilibrium where it attains a fixed height.

1.3.2.1 Statics

Theoretically, using the affinity of the liquid to the solid, the condition for the rise can be written as,

$$I = \sigma_{SG} - \sigma_{SL} \tag{1.13}$$

The above equation defines the difference in surface energy of the solid when it is dry and wet by a liquid. This condition for the rise is often referred as the imbibition criteria. The liquid rises in the capillary when $I > 0$ and falls below its initial level when $I < 0$. The above equation can be simplified using Young's relation (1.2), which gives $I = \sigma \cos\theta$. Thus the condition for rise is $\theta < 90°$.

The maximum height reached by the liquid is also called the equilibrium height h_o since the rising liquid eventually comes to rest, when the forces are balanced. This height is measured from the free surface of the pool to the lowest point of the meniscus in the center of the capillary (see Figure 1.6). Balancing the capillary force with the weight of the liquid gives the equilibrium height.

For a cylindrical capillary of radius r as shown in the Figure 1.6, the equilibrium height is,

$$h_o = \frac{2\sigma \cos\theta}{\rho g r}. \tag{1.14}$$

This expression confirms the early observations about the height being inversely proportional to the radius. It also reveals that the height increases monotonically with decreasing contact angle, and it reaches a maximum for $\theta = 0°$.

Note in the above equation (1.14), the weight of the liquid underneath the meniscus was not considered, which is valid for $R \ll a$, since the weight of the liquid underneath the meniscus is very small. But for $R \geq a$, this liquid weight must be accounted. Moreover, the meniscus is no longer spherical due to gravity, which makes the calculation of the liquid weight difficult. Under such circumstances, it has been suggested to compare the mean meniscus position to the theory for the rise between planar surfaces [32].

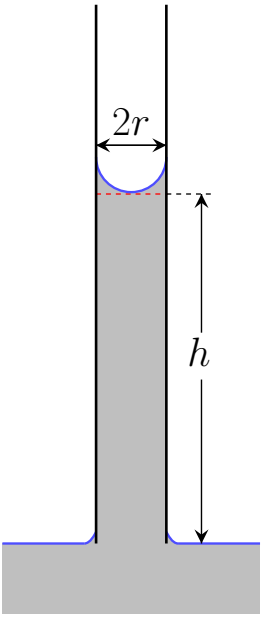

Figure 1.6: Cylindrical capillary.

1.3.2.2 Dynamics

The dynamics of capillary rise can be described by a simple model under the following assumptions.

- The flow is one-dimensional, and it is along the length of the tube.
- The viscous-friction is given by the Hagen-Poiseuille flow.
- The contact angle is constant.
- The liquid-column rising inside the capillary assumes the shape of the capillary i.e, a cylindrical column of cross-section same as the capillary and length h. The shape of the meniscus is ignored.

The capillary force F_σ drives the liquid column, which is opposed by a combination of inertia, added mass F_a, viscous friction F_μ, gravity F_g

and pressure loss F_P. The momentum balance reads,

$$\frac{d}{dt}(mu) = F_\sigma - F_a - F_\mu - F_g - F_P. \tag{1.15}$$

Here, m denotes the mass ($= \rho A_c h$) and u the average speed of the liquid column ($\approx h'$). Physically, the added mass force ($\simeq m_a h''$) is due to the accelerating liquid which drags some amount of the surrounding liquid with it as it moves, when the tube gently touches the liquid pool. Assuming a hemispherical bowl of liquid at the bottom of the tube, equating the work done by pressure difference to the kinetic energy in the system, one obtains $m_a = (7/6)\pi r^3$ [33]. The force F_P denotes the pressure loss due to eddies forming on the sides of the tube entrance as the liquid experiences a abrupt contraction between the reservoir and the capillary. This pressure loss can be written as $0.225\rho u^2$ [34]. Now, substituting the appropriate expressions for the forces and simplifying results in the equation,

$$\left(h + \frac{7}{6}r\right)h'' + 1.225h'^2 + \frac{8\mu}{\rho r^2}hh' + gh = \frac{2\sigma\cos\theta}{\rho r}, \tag{1.16}$$

which describes the evolution of liquid height in the capillary. The force due to added mass and the pressure loss is often neglected in most studies since it is negligible after a few milliseconds [33]. There is no analytical solution for the equation (1.16), hence it must be solved numerically to get the complete picture of the dynamics. Surprisingly, several limiting analytical solutions can be obtained by equating the dominant opposing force(s) with the capillary force in equation (1.16). Table 1.2 lists the some of the limiting solutions along with the assumptions.

Table 1.2: Limiting solutions of equation (1.16)

Assumptions	Governing equation	Solution
Inertial regime[1] [35, 36]		
$h \ll 0$ & $h' \sim 0$	$\frac{7}{6} r h'' = \frac{2\sigma \cos\theta}{\rho r}$	$h = \frac{6}{7} \frac{\sigma \cos\theta}{\rho r^2} t^2$
$h' = constant$	$h'^2 = \frac{2\sigma \cos\theta}{\rho r}$	$h = \sqrt{\frac{2\sigma \cos\theta}{\rho r}} t$
Visco-Inertial regime [37]		
$m_a h'' \sim 0$	$hh'' + h'^2 + \frac{8\mu}{\rho r^2} hh' = \frac{2\sigma \cos\theta}{\rho r}$	$h^2 = \frac{2b_2}{b_1}\left(t - \frac{1}{b_1}(1 - \exp^{-b_1 t})\right)$
		$b_1 = \frac{8\mu}{\rho r^2}$, $b_2 = \frac{2\sigma \cos\theta}{\rho r}$
Visco-gravity regime: Lucas-Washburn equation[2] [38–40]		
inertia is negligible	$\frac{8\mu}{\rho r^2} hh' + hg = \frac{2\sigma \cos\theta}{\rho r}$	$t = -\frac{h}{b_2} \frac{b_1}{b_2^2} \ln\left(1 - \frac{b_2 h}{b_1}\right)$
		$b_1 = \frac{\sigma R \cos\theta}{4\mu}$, $b_2 = \frac{\rho g R^2}{8\mu}$
under zero-gravity	$\frac{8\mu}{\rho r^2} hh' = \frac{2\sigma \cos\theta}{\rho r}$	$h = \sqrt{\frac{\sigma R \cos\theta}{2\mu}} t$

[1] viscous & gravity forces are negligible since $t \ll r^2/\nu$ & $h \ll a$
[2] The ODE has also explicit solutions [41, 42]

These limiting solutions clearly show that the temporal variation of liquid height follows different power-laws during its course of rise. While the liquid eventually reaches equilibrium under gravity, but under zero-gravity (or capillaries oriented horizontally) the liquid continues to rise. In such circumstances, the length of the liquid column at long times varies linearly with the square root of time ($h \sim t^{1/2}$). This solution is often referred as the "Washburn law".

In addition to the above limiting solutions, if the time to reach h_0 is shorter than the diffusion time scale, i.e., $\sigma\mu/\rho^2 g^2 r^3 \ll r^2/\nu$; inertial forces dominate, resulting in oscillations of the liquid column. These inertial oscillations are commonly observed for low-viscosity liquids [35, 36, 43]. The general condition for observing such oscillations is $Oh/Bo \ll 1$ [44].

Limitations of the model The model assumes a constant contact angle, i.e., the meniscus is spherical right from the start of the rise. But in reality the interface is flat at the beginning which progressively develops into a meniscus as it makes contact with the walls of the tube. Several studies [41, 45, 46] report that as a consequence of this constant angle assumption, the model predicts faster rate of rise. But excellent agreement between the model and the experiments is also reported [47, 48]. It could be argued that this discrepancy in the model agreement might be due to the difference in duration for the meniscus development.

1.3.3 Extension to polygonal capillaries and open channels

The forces acting on the rising liquid column remains the same irrespective of the geometry, so the solutions proposed for cylindrical capillaries can be extended to other geometries, with minor modifications related to change in geometry. These modifications include the change in radius of curvature, and viscous friction coefficient k.

1.3.3.1 Radius of curvature

A more general expression for calculating the equilibrium height in any closed geometry is,

$$h_o = \frac{2\sigma}{\rho g R}, \tag{1.17}$$

where R is the radius of curvature of the meniscus. Since the meniscus inside a circular capillary is a part of sphere, the radius of curvature is $R/\cos\theta$. Now assuming the same, one could also approximate the meniscus in polygonal capillaries as a part of sphere, which gives R as $l/\cos\theta$. Here, l refers to the distance between the center of the capillary to the center of one of its sides. By doing so, one ignores the influence of corners in the polygonal capillaries. This naive approximation is only valid for $\theta + \alpha \geq \pi/2$, where α is half of the corner angle.

Mayer-Stowe-Princen Theory (MS-P) This method was independently put forward by Mayer-Stowe [49] and Princen [50–52] for calculating the curvature of the menisci in wedges formed between a pack of cylindrical rods, between a rod and a plate and in polygonal tubes of uniform cross-section. The essence of this method is to equate the curvature of the wedge menisci to that of the bulk meniscus in the form of virtual work. A demonstration of this method for calculating curvature in capillaries of uniform cross-section is given in [53]. Using this method, the equilibrium height was calculated later for square [54], rectangular [34, 55] and triangular [56] capillaries, which showed good agreement with experimental measurements.

The equilibrium height calculated using MS-P theory shows that the presence of rivulets in the corner leads to 6% decrease in the maximum height [50, 54] in a square capillary. Note that this decrease in height is a theoretical estimate calculated using the heights which include and neglect the rivulets i.e, between the naive spherical approximation and the MS-P method.

1.3.3.2 Viscous friction coefficient

The viscous friction coefficient for polygonal capillaries can be obtained from the solutions of the laminar flow in the cross-section of the desired geometry. Analytical solutions in terms of Fourier series exists for standard

cross-sections such as rectangle, triangle and ellipse [57]. Experiments on capillary rise in square and rectangular capillaries [58, 59] show reasonable agreement with the extended model using these expressions.

In case of open channels, the liquid-gas interface interaction also occurs on the open side of the channel, which affects the flow through its impact on the meniscus shape inside the channel. In addition, analytical solutions for open channels does not exist. Several numerical estimates were made by solving the fully developed flow in different geometries such as rectangular [60–62] triangular [63], trapezoidal [64, 65] and sinusoidal grooves [65].

In addition to numerical estimates, the coefficient was also calculated experimentally in different geometries: triangular [66–70], rectangular [71–73] and curved [71]. These studies obtained the coefficient by fitting the temporal variation of the wetting front with the equation of the form $h^2 = ct$. Here, c is called the mobility parameter which includes the coefficient in the form $\sigma lk/\mu$, where σ, l, μ are the surface tension, characteristic length scale and viscosity respectively. These experimentally calculated values, when tested by other researchers, showed contradictory results [71–73], which might be due to the difference in materials used in the fabrication of the channel.

The obtained estimates for the viscous friction coefficient were also tested in spontaneous rise in open channels oriented vertically [59, 74, 75], where the liquid-gas interface is no longer confined to the channels. The results of these studies show that the use of theoretical estimates from the above studies leads to under prediction of the rate of rise.

Instead of using the simple one-dimensional model for describing the rise, one could also theoretically solve the flow in the channel. The first study that focused on this aspect, considered the case of horizontally oriented V-grooves [66]. Assuming a fully developed flow, the mass and momentum equations were reduced to a non-linear diffusion equation, which showed that the final solution had the form $h \sim t^{1/2}$, as predicted by the simple capillary rise model. Even though this solution had the same form ($h \sim t^{1/2}$), it differed from the simple model in the calculation of the capillary force, which included the shape of the interface, and the viscous friction. Later it was shown that the detailed shape of the interface influences the rise rate [67] through the viscous friction coefficient.

1.3.4 Rise near a corner

It is essential to understand the capillary rise near corners since they are abundant in polygonal capillaries, microchannels and open channels, which are being increasingly used in the field of microfluidics.

Consider a wedge formed between two flat plates as shown in the Figure 1.7a, and the angle between them is 2α. At equilibrium, the force balance reads,

$$\nabla \cdot \mathbf{n} = \frac{\rho g}{\sigma} y. \tag{1.18}$$

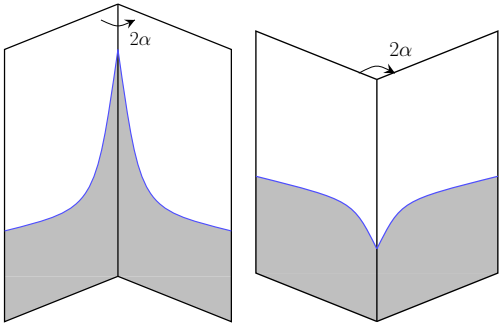

Figure 1.7: Capillary rise in corners: (a) rivulet in inner corner and (b) cusp in outer corner.

Equation (1.18) along with the boundary condition at the wall $\cos\theta = \mathbf{n} \cdot \mathbf{n_w}$, must be solved to obtain the shape of the meniscus in the wedge. Here, $\mathbf{n_w}$ is the unit normal to the wall. Mathematically, the above equation only has a solution when $\theta + \alpha \geq \pi/2$ [76]. In other words, a closed meniscus shape is possible only when $\theta + \alpha \geq \pi/2$. For $\theta + \alpha < \pi/2$, there is no static meniscus shape in the corner. This criteria is now commonly called as the Concus-Finn criteria [76]. Physically, the curving of the meniscus as it nears the wedge results in a negative pressure gradient, which leads to the liquid climbing along the corner resulting in the formation of the rivulets. In the literature, these rivulets are also referred by terms such as wedge or arc meniscii.

While rivulets form in the wedge, one obviously wonders what happens

on the other (opposite) side of the wedge, which is here called as outer corner (see Figure 1.7b). The force balance (1.18) is the same for determining the shape of meniscus. It was shown recently [77] that a smooth meniscus is formed only when $3\pi/2 < \theta + \alpha_e < \pi/2$ and a cusp otherwise. Here, α_e is the half-angle of the outer corner. The positive pressure of the meniscus near the corner squeezes the liquid out resulting in a cusp. Thus one observes two different and completely opposite meniscus behavior on either sides of the corner. The conditions for observing the rivulet or the cusp in corners with different contact angles on its both faces and for different corner angles are discussed in [77, 78]. For a right-angled corner with ($2\alpha = 90°$) found in square or rectangular tubes, the condition for rivulet and cusp formation on the inner and outer corner are the same ($\theta < 45°$).

1.3.4.1 Roundedness of corners

The corners are always rounded in reality, so the rivulets will eventually stop growing when its curvature reaches the curvature of the rounded corner. The length of the rivulet can be calculated as [79],

$$l = \frac{R_o}{Bo}\left(\frac{1}{r^*} - 1\right) \tag{1.19}$$

where R_o is the radius of the bulk meniscus and r^* is the radius of the rounded corner normalised with R_o. Using the roundedness of the corner, the contact angle of the liquid-solid system can also be measured [80].

1.3.4.2 Dynamics of rivulet flows

From the Concus-Finn criteria, it is evident that the rivulets are formed in corners when $\theta + \alpha \geq \pi/2$. So, in polygonal capillaries, open channels, when the Concus-Finn criteria is satisfied, two types of flow are observed: rivulet flow in the corner and the bulk flow.

Several studies on square capillaries [58, 59] and open channels [71–73, 81, 82] discussed above, have reported the presence of rivulets in their corners, which precede the bulk flow. These rivulets rising in the corners can be either detrimental, such as in a microchannel, where it alters the flow by lubricating the channel and also by premature mixing of fluids

[81], or beneficial, such as its use to fabricate microstructures used for force measurements by capillary micromolding [72, 83].

Initial studies [84–89] on the corner flow focused on solving the fully developed laminar flow along the corner/groove in two dimensions, assuming a constant pressure drop and known meniscus shape. The resulting solution for the viscous stresses is presented in integral form, in terms of a dimensionless friction factor, which measures the hydrodynamic resistance to the flow. The influence of the corner geometry (roundedness, corner angle) and the contact angle on the friction factor are discussed. These studies differ primarily in the modelling approaches used for the friction factor, which includes hydraulic diameter approximation [86], full computation of the flow in the given cross-section [84, 85, 87, 88] and the Laplacian scaling approach [89].

Theoretical analysis of the dynamics of rivulet flows in the corner is usually based on the long-wave approximations by assuming a fully developed laminar flow, with negligible inertial effects and also neglecting the deformation of the interface due to viscous stresses and gravity. A similarity solution for the rivulet propagation is obtained in [90], which predicts the evolution of the rivulet height proportional to the square root of time, $h \sim t^{1/2}$, at long times for zero gravity. This square root dependence on time was also observed experimentally [90] in square capillaries placed horizontally, for which the effect of gravity is negligibly small. Further studies [89, 91, 92] on capillary flows in the interior corner of containers has been performed under zero and microgravity conditions in polygonal tubes and containers. Using the lubrication approximation, an asymptotic solution was derived and three regimes were identified: an initial inertial regime ($h \sim t$) followed by a constant flow regime ($h \sim t^{3/5}$) then an overlap regime and finally constant height regime, where the rivulet follows the power-law $h \sim t^{1/2}$.

While the rivulets under zero-gravity follows the power-law $h \sim t^{1/2}$, under gravity, scaling analysis [93] shows that it rises according to the power-law $h \sim t^{1/3}$. This one-third asymptotic growth of rivulets was also observed for the liquid rise in a narrow wedge [94] and in corners formed between different geometries [95].

1.3.5 Numerical studies

Numerical simulations can further enhance our understanding of the flow by resolving them spatially and temporally. Special techniques must be used for the two-phase flow in order to accurately predict the changing topology of the liquid-gas interface. The available techniques can be classified into three broad groups, which are defined below.

- **Surface tracking methods** define a sharp interface using marker particles, which are transported using the calculated velocity field. The exact location of the interface is always known from the location of the markers.
- **Volume tracking methods** define the interface implicitly using an indicator function; hence, the exact location of the interface is not known.
- In **Moving mesh methods**, a dynamic mesh follows the interface and it forms the boundary of the computational domain. The mesh must be adjusted at every time step according to the interface deformations.

While the exact location of the interface is known in both moving mesh and surface tracking methods, it requires either the location of the markers or the mesh to be continuously updated depending upon the interface deformations. This step increases the complexity as well as the computational cost.

The first few numerical studies [96, 97] conducted in capillaries and between parallel plates focused on the steady displacement of the meniscus in a cylindrical capillary, i.e., forced wetting. The main objective of these studies was to investigate the validity of the hydrodynamic theory (HT) by comparing the interface shape. The flow was solved only inside the liquid with boundary conditions applied at the interface. Further, the region close to the wall was completely resolved using a non-uniform mesh: fine near the wall and coarser near the center. Since the interface was completely resolved down to the slip-length, only a microscopic contact angle was used. A few numerical studies focused on demonstrating their solver capabilities in predicting the dynamics of imbibition in cylindrical capillaries [98–100].

Only few studies have focussed on imbibition in corners, where they have discussed the influence of surface roughness (of nanoscopic scale)

on the early stages of rise [101], and identifying the static configurations of meniscus shapes using surface evolver [102, 103], and other numerical techniques mentioned above [104].

1.3.6 Summary

Despite the vast range of the studies on capillary rise in different geometries, there are still some unanswered questions, which are listed below.

- While the capillary flow of the bulk liquid in microchannels has been well documented, the rivulets in the corners have not. Studies so far have confirmed the long-time universal growth of the rivulets, but its dependence on the geometry has not been studied thoroughly. The rate of rise of rivulets is crucial for the design of channels which handle mixing of liquids in minute volumes.
- The studies on capillary rise in open channels have focused mainly on the liquid flow (bulk flow) inside the channel. In an array of connected open channels, the interaction between the neighbouring channels also needs to be explored. These interactions occur at the outer corner between the channel wall and the outer face connecting the channels and also on the outer face which has not been explored yet.
- Forced wetting studies in capillaries conducted so far have focused primarily on validating the contact angle theories. The effect of forced wetting on rivulet dynamics has not yet been investigated.

1.4 Objective and outline of the thesis

The main objective of this thesis is to understand the dynamics of rivulets in corners and their influence on the bulk flow, using a combination of numerical simulations, theoretical analysis and experiments. In this context three cases are considered: (i) Spontaneous rise in square capillaries (ii) Spontaneous rise in open rectangular channels and (iii) Forced wetting in square capillaries. The thesis is structured as follows,

Chapter 2 describes the governing equations and the numerical methodology used in this work. A brief summary of the two-phase flow modelling technique and an overview of the OpenFOAM structure is de-

scribed. Finally, the mesh dependency issues concerning contact line simulations are discussed.

The investigations of spontaneous rise of rivulets in a square capillary is presented in **Chapter 3**. The different stages observed in the rise of rivulets and the influence of various parameters on the rivulet growth rate are described. The flow in the rivulet is described using a long-wave approximation, and finally, a scaling analysis is proposed which predicts rivulet growth rates for the given parameters.

In **Chapter 4**, the spontaneous rise of a liquid in an array of open rectangular channels under the influence of gravity is studied using numerical simulations. The effect of parameters such as channel aspect ratio, outer face width and contact angle on the capillary rise inside the channel and on the outer face are described. The rise is characterized by the meniscus height measured at the channel center, outer face and the interior and exterior corners. The growth rate of rivulets at long times is compared with their equivalent square capillaries.

Following the spontaneous rise studies in square capillaries and open channels, **Chapter 5** investigates the forced wetting in square capillaries, where two forced wetting cases are introduced. In the first case, the capillary is continuously immersed at a constant speed. Here, the focus is on the bulk flow, which is studied using experiments and modelling. The observations from the experiments for different speeds in different capillary sizes are compared with a one-dimensional model. In the second case of forced wetting, liquid is pumped into the capillary at a constant volumetric flow rate. Here, the focus is on the rivulet flow, which is studied using numerical simulations. The effect of forcing on the rivulets under different speeds, capillary sizes and liquids are analysed and finally, the length and thickness of the rivulet are described using lubrication approximation.

Finally in **Chapter 6**, the main findings and conclusions of this thesis are summarized. Some of the outstanding issues and suggestions for future research are described.

2 Numerical methodology

In this chapter, the numerical methodology used in this thesis is described. The governing equations for the two-phase flow, and the underlying interface modelling technique are presented in section 2.1. The contact angle treatment and its associated mesh-dependency problem are reviewed in section 2.2. In section 2.3, the basic framework of OpenFOAM software is provided, and finally in section 2.4 the numerical procedure for the solver is summarized.

2.1 Governing equations

In this study, the two-phase flow is modelled using the Volume-of-Fluid (VOF) method. The basic idea in the VOF method is to treat the two incompressible, immiscible fluids as one mixed fluid which includes both the fluids as well as the interface separating them. This idea is achieved by defining a mixed fluid using an indicator function γ, which represents the volume fraction of the denser fluid in a cell. A cell with $\gamma = 1$ is completely filled with liquid, and $\gamma = 0$ with gas. Any value in-between $(0 < \gamma < 1)$ indicates the presence of the liquid-gas interface in the cell. Thus, this one fluid approach solves only one set of governing equations instead of the two for the two fluids involved. In the VOF method, the interface is modelled implicitly, i.e., while the cells containing the interface can be identified, its exact location in each cell is not known.

The equations governing the flow of this mixed fluid under incompressible, isothermal conditions are,

$$\nabla \cdot \mathbf{U} = 0, \tag{2.1}$$

$$\rho \left(\frac{\partial \mathbf{U}}{\partial t} + \mathbf{U} \cdot \nabla \mathbf{U} \right) = -\nabla P + \nabla \cdot \tau + \rho \mathbf{g} + \mathbf{F}_\sigma. \tag{2.2}$$

Here, $\mathbf{U}$ represents the velocity field, P the pressure field, and $\mathbf{g}$ the

acceleration due to gravity. The viscous stress tensor τ is given by $\mu\left[(\nabla\mathbf{U}) + (\nabla\mathbf{U})^T\right]$, and the term $\mathbf{F}_\sigma$ represents the volumetric form of the capillary force.

The properties (ρ, μ) of this mixed fluid are calculated from the volume weighted averages of the individual phases as given below

$$\phi = \gamma\phi_1 + (1-\gamma)\phi_2. \tag{2.3}$$

Here, $\phi = \rho$ or μ, and the subscripts 1, 2 represent the denser and lighter fluids respectively.

The distribution of the indicator function γ is governed by the advection equation,

$$\frac{\partial\gamma}{\partial t} + \nabla\cdot(\gamma\mathbf{U}) = 0. \tag{2.4}$$

When solving the above equation, sufficient care must be taken to ensure that the interface is sharp, and also γ is both bounded and conserved. Typically, the interface is smeared over few mesh cells due to numerical diffusion. Thus the sharpness of the interface is highly sensitive to the mesh size, which affects the calculation of the curvature. Here, this interface smearing is overcome by using the counter-gradient approach [105]. According to this method, an additional convective term is added to equation (2.4), which artificially compresses the interface thereby maintaining its sharpness. The modified equation is,

$$\frac{\partial\gamma}{\partial t} + \nabla\cdot(\gamma\mathbf{U}) + \nabla\cdot(\gamma(1-\gamma)\mathbf{U}_r) = 0. \tag{2.5}$$

In the above equation, $\mathbf{U}_r$ is the compression velocity, which is actually the relative liquid-gas velocity acting normal to the interface. It is given by $\min\left(C_\gamma|\mathbf{U}|, \max(|\mathbf{U}|)\right)\frac{\nabla\gamma}{|\nabla\gamma|}$, where C_γ is the compression factor, and it is set to one in this work. The term $\gamma(\gamma-1)$ in equation (2.5) ensures that the additional compression from the convective term is active only in the interface region.

2.1.1 Estimation of capillary force

Theoretically, the capillary force resulting from the pressure jump across the curved interface is introduced as a surface stress boundary condition. Since the VOF method models the interface implicitly, this stress boundary condition cannot be implemented directly. A workaround is to treat

this surface force in a volumetric form using the Continuum Surface Force (CSF) approach [106], which is then directly introduced into the equation (2.2) as a source term like gravity. The volumetric form of the capillary force is written as,

$$\mathbf{F}_\sigma = \sigma\kappa\nabla\gamma, \tag{2.6}$$

where κ represents the curvature of the liquid-gas interface. This force is spread over all the cells containing the interface, which eliminates the need for determining the exact location of the interface. The gradient term $\nabla\gamma$ in equation (2.6) ensures that the capillary force acts only in the interface region.

The accuracy of the capillary force calculation depends strongly on the calculation of the curvature which is given by $\nabla \cdot \mathbf{n}$, where $\mathbf{n}$ is the interface normal. Usually (interFoam solver in OpenFOAM) the interface normal $\mathbf{n}$ is calculated from the gradient of the indicator function γ as $\frac{\nabla\gamma}{|\nabla\gamma|}$, but here an iso-contour approach developed in [107, 108] is used. In this approach, the contour $\gamma = 0.5$ is used for calculating the normal. First the cell values of γ are interpolated to its vertices, and then the location where the contour cuts the cell edges are found by the change of sign of the term $(\gamma - 0.5)$. Then the exact position $\mathbf{x}_p$ where the interface cuts the edge is calculated from linear interpolation,

$$\mathbf{x}_p = \mathbf{x}_1 + (\mathbf{x}_2 - \mathbf{x}_1)\frac{0.5 - \gamma_1}{\gamma_2 - \gamma_1}. \tag{2.7}$$

The vectors $\mathbf{x}_1$ and $\mathbf{x}_2$ represent the location of vertices 1 and 2 forming the edge, across which the interface cuts the cell. Applying the above equation to all the cells containing the interface, the position of the contour is determined. Now, using the points $\mathbf{x}_p$, the surface area vector $\mathbf{S}_p$ to the contour in each cell is calculated as shown below,

$$\mathbf{S}_p = \sum_{i=1}^{n} \frac{1}{2}\left(\mathbf{x}_{p,i} \times \mathbf{x}_{p,i+1}\right). \tag{2.8}$$

The points $\mathbf{x}_p$ in the above equation are traversed over in clockwise direction and n is the number of points $\mathbf{x}_p$ in a cell. The interface normal is then calculated from the surface area vector as,

$$\mathbf{n} = \frac{\mathbf{S}_p}{|\mathbf{S}_p|}. \tag{2.9}$$

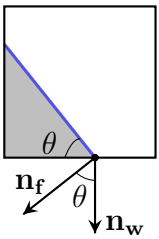

Figure 2.1: Definition of contact angle at the boundary cell.

The curvature is now calculated using this interface normal, and a median filter is applied over this curvature for smoothing. Unlike the classical geometrical reconstruction algorithms like piecewise linear interface calculation (PLIC) [109], this contour based reconstruction approach is not subject to the volume fraction constraint, hence it cannot be used in the flux calculation for the transport of volume fraction.

2.2 Contact angle treatment

Even though the contact angle is a material property of the system, it is introduced as a boundary condition both theoretically and numerically. Numerically, the contact angle [106] is defined as the angle between the interface normal $\mathbf{n}_f$ at the wall and the wall normal $\mathbf{n}_w$ as shown in the Figure 2.1, and given by,

$$\mathbf{n}_f \cdot \mathbf{n}_w = \cos\theta. \tag{2.10}$$

The interface normal interpolated at the wall must be corrected in order to impose the desired contact angle. The corrected interface normal must also lie in the plane spanned by the old interface normal $\mathbf{n}_{f,o}$ and the normal to the wall. So, the corrected interface normal can be written as,

$$\mathbf{n}_f = c_1\mathbf{n}_{f,o} + c_2\mathbf{n}_w. \tag{2.11}$$

The coefficients c_1, c_2 are determined by solving the above equations

(2.10) and (2.11),

$$c_1 = \frac{\cos\theta - \cos\theta_o \cos(\theta_o - \theta)}{1 - \cos^2\theta_o}, \tag{2.12}$$

$$c_2 = \frac{\cos(\theta_o - \theta) - \cos\theta_o \cos\theta}{1 - \cos^2\theta_o}. \tag{2.13}$$

The static microscopic contact angle (θ_A or θ_R) can be used directly as the boundary condition, provided the mesh resolves the intermediate region all the way down to the slip-length, which is usually of the order of nanometers. Kafka and Dussan [110] have shown that for a nanometer slip length, using an interfacial angle at a distance to the contact line ranging from 10 nm to 10 μm leads to almost the same result in the outer region. While this information significantly increases the scale of the region to be resolved, still in most circumstances it is computationally expensive. Under such circumstances, dynamic contact angle models (described in section 1.2.3) should be used.

When using these models, often the cell-face normal velocities at the boundary cell are used as the contact line velocity u_{cl}, which is physically not correct. A better choice for the contact line velocity [111] based on geometrical considerations is ,

$$u_{cl} = \frac{\mathbf{u}_p \cdot \mathbf{n}_f}{\sqrt{1 - \mathbf{n}_w \cdot \mathbf{n}_f}}. \tag{2.14}$$

Here, $\mathbf{u}_p$ is the cell centered velocity of the cell containing the contact line.

2.2.1 Mesh dependency

In the VOF method, the cell face normal velocities are used to advect γ, which provides an implicit slip-length of $\Delta x/2$. Thus, even when a no-slip condition is explicitly enforced at the wall, there is slip. Since this implicit slip-length decreases with the mesh size, it also reduces the contact line speed, which results in mesh dependency [112, 113]. The contact line speed has been observed to vary logarithmically with mesh spacing [114–116]. The mesh dependency in contact line simulations is a fundamental problem independent of the choice of the numerical method.

This mesh dependency can be avoided if the mesh is completely resolved all the way down to the slip-length, and using the Navier-slip at

the boundary [117]. Solving the flow with the mesh resolved down to the slip length is nothing but direct numerical simulation (DNS). As of now, performing DNS even with adaptive mesh refinement (AMR) is limited to only small problems such as axisymmetric drop spreading, plate withdrawal in two dimensions, where the domain size is in the range of millimetres. However in most problems, such as the one discussed in this work, the domain size is large (ranging from centimetres to metres) and in addition, the computations are in three dimensions. Even with AMR, resolving the mesh completely is computationally expensive and time consuming.

Several studies in the literature have proposed solutions for achieving grid independent results. A majority of these proposed solutions are some form of a mesh-dependent contact angle model based on Cox's analysis [12].

The first mesh dependent contact line model [118] was based on Sheng and Zhou's [119] approximation of Cox's theory (see section 1.2.3.1). This model along with Navier-slip was demonstrated using VOF-PLIC method to achieve grid-independent results for two cases: drop spreading and flat plate withdrawal from a large pool. However, the same model was reported [120] to result in mesh-dependent results, which might be due to the difference in interface and curvature modelling techniques between the two. While the former used explicit interface reconstruction technique (VOF-PLIC), the latter used algebraic VOF technique, which is also used in this work.

The second mesh dependent model was developed in the framework of level-set method [117, 121], where it included all the higher order terms considered by Cox (equation 1.6) and also accounts for inertial effects [122]. This model also achieves grid convergence even when the mesh size used was larger than the slip-length, and also matches well with the theory in describing the interface shape. However, the author reports that this model leads to mesh dependent results when $Ca > 0.1$. In addition, some of the parameters used in the model are problem specific, which must be then obtained from the experiments.

The third model [99] also uses Cox's theory, and considers the microscopic contact angle velocity dependent. This model along with the grid based Navier-slip boundary condition, was demonstrated to achieve near convergence, using the front tracking method.

In addition to the above models, in [123] a localized body force at the

contact line along with slip was shown to achieve convergence. However, this body force requires a pre-factor, which must be obtained from fitting the experimental data.

In summary, it can be concluded that the available solutions, i.e., mesh dependent contact angle models, cannot be directly applied in this work, since the underlying techniques used in them are totally different from the algebraic VOF approach used here. Thus, the results presented in this work are mesh dependent. Despite the mesh-dependent results, the physical conclusions reported in this work are independent of the mesh size (see Appendix A). Differences in measured quantities such as the equilibrium height vary by no more than 5% within the mesh refinement.

2.3 Basic structure of OpenFOAM

All the numerical simulations performed in this work were carried out using the open source computational fluid dynamics toolbox, OpenFOAM [124, 125]. In OpenFOAM, the governing equations are discretized using the finite volume method on an unstructured mesh, with co-allocated arrangement, in three-dimensional space. The software is written in the programming language C++ using the object oriented programming approach. It consists of several pre-compiled libraries and solvers intended for different applications.

2.3.1 Finite volume method

The Finite Volume Method (FVM) is commonly used in computational fluid dynamics, due to its conservative nature of the field quantities, which makes it to be easily extended for unstructured meshes. It consists of the following three major steps: domain discretization, equation discretization, and solving the discretized equations.

Domain discretization: The physical geometry is split into a finite number of non-overlapping small volumes, which are often referred to as control volumes or cells. In OpenFOAM this step is accomplished by using either the primitive blockMesh tool for simple geometries or the advanced snappyHexMesh tool for complicated geometries. Each cell consists of a node at its center in which the field quantities are defined and stored.

Each node is surrounded by several faces which forms the boundary of the cell. Each face is shared between two cells unless it is located at the boundary of the domain.

Equation discretization: In the second step, the governing partial differential equations (PDE) are transformed into a set of algebraic equations. This step involves first integrating the PDE over each control volume to obtain a semi-discretized form of the equation. The general form of the conservation equation for any arbitrary variable Φ is,

$$\frac{\partial(\rho\Phi)}{\partial t} + \nabla \cdot (\rho \mathbf{U}\Phi) = \nabla \cdot (\Gamma \nabla \Phi) + S_\Phi \tag{2.15}$$

where t is the time, Γ is the diffusivity of Φ and S_Φ is the source term. Note that the conservative form of the equation described above includes all modes of transport: convection, diffusion and source/sink. Assuming constant material properties (ρ, Γ), the above equation can be integrated over a control volume which reads,

$$\rho \left[\frac{\partial}{\partial t} \int_V \Phi dV + \int_s \Phi \mathbf{U} \cdot d\mathbf{S} \right] = \rho\Gamma \int_S \nabla\Phi \cdot d\mathbf{S} + \int_V S_\Phi dV. \tag{2.16}$$

Replacing the surface integrals by a summation over the control volume faces, and the volume integral by the volume V_P of the cell, equation (2.16) becomes,

$$\rho \left[V_c \left(\frac{\partial(\rho\Phi)}{\partial t} \right)_c + \sum_f \Phi_f \mathbf{U}_f \mathbf{S}_f \right] = \sum_f (\nabla\Phi)_f \mathbf{S}_f + S_{\Phi,c} V_c. \tag{2.17}$$

The variables, V_c, $\mathbf{S}_f$ represent the volume of the cell and the surface area vector of faces of the cell respectively. In order to calculate the gradient $(\nabla\Phi)_f$ at the face, the variation of Φ between the cells is required, which is usually assumed to be linear. Similar to the discretization of the spatial domain, the time domain is also subdivided into a finite number of intervals called time steps (Δt). Equation (2.17) is solved only at these discrete time steps. Since the governing PDE (2.15) is a parabolic equation, it is only influenced by the events happening before the current time step, hence the transient term in equation (2.17) can be expressed

as a function of,

$$\left(\frac{\partial(\rho\Phi)}{\partial t}\right)_c \approx f(\Delta t, \Phi^n, \Phi^{n-1}, ...), \tag{2.18}$$

where the superscript $n, n-1, ..$ refers to Φ at present and previous time steps. A wide range of temporal and spatial discretization schemes are available in OpenFOAM. A detailed discussion of those numerical schemes are discussed in [126–128].

Solution of the discretized equations Finally, assembling all the discretized equations yields a system of linear algebraic equations of the form:

$$\mathbf{A} \cdot \Phi = \mathbf{b}, \tag{2.19}$$

where $\mathbf{A}$ is the coefficient matrix and $\mathbf{b}$ is the source matrix. The above equation can be easily solved using the direct method, which usually involves inverting $\mathbf{A}$ and multiplying it with $\mathbf{b}$. However, when the number of cells in the domain increases, this inversion task becomes computationally expensive. Hence, iterative methods are usually preferred, where an initial guess for the solution is made, which is improved iteratively by solving the discrete system of equations until it reaches a desired tolerance defined by the user.

2.3.2 Adaptive mesh refinement

In order to capture the contact line physics near the wall and model the capillary force accurately, the liquid-gas interface must be resolved sufficiently. However, refining the complete domain to the smallest mesh size for accuracy, is computationally expensive and unnecessary. This problem is overcome by using adaptive mesh refinement (AMR), which selectively resolves the region where it is required, while keeping other cells at a coarser mesh. Selecting the region for refinement is made by monitoring one of the field variables or its gradient, as defined by the user. In this work, the liquid-gas interface is chosen for refinement, which is done by refining the cells where the gradient of the indicator function is non-zero.

At each time step, the cells are identified and marked for refinement, based on the user-defined criteria. Each marked cell is split into eight new cells and the splitting can be consecutively applied, i.e., the newly created cells can be further split. The coarsest cell is called the parent cell and the newly created cells from splitting are called daughter cells. This splitting process is indicated by the level of refinement, with the level starting from zero in the base mesh. The refined cells can be recombined into the original parent cell if they are marked for un-refinement (coarsening). After refinement, the field values in the parent cells must be mapped into the daughter cells, which is done by interpolation. Similarly, after coarsening, the value for the coarsened cell is obtained by averaging.

During refinement operations, there are circumstances where some of the daughter cells might share one of their faces with a coarse cell. This situation results in hanging nodes, which, if present at the interface, will result in poor accuracy due to interpolation errors. These errors are avoided by providing several layers of cells in each refinement, such that the hanging nodes are not found near the interface.

2.3.3 Parallelization and load balancing

Large scale computations are often run in parallel, since the number of linear algebraic equations to be solved are high. Parallelization splits the computational domain into smaller sub-domains, where the equations are solved for those sub-domains simultaneously on different processors. The resulting solution from each sub-domain must be coupled together at each time step, which necessitates communication between the processors. In OpenFOAM, this communication is achieved using Message Passing Interface (MPI). The speed-up achieved by parallelization is limited by the speed of the slowest processor. In addition, the computational cost involved in the floating point operations must be higher than the cost for communication between the processors, for the parallelization to be effective.

When using AMR, depending upon the refinement criteria, the cells are frequently refined and coarsened in each sub-domain at every time step, which makes the relative load of the processors worse, thus affecting the speed-up of the operations as well as the accuracy. This imbalance between the processors is avoided by using a load balancing algorithm, which pauses the simulation every time an imbalance is detected, redis-

tributes the cells among the processors. The imbalance is determined by calculating the relative change between the number of cells per processor to the average number defined and taking the maximum relative change as the imbalance. In this work, the imbalance is detected whenever the maximum relative change is above 0.25. During redistribution, sufficient care must be taken to ensure that the daughter cells from the same parent are redistributed on the same sub-domain.

2.4 Solution procedure

2.4.1 PISO

The main requirement of any algorithm used for numerically solving the fluid flows, is its ability to deal with the pressure velocity coupling. Since the two-phase flow being solved is considered as incompressible, there is no explicit equation for computing the pressure field. Typically, the pressure equation is obtained by combining the semi-discretized momentum and continuity equation. In this work, this pressure velocity coupling is dealt with the Pressure-Implicit Split Operator algorithm (PISO) developed by Issa [129]. It consists of three main steps:

- **Predictor step** The momentum equation is solved using the available pressure field from the previous time-step. Note this approximate velocity field is not divergence free.
- **Pressure solution** Using this approximate velocity field, the pressure equation is solved.
- **Explicit velocity correction** The fluxes are updated and the velocity field is corrected using the new pressure field

The last two steps are repeated till the updated velocity is divergence free, i.e., until it reaches the desired tolerance.

2.4.2 MULES

The transport equation (2.5) for γ is non-linear and hyperbolic. The numerical method used for solving this equation must preserve the boundedness of γ as well as retain the sharp interface. In OpenFOAM, it is achieved using Multi-dimensional Universal Limiter of Explicit Solution

(MULES) algorithm [105]. The semi-discretized version of (2.5) contains fluxes from the linear term and also from the compression term, which is non-linear. While the linear flux is calculated explicitly, the non-linear flux is calculated using a blend of higher-order, limited and first order upwind schemes. In addition, this anti-diffusive flux is then limited by the extrema determined using the neighboring cells.

Temporal sub-cycling In order to achieve stability, the transport equation (2.5) is solved in several sub-cycles within a single time step. The time step used during this sub-cycling is obtained from the dividing the global time-step with the number of sub-cycles, which is defined by the user. The mass fluxes calculated in each sub-cycle are summed up at the end of the cycle to be used in the momentum equations.

2.4.3 Adaptive time stepping

Despite the use of Euler implicit scheme for discretizing the transient term in the momentum equation (2.2), the Courant number Co must be kept always less than 1. Also maintaining $Co < 1$ ensures that the volume fraction is not transported more than one mesh cell per time step, which is important for stability of the solution. There are two available options in OpenFOAM : fixed time step or fixed Co. Among the two, the latter is always preferred and it is achieved by using adaptive time step control,

$$\Delta t = min\left\{\frac{Co_{max}}{Co}\Delta t^o, \left(1+\lambda_1\frac{Co_{max}}{Co}\right)\Delta t^o, \lambda_2\Delta t^o\Delta t_{max}\right\}, \quad (2.20)$$

where local Courant number is defined as

$$Co = \frac{\mathbf{U}_f \cdot \mathbf{S}}{\mathbf{d}\cdot\mathbf{S}}. \quad (2.21)$$

The superscript o refers to the old value and the vector $\mathbf{d}$ refers the to the distance between cell centres. The constants λ_1 and λ_2 have values 0.1 and 1.2 respectively. This adaptive time stepping provides a smooth variation of time step, which helps to keep the Co calculated at every time step closer to the user defined value Co_{max}. In this work Co_{max} is set to 0.2, which gives time steps lower than the time step restriction required for capturing the capillary waves [106].

At every time step, first the transport equation (2.5) is solved using MULES with the velocity field from the last time step. Then the curvature

of the interface is calculated, which is then used to calculate the volumetric capillary force. Finally, assembling all the external forces, the momentum equation is solved using PISO algorithm.

3 Spontaneous rise of rivulets in a square capillary

This chapter presents the investigation of the spontaneous rise of rivulets in a square capillary under the influence of gravity. The effect of various parameters such as capillary size, contact angle and liquid viscosity on the long-time behaviour of the rivulet growth is the main objective.

The computational setup used for the simulations is presented in section 3.1, and in section 3.2 the general flow features of the spontaneous rise in the square capillary is described. Section 3.3 presents theoretical analysis of the flow inside the rivulet and its shape using lubrication approximation. Finally, in section 3.4 the results are summarized.

This chapter is based on the article *Computations of spontaneous rise of a rivulet in a corner of a vertical square capillary* by V. Thammanna Gurumurthy et al. (2018), published in Colloids and Surfaces A: Physicochemical and Engineering Aspects.

3.1 Computational setup

The parameters chosen for the study are the capillary size w, contact angle θ and the liquid viscosity μ. The size of the capillaries used are 0.6, 1 ,3 and 4.5 mm. Since the study is primarily on the capillary rise of rivulets the contact angles chosen are $0°$, $15°$, $30°$. The commonly used liquid polydimethyl siloxane (PDMS) in wetting experiments is used here with two different viscosities. The physical properties of the liquids used are given in the Table 3.1. The Bond number Bo based on the capillary sizes 0.6, 1 ,3 and 4.5 mm are 0.17, 0.46, 4.15 and 9.33 respectively.

Since the square capillary is symmetric along its cross-section, only one quarter of its cross section is simulated. The computational domain consists of a square column, as shown in the Figure 3.1, of size $w/2 \times w/2 \times L$. The length of the computational domain L is set to 30 mm for

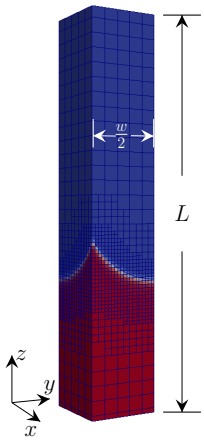

Figure 3.1: Computational domain.

Table 3.1: Material properties of the liquids used in the simulations.

Properties	PDMS-20cSt	PDMS-100cSt
Density(kg/m^3)	930	970
Viscosity (mPa s)	19.2	97
Surface tension (mN/m)	19.8	20.1
Capillary length (mm)	1.47	1.45

all the capillary sizes to ensure that both the rising bulk meniscus and the rivulets are located in the computational domain. The base mesh size for each capillary is $w/10$ and an adaptive mesh refinement is used with load balancing along the liquid-gas interface for higher accuracy. Based on the grid convergence tests (see Appendix A), the refinement levels are kept at 2, 3, 4 and 4 for capillary sizes 0.6, 1, 3, and 4.5 mm respectively. Figure 3.1 shows also the typical mesh employed in the simulations. The boundary conditions are symmetry at the back and right faces of the column, inlet at the bottom for the liquid flow and the top face is open to the atmosphere. The front and left faces of the column have constant contact angle and no-slip boundary condition. As described in the previous chapter, the VOF method uses an implicit slip length [118] of $\Delta x/2$, which alleviates the stress singularity at the contact line.

Previous studies about rivulet flow in other geometries [94, 95] show that the capillary number based on the speed of rivulets is very small. Under such conditions, the effect of the dynamic contact angle is minor and therefore a static contact angle at the boundaries can be assumed. Such an assumption is the same as in [89].

Here, the capillary rise is characterized by measuring the height of the meniscus in the center and in the corner of the capillary, which represent the bulk flow and rivulet flow respectively. Both heights are measured with respect to the origin ($z = 0$) (see Figure 3.1). When describing the corner flow in detail, the height of the rivulet tip is measured relative to the center of the bulk meniscus as described in [130].

3.2 General features of the flow

Figure 3.2 shows the computed meniscus shapes in a square capillary of size $w = 3$ mm for various contact angles ($0°$, $15°$, $45°$, $60°$) at $t = 5$ s, For $\theta \geq 45°$ the liquid in the corner reaches equilibrium, thus approaching a long-time stationary situation, but for $\theta < 45°$, the computations show an emergence of continuous rivulet flow in the corners as predicted by the theory [76].

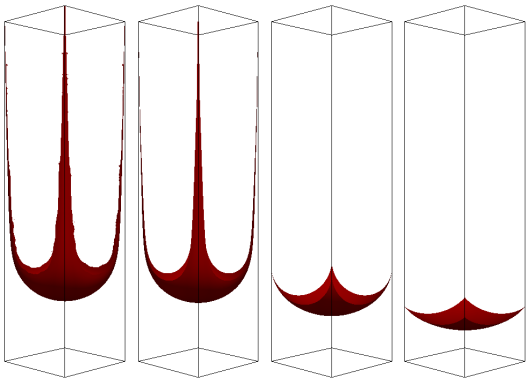

Figure 3.2: Meniscus shapes in 3 mm capillary at different contact angles. Images from left to right are at $\theta = 0°$, $15°$, $45°$ and $60°$ at $t = 5$ s.

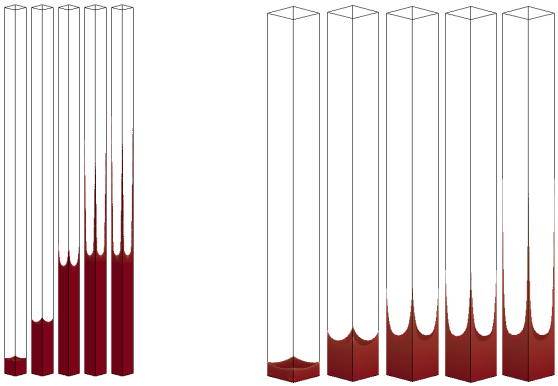

(a) $w = 1$ mm (b) $w = 3$ mm

Figure 3.3: Instantaneous snapshots of capillary rise in square capillaries. The snapshots are taken at $t = 0.01,\ 0.1,\ 1,\ 10$ and 15 s for $\theta = 30°$.

Figures 3.3a and 3.3b show the instantaneous snapshots of capillary rise observed in $w = 1$ mm and $w = 3$ mm capillary at $\theta = 30°$. As the contact angle satisfies both the general condition for the capillary rise in the bulk ($\theta < 90°$) and the rivulet formation in the corner ($\theta < 45°$), bulk and corner flows are seen. Such a situation is referred as *compound capillary flow* [130]. Eventually the bulk rise reaches equilibrium, where it attains a constant height and thereafter there is only rivulet rise in the corners.

Figures 3.4a and 3.4b show the progression of meniscus height measured in the center and in the corner of the capillary over time for $w = 1$ mm and $w = 3$ mm respectively. The corner rise always precedes the bulk, unlike the capillary rise observed in wedges where the maximum height slowly approaches the corner from the bulk [94, 95]. Thus the capillary rise in a square capillary has two different regimes: *compound capillary flow* at the early stages and *corner flow* at the later stages, when the bulk rise has reached equilibrium.

In the early stages of the capillary rise, bulk flow and corner flow are coupled, as the capillary pressure driving the liquid is shared between them at the bulk meniscus. This coupling is reflected in the rise, where

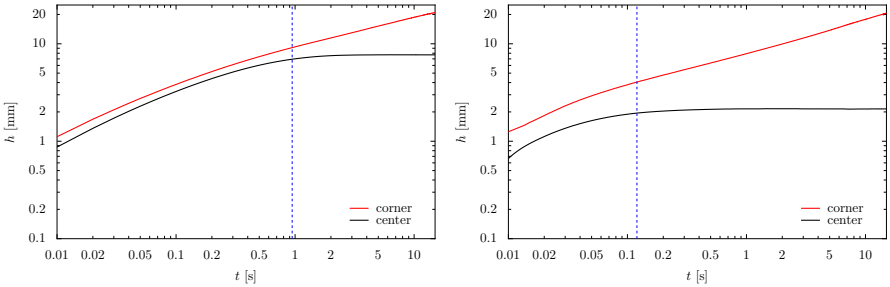

(a) $w = 1$ mm (b) $w = 3$ mm

Figure 3.4: Temporal variation of rise height in the center and in the corner for $\theta = 0°$. The dashed vertical line indicates the $t_{90\%}$.

we observe the corner rise following the same trend as the bulk rise (see Figures 3.4a and 3.4b). During its rising stage, the bulk flow undergoes several regimes [131] in which its speed continuously decreases due to the increasing friction and gravitational pull, eventually reaching equilibrium. The bulk rise at some point of time ($t = t_s$) enters the visco-gravitational regime, during which it exponentially relaxes [42] towards equilibrium. This early stage ends when the bulk rise enters the visco-gravitational regime, and here its duration is taken as the time to reach 90% of its equilibrium height ($t_s = t_{90\%}$).

3.2.1 Dynamics of rivulet flow at long times

At times larger than t_s, the height of the bulk meniscus quickly approaches a plateau, thus reaching equilibrium while the rivulet in the corner continues to rise (see Figure 3.4). This stationary bulk meniscus situation is described by the solution in the corner flow limit under zero gravity [130].

The height of the rivulet tip H is measured from the central, lowest point of the main bulk meniscus and the time T is measured from the instant when the meniscus height reaches 90% of its maximum height, $T = t - t_{90\%}$. Figure 3.3 shows the temporal evolution of rivulet tip height in the corner at $\theta = 15°$ for all capillary sizes. A few seconds after the bulk rise reaches equilibrium, the rivulet rises according to the one-third asymptotic $H \sim T^{1/3}$. This result is in the agreement with the

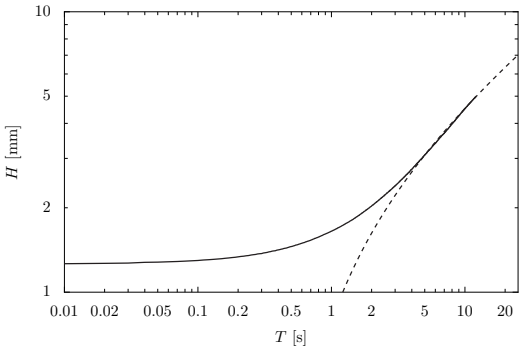

(a) $w = 0.6$ mm

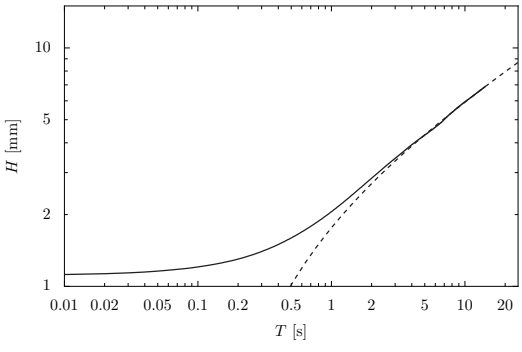

(b) $w = 1$ mm

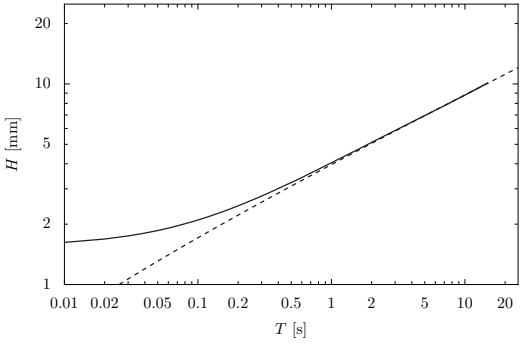

(c) $w = 3$ mm

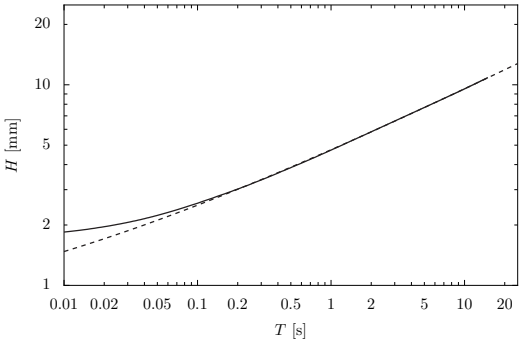

(d) $w = 4.5$ mm

Figure 3.3: Temporal variation of the rivulet tip height in the corner for $\theta = 30°$. The dashed line is the one-third asymptotic least squares fit $H = c_1 T^{1/3} + c_2$, where c_1 and c_2 are fitting constants.

existing theoretical predictions and experimental observations for an open corner [93–95].

3.2.2 Parameter study

Figure 3.4 shows the effect of parameters such as the capillary size, contact angle and the viscosity on the rivulet rise at long times. The effect of these parameters is characterized qualitatively by observing the slope of the one-third fits made to each curve. The slope of the curves in the Figure 3.4a varies only slightly with the capillary size, implying a weak dependence. Figure 3.4b shows the effect of contact angle for $w = 1$ mm, where the rate of rise decreases with increasing contact angle as the capillary force decreases. In addition to the decreasing capillary force, the contact area of the liquid with the wall also increases with contact angle, which increases the viscous dissipation. Similar to the contact angle, increasing the viscosity reduces the rate of rise due to the increased viscous dissipation as shown in the Figure 3.4c.

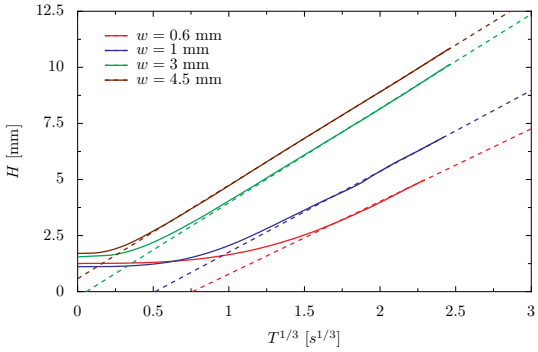

(a) Effect of capillary size at $\theta = 30°$.

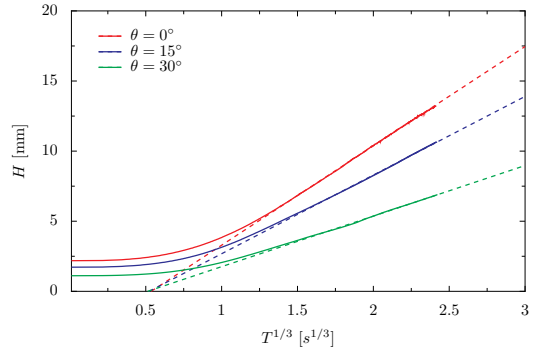

(b) Effect of contact angle at $w = 1$ mm.

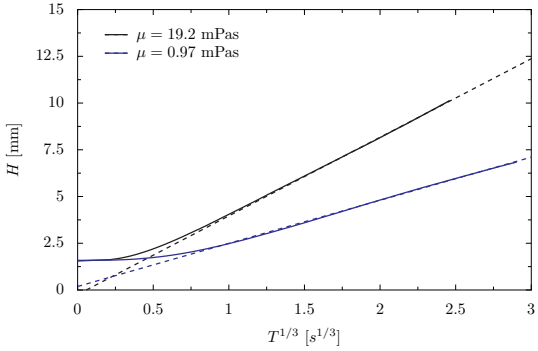

(c) Effect of viscosity at $w = 3$ mm, $\theta = 30°$.

Figure 3.4: Effect of the capillary size, contact angle and viscosity on the rivulet rise in the corner. The dashed lines to each curve is the one-third asymptotic least squares fit to each curve.

3.3 Scaling of the flow in the rising rivulet

Similar to bulk flow, the flow in the corner is also governed by surface tension, gravity and viscous stresses. The speed of rivulet rise at long times is very small ($\approx$ 1-5 mm/s), while the rivulet thickness is 0.1 - 0.5 mm. Thus the Reynolds number associated with this flow is very small ($\approx 0.01 - 0.1$); hence, the inertial effects can be safely neglected.

The complete shape of the rivulet in the corner is three dimensional, thus an exact analysis of such flow is rather complicated. However, far from the bulk meniscus the rivulet is thin. In this region a theoretical description of the rivulet flow using the long-wave, lubrication approximation is straightforward [89, 90, 92, 94, 130, 132]. Below, the conventional derivations for the rivulet flow in the framework of the long-wave approximation are presented and examined.

Consider a coordinate system with the z-coordinate along the corner with the origin at the central, lowest point of the bulk meniscus. The thickness of the rivulet at a given height z is denoted by $\delta(z,T)$ (See the definition of δ in Figure 3.5a). In the long-wave approximation, $\partial\delta/\partial z \ll 1$, the curvature of the rivulet can be roughly estimated as

$$\kappa = \frac{1-\sqrt{2}\cos\theta}{\delta(z,t)} - \frac{\partial^2\delta}{\partial z^2}, \tag{3.1}$$

where the first term in the right-hand side of the equation is the curvature of the meniscus in transverse direction obtained from pure geometrical considerations, and the second term is associated with the curvature in the longitudinal direction (along z). Close to the bulk meniscus it is equal to the local meniscus radius R_o.

Far away from the bulk meniscus, the thickness of the rivulet is much smaller than the meniscus radius $\delta \ll R_o$, so the curvature in longitudinal direction can be neglected. The expression for the curvature κ in this region, where $\delta \ll R_o$, now simplifies to

$$\kappa \approx \frac{1-\sqrt{2}\cos\theta}{\delta(z,t)}. \tag{3.2}$$

Next, since the velocity component in the direction normal to the solid wall of the capillary is very small, the pressure is uniform in the cross-section normal to the z-axis, and can be estimated using the Young-Laplace equation,

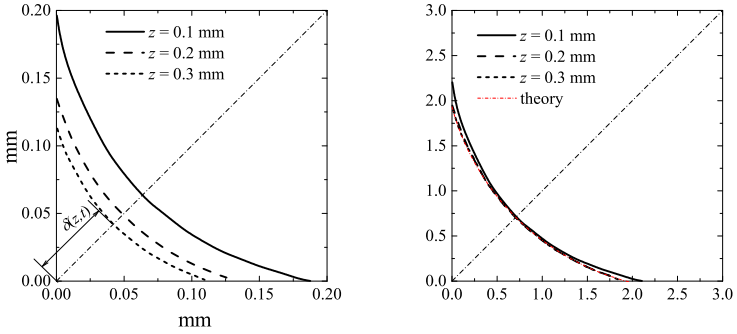

(a) (b)

Figure 3.5: (a) Shape of the rivulet in transverse direction at various heights from the bulk meniscus for $w = 0.6$ mm, $\theta = 15°$. (b) The shapes are scaled by the corresponding value of δ and compared with the theoretically predicted circular interface of constant curvature, determined in equation (3.2).

$$p = \sigma\kappa(z). \tag{3.3}$$

Figures 3.5 and 3.6 show the shape of the rivulet in transverse direction at at various heights z from the bulk meniscus for $w = 0.6$ and $w = 4.5$ mm, respectively. For both cases the interface shapes are scaled by the corresponding values of δ (shown in Figures 3.5b and 3.6b). For smaller capillary width ($w < a$), the shapes quickly approach the circular shape of the curvature predicted by the approximate expression (3.2). For the larger capillary ($w > a$), the shapes are also nearly circular (see Figure 3.6), but the deviation from the predicted curvature (3.2) can be noted. This deviation is due to the width of the capillary being comparable with the capillary length, so the forces associated with gravity lead to the interface deformation, especially in the regions near the bulk meniscus where the gradient $\partial\delta/\partial z$ cannot be neglected.

Remote stationary shape of the rivulet At long times a portion of the rivulet shape near the bulk meniscus approaches a static shape. This

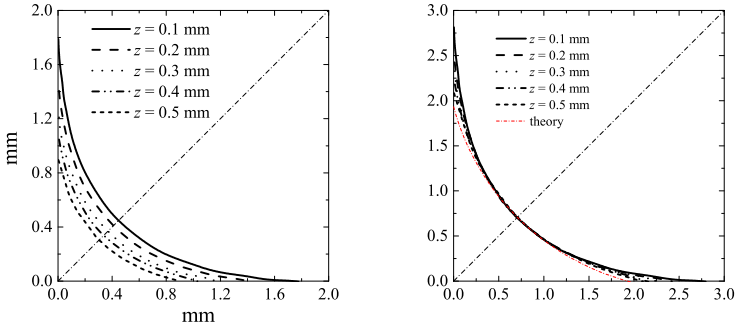

(a) (b)

Figure 3.6: (a) Shape of the rivulet in transverse direction at various heights from the bulk meniscus for $w = 4.5$ mm, $\theta = 15°$. (b) The shapes are scaled by the corresponding value of δ and compared with the theoretically predicted circular interface of constant curvature, determined in equation (3.2).

shape can be estimated by equating the expression for pressure given by the equation (3.3) with the hydrostatic pressure, leading to the equation for the rivulet thickness in the form

$$\sigma \frac{1 - \sqrt{2}\cos\theta}{\delta_{\text{stat}}(z)} + p_0 + \rho g z = 0, \tag{3.4}$$

where $-p_0 = 2\sigma/R_o$ is the Laplace pressure at the bulk meniscus, R_o is its radius at $z = 0$. Solving the above equation results in an approximate solution for the rivulet thickness of the static meniscus given by

$$\delta_{\text{stat}} = \frac{A\sigma}{\rho g(h_0 + z)}, \tag{3.5}$$

$$A = \sqrt{2}\cos\theta - 1, \quad h_0 = \frac{2\sigma}{\rho g R_o}, \tag{3.6}$$

where h_0 is the height of the bulk meniscus. Note that the solution for δ_{stat} is positive only if $\theta < \pi/4$, which is in the agreement with the existing threshold for the rise of rivulets [76]. The only unknown in the above equation is the radius of bulk meniscus R_o, which can be calculated from

the equilibrium height for the bulk meniscus h_0. The equilibrium height in a capillary is typically calculated by balancing the capillary force with the weight of the liquid. Here, in a square capillary, when calculating the weight of the liquid, the mass of the rivulets should also be considered.

The total mass of the rivulet for long times is calculated by,

$$M_r \equiv \rho \int_0^\infty S_r \mathrm{d}z \tag{3.7}$$

where S_r refers to the cross-sectional area of the rivulet. It can be estimated from geometrical considerations,

$$S_r = \frac{\delta^2}{4A^2} \left[4\theta - \pi + 4\cos\theta(\cos\theta - \sin\theta)\right]. \tag{3.8}$$

Using the above equation, the total mass of the rivulet can be roughly estimated as,

$$M_r = \frac{\sigma^2}{4g^2\rho z_0}(2 - \pi + 4\theta + 2\cos\theta - 2\sin 2\theta). \tag{3.9}$$

Balancing the weight of the liquid in the capillary with the capillary force results in the following equation,

$$4M_r g + w^2 \rho g z_0 = 4w\sigma\cos\theta. \tag{3.10}$$

The prefactor 4 in the first term in the above equation is introduced to account for the rise of rivulets in the four corners of the capillary. The equilibrium height (h_0) of the bulk meniscus for the contact angles $\theta < \pi/4$ is the root of equation (3.10) obtained in [54] with the help of (3.9)

$$h_0 = \frac{\sigma}{\rho g w}\left(2\cos\theta + \sqrt{\pi - 4\theta + 2\sin 2\theta}\right). \tag{3.11}$$

The average radius R_o of the meniscus is therefore,

$$R_o = \frac{2\sigma}{\rho g z_0} = \frac{2w}{2\cos\theta + \sqrt{\pi - 4\theta + 2\sin 2\theta}}. \tag{3.12}$$

The value of R_0 is uniform at the meniscus surface only in the limit $w \ll a$. When the size of the capillary is comparable or larger than the capillary length a the curvature of the meniscus is not uniform and depends on the local position at the interface.

Dynamics of the flow in the rivulet Consider now the flow in the thin rivulet far away from the bulk meniscus. Neglecting the inertial effects, the momentum balance for the flow in the rivulet can be written as

$$-\frac{\partial p}{\partial z}-\rho g+\mu\left(\frac{\partial^2 u}{\partial x^2}+\frac{\partial^2 u}{\partial y^2}\right)=0, \tag{3.13}$$

where u is the stream-wise velocity component along z. Here only the major viscous terms are taken into account, as in the lubrication approximation, valid for a long rivulet. Equation (3.13) can be simplified assuming the similarity of the flow in a rivulet cross-section. In this case the momentum equation is reduced to

$$-\frac{\partial p}{\partial z}-\rho g-B\mu\frac{U(z,T)}{\delta(z,T)^2}=0, \tag{3.14}$$

where B is a dimensionless coefficient of order unity, which depends only on the contact angle θ. The value of B is associated with the friction factor [130], which is often introduced to account for the shape of the cross-section of the rivulet. $U(z,T)$ is the characteristic longitudinal velocity of the liquid in a rivulet cross-section. This velocity can now be estimated from (3.14) with the help of (3.2) and (3.3)

$$U=-\frac{g\rho h^2}{B\mu}-\frac{\sigma A\delta_z}{B\mu} \tag{3.15}$$

The mass balance equation for the rivulet flow is,

$$\frac{\partial S_r}{\partial T}+\frac{\partial Q}{\partial z}=0, \tag{3.16}$$

where Q ($\equiv US_r$) is the volumetric flow rate of the rivulets. Simplifying the above equation using (3.8) yields,

$$\frac{\partial \delta^2}{\partial T}+\frac{\partial \delta^2 U}{\partial z}=0. \tag{3.17}$$

The equation for the evolution of the rivulet thickness is obtained by substitution of (3.15) in (3.17)

$$4g\rho\delta_z\delta^2-2B\mu\delta_T+A\sigma\left(\delta_{zz}\delta+2\delta_z^2\right)=0 \tag{3.18}$$

The suffixes z ,T in the above equation indicate the differentiation with respect to the axial co-ordinate z and the time T. This equation has a similarity solution far from the bulk meniscus of the capillary:

$$\delta(z,T) = LF\left[W - G(z+h_0)T^{-1/3}\right]T^{-1/3}. \tag{3.19}$$

$$L = \frac{(AB\mu\sigma)^{1/3}}{2\times 3^{1/3}(g\rho)^{2/3}}, \tag{3.20}$$

$$G = \frac{(2Bg\mu\rho)^{1/3}}{3^{1/3}(A\sigma)^{2/3}}, \tag{3.21}$$

where W is an unknown constant and $F(\xi)$ is a dimensionless function of a similarity variable ξ,

$$\xi = W - G(z+z_0)T^{-1/3}. \tag{3.22}$$

Substituting the expression for δ given by (3.19) results in the ordinary differential equation

$$-F_\xi F^2 + F_{\xi\xi}F + F + 2F_\xi^2 - WF_\xi + \xi F_\xi = 0. \tag{3.23}$$

Function $F(\xi)$ can be obtained by the integration of the above ordinary differential equation subject to the boundary conditions

$$F(0) = 0, \quad F(\xi \to W) = \frac{4}{W-\xi}, \tag{3.24}$$

Here, $\xi = 0$ corresponds to the rivulet tip and the region $\xi \to W$ corresponds to the static solution (3.5).

The similarity solution (3.19) described above for the rivulet flow cannot be matched directly with the bulk meniscus but only with the intermediate region, where the shape of the rivulet at large times approaches the static solution given by the equation (3.5). Thus the solution for the rise of rivulets in the corner is subdivided into three main regions: (i) the similar flow (3.19) near the rivulet tip, (ii) the intermediate region which at large times approaches the static solution and (iii) the complex three-dimensional shape of the rivulet near the bulk meniscus. The regions (i) and (ii) are matched by the second condition in (3.24). Note that the flow in the region close to the bulk meniscus cannot be explained using the long-wave approximation; hence, the exact values for W cannot be obtained from this analysis. Thus, full three-dimensional computations are necessary for a reliable solution of this problem.

3.3.1 Rivulet profile $\delta(z)$

The dimensionless rivulet profile along the corner, $F(\xi)$, is estimated from (3.19) using the values for $\delta(T)$ from the numerical simulations. The unknown dimensionless parameter $B(\theta)$ obtained by fitting $F(\xi)$ using the condition that $F(\xi)$ does not depend on θ. Figure 3.7b shows the variation of dimensionless parameter with contact angle. The results of computations of $F(\xi)$ are shown in Figure 3.7a for the capillary size $w = 3$ mm and $\mu = 19.2$ mPa s at $t = 15$ s. The predicted shapes $F(\xi)$ for different contact angles coincide on the segment $\xi < 1$, indicating the self-similarity of the rivulet rise. At larger values of ξ the different profiles diverge as the similarity solution breaks down near the bulk meniscus.

The dimensionless rivulet shape for various liquid viscosities and capillary sizes are shown in Figure 3.8 for $t = 13,\ 14,\ 15$ s. In all the cases, the similarity solution is valid near the rivulet tip (for small values of ξ) and breaks down near the static bulk meniscus. The effect of the bulk meniscus is especially clear in the case of different capillary sizes which leads to the dependence of the rivulet growth on the capillary size w.

3.3.2 Rivulet growth rate

The long-time asymptotics for the position of the rivulet tip at $\xi = 0$ can now be determined from (3.19) as

$$H = K\frac{(A\sigma)^{2/3}}{(Bg\rho\mu)^{1/3}}T^{1/3}, \tag{3.25}$$

where K is a dimensionless rate of the rivulet growth. This relation is similar to the corresponding expression obtained in [130], where the rivulet tip under zero gravity is shown to follow the power-law: $H \sim T^{1/2}$.

Equation (3.25) can be rewritten in the form $H/a \sim (\sigma T/\mu a)^{1/3}$. This relation describes well the evolution of the rivulet tip in the corner formed between different geometries [94, 95]. Figure 3.9 presents the temporal variation of the dimensionless rivulet height in the corner of 3 mm capillary at two values of the contact angle: $\theta = 15^\circ$ and 30°. The curves for the same contact angle collapse into one curve for both viscosities when scaled using the form described above. However, the same scaling, when used to scale rivulet heights obtained from different capillary sizes, does not collapse into one curve due to the weak geometrical dependence.

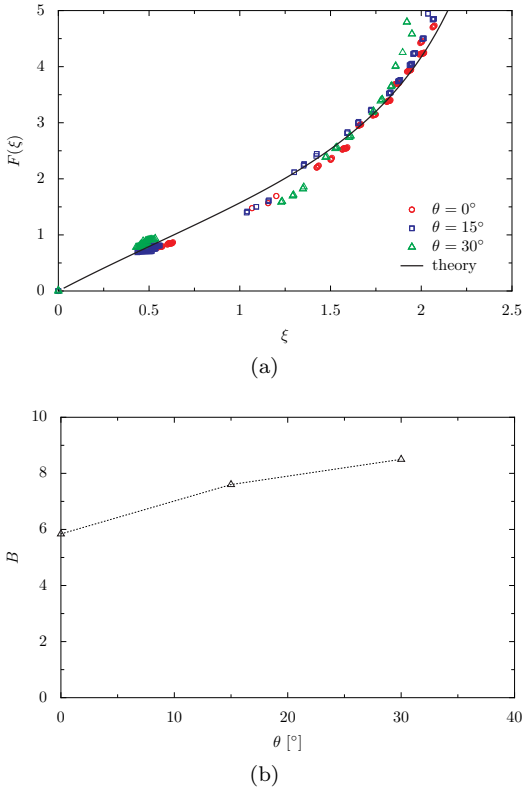

Figure 3.7: (a) Dimensionless rivulet profile $F(\xi)$ defined in equation (3.19) for $w = 3$ mm, $\mu = 19.2$ mPa·s obtained using the fitted values of the parameter $B(\theta)$, shown in (b). The numerical predictions are compared with the theory (3.23) computed for $W = 3.4$

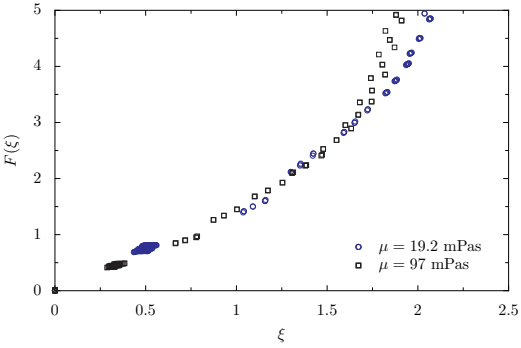

(a) $\theta = 15°$, $w = 3$ mm.

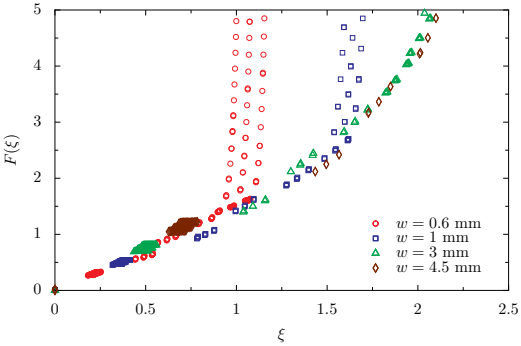

(b) $\theta = 15°$, $\mu = 19.2$ mPa·s.

Figure 3.8: Dimensionless rivulet profile $F(\xi)$ defined in equation (3.19) for (a) various viscosities and (b) capillary sizes.

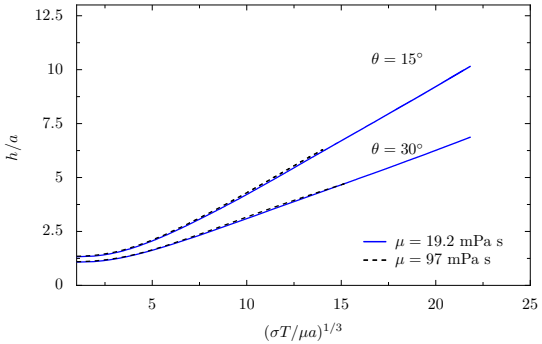

Figure 3.9: Effect of viscosity and contact angle on the dimensionless corner rise h/a for the width of the capillary $w = 3$ mm.

The dimensionless rate of the rivulet growth K, mentioned in equation (3.25), is of order unity and can be written as,

$$K = c_1 \frac{(g\mu\rho)^{1/3}}{(A\sigma)^{2/3}}, \tag{3.26}$$

where, c_1 is one of the fitting parameters of the equation $H = c_1 T^{1/3} + c_2$ used in fitting the evolution of rivulet tip. Since the equation (3.25) is obtained from the similarity solution (3.19), which is not valid near the bulk meniscus, the influence of capillary size cannot be ascertained from equation (3.25). The influence of the size is introduced through the initial rivulet thickness δ_o near the bulk meniscus, which can be estimated from geometrical considerations

$$\delta_o \approx \frac{\sqrt{2}}{2} w - R_o. \tag{3.27}$$

The dependence of the computed values of K on the ratio δ_o/a is shown in Figure 3.10. The rate of the rivulet growth K slightly increases with δ_o/a thus showing that the influence of capillary size is relatively weak. It is remarkable that the obtained values of K almost do not depend on the contact angle.

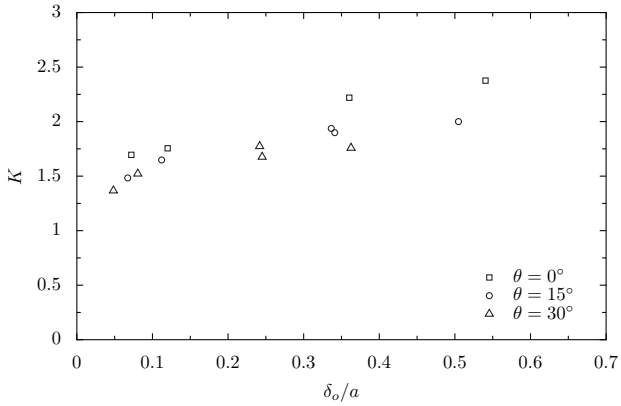

Figure 3.10: Computed values for the dimensionless rate K of the rivulet rise in a corner, defined in (3.25). Dependence on the wall contact angle and the dimensionless initial rivulet thickness δ_o/a.

3.4 Summary

In this chapter, the spontaneous rise of rivulets in a square capillary under gravity is investigated using numerical simulations. Unlike the circular capillary where there is only bulk flow, the corners in the square capillary enhance the capillary effects, which results in the rise of rivulets when $\theta < \pi/4$. These rivulets rising in the corner precede the bulk flow, and thus in a square capillary for $\theta < \pi/4$, there is both bulk flow and rivulet flow.

Based on the observations from the simulations, the growth of the rivulet can be split into two stages. In addition to the rivulets rising in the corners, there is also the bulk flow in the early stage, where they both share the same capillary pressure at the bulk meniscus. This situation is called the compound capillary flow and here it is dominated by the bulk flow. Hence, the early stage of the rivulet flow follows the same trend as the bulk flow. When the bulk rise starts relaxing towards a static height during the visco-gravitational regime, the rivulet flow starts its transition towards the pure corner flow. Shortly after the bulk flow reaches equilibrium, the rivulets enter the late stage, where it rises according to the one-third asymptotic: $H \sim T^{1/3}$. This one-third law was

also experimentally observed in the capillary rise in corners of different geometries.

In the late stages, three different spatial regions in the the rivulet profile could be identified. The first spatial region of the rivulet is close to the bulk meniscus, hence influenced by the bulk flow, i.e., by the shape of the bulk meniscus. The intermediate region is located slightly above the bulk meniscus and it approaches a near static shape at long times. Neglecting the curvature of the rivulet along the axial direction the thickness of the rivulet is computed theoretically, which agrees with the simulations. The third region is close to the rivulet tip, which is self-similar. The flow in this region is described using the lubrication approximation, where a similarity solution is obtained by matching with the intermediate region. The thickness of the rivulet profile obtained from the solution is compared with the computed profiles. Good agreement between them is observed in the region close to the tip, but close to the bulk meniscus the solution and the computed profiles disagree, because the similarity solution is not valid near the bulk meniscus.

Finally, a scaling for predicting the rate of rivulet growth is proposed. The dependence of the dimensionless growth rate K on the dimensionless initial rivulet thickness δ_o/a obtained from the numerical simulations shows that the function $K(\delta_o/a)$ is almost independent of the contact angle, liquid viscosity or surface tension.

4 Spontaneous rise in open rectangular channels

This chapter presents the numerical investigation of the spontaneous rise in an array of connected open rectangular channels. In addition to the rivulets in the interior corner, the capillary rise on the outer face connecting the two neighbouring channels as well as inside the channel and on the outer corner are also analysed. The effect of parameters such as contact angle, the dimensions of the channel and also the width of the outer face on the capillary rise are characterized.

The description of the computational setup used in the simulations is presented in section 4.1. Section 4.2 describes the general features of the flow, and in section 4.3 the dynamics of capillary rise inside the channel is presented. The capillary rise on the outer face and the meniscus behavior on the outer corner are discussed in section 4.4. Finally, the results are summarized in section 4.5.

This Chapter is based on the article *Spontaneous rise in open rectangular channels under gravity* by V. Thammanna Gurumurthy et al. (2018), published in Journal of Colloids and Interface Science.

4.1 Computational setup

The computational domain shown in the Figure 4.1, consists of a rectangular column. The height L_z of the domain is chosen as 30 mm, which is long enough for the rivulet rise to stay inside the domain. Since the channel is symmetric only one half of the channel is simulated, which makes the width L_y equal to $(F + W)/2$. The depth L_x of the domain is set to $D + 12$ mm, which is the minimum length required such that the effects of the wall bounding the domain away from the channel on the capillary rise are minimal.

Both front and back faces of the domain have symmetry boundary

conditions, while the right face at the far end has no-slip and zero pressure gradient boundary conditions. The left face, which includes the channel walls and the outer face, has constant contact angle and no-slip boundary condition. The geometry of the channel is characterized by its aspect ratio

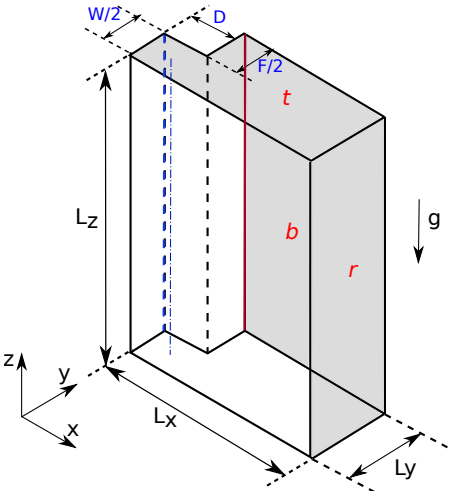

Figure 4.1: Computational domain. The labels **b**, **r** and **t** indicate the back, right and top faces (shaded in grey) of the domain respectively. The blue dashed and dash-dotted lines represent the line along which the meniscus height in the center and in the corner of the channel is measured. The meniscus height on the outer face is measured along the red line.

ϵ, defined as the ratio of depth D to width W. In addition to that, the width of the outer face F connecting the channels is also included. Table 4.1 lists the dimensions and the aspect ratio of the channel considered in this study. It also shows the corresponding ratio of Ohnesorge number ($Oh = \mu/\sqrt{\rho\sigma W}$) to Bond number ($Bo = \rho g W^2/\sigma$) defined using the width of the channel as the characteristic length. The influence of outer face width F is also studied by varying it ($0.5-12$ mm) while keeping both the channel depth and width at 3 mm. Polydimethyl siloxane (PDMS-20cSt) is used as the liquid in this simulations, whose properties are given in Table 3.1. The contact angles considered in this study are 0°, 15°, 30°, 45° and 60°. The liquid-gas interface is resolved using adaptive mesh

refinement. Based on the grid convergence tests, the mesh size is chosen as 31.25 microns.

Table 4.1: Dimensions of the channel

D (mm)	W (mm)	F (mm)	$\epsilon = D/W$	Oh/Bo
0.25	3.00	3.00	0.08	0.02
0.50	3.00	3.00	0.17	0.02
0.75	3.00	3.00	0.25	0.02
1.50	3.00	3.00	0.50	0.02
3.00	3.00	3.00	1.00	0.02
3.00	1.50	3.00	2.00	0.11
3.00	0.75	3.00	3.00	0.63

The effect of face width is also studied by varying it in the range of $0.5 - 12$ mm while keeping both the D and W constant at 3.00 mm.

4.2 General features of the flow

The capillary rise inside the channel is characterized by measuring the height of the meniscus above the free surface in the center (blue dash-dotted line in Figure 4.1) and in the corner (blue dashed line in Figure 4.1). The height measured in the center of the channel is representative of the bulk flow and the height measured in the interior corner represents the rivulet flow. The rise of meniscus in the center of the outer face (red line in Figure 4.1) is also measured to characterize its behaviour. The liquid level in the domain is initialized to 8 mm from the bottom of the channel, and with a flat interface. Once the simulation starts, the wetting boundary conditions imposed on the channel wall take effect making the flat interface depress, forming a meniscus, after which it starts to rise. The duration of this meniscus forming stage is approximately 0.01 s. The liquid height measured in the channel during this stage actually decreases below the initial liquid level and then begins to rise above it. Hence, we start measuring the liquid height once it rises above the initial liquid level and set $t = 0$ at this instant.

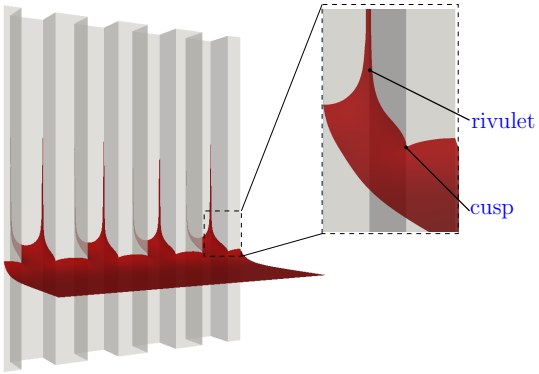

Figure 4.2: Meniscus shape in the open channel of dimensions:$W = D = F = 3$ mm at $t = 15$ s for $\theta = 30°$. The inset figure shows the zoomed-in view of a single channel, where a rivulet rising in the interior corner and a cusp formed at the outer corner can be seen.

Figure 4.2 shows a snapshot of capillary rise in the open channel ($W = D = F = 3.00$ mm) at $t = 15$ s for $\theta = 30°$. The initially flat surface at $t = 0$ s depresses, forming a meniscus and creating an underpressure, which results in capillary rise. When the capillary force driving the meniscus is balanced by gravity, the meniscus reaches equilibrium everywhere, excluding the interior corner of the channel (if $\theta < 45°$). The meniscus close to the interior corner results in the rise of rivulets, since the contact angle is below the threshold criteria [76] ($\theta < 45°$) for the formation of rivulets. While rivulets are formed in the interior corner, at the exterior corner between the outer face and the channel wall, the meniscus depresses, forming a cusp as shown in the inset Figure 4.2. When $\theta \geq 45°$, no rivulets are formed in the interior corner and a smooth meniscus on the outer corner as seen in the Figure 4.3. These observations agree with the theory for the formation of rivulet [76] and cusp [77]. Figure 4.4 shows the temporal evolution of liquid heights measured inside the channel and on the outer face for $\theta = 30°$. Everywhere the liquid column oscillates in the initial stages due to inertia [35, 36], which decays as the viscous friction sets in. Thereafter it reaches equilibrium rapidly, attaining a fixed height except in the interior corners.

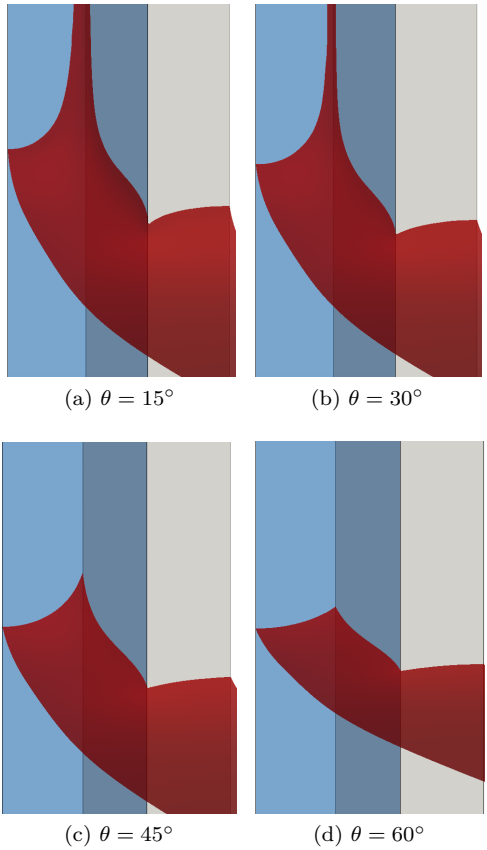

(a) $\theta = 15°$ (b) $\theta = 30°$

(c) $\theta = 45°$ (d) $\theta = 60°$

Figure 4.3: Meniscus shape in the open channel ($W = D = F = 3$ mm) for different contact angles. The channel walls are shaded in blue and the outer face in grey for clarity.

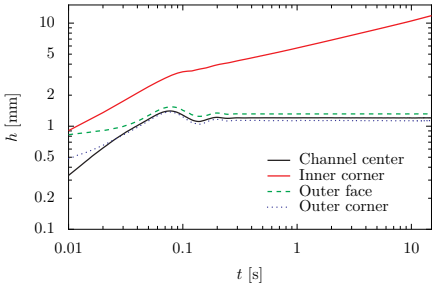

Figure 4.4: Temporal evolution of meniscus height measured inside the channel ($W = D = F = 3$ mm) and on the outer face at $\theta = 30°$.

4.3 Capillary rise inside the channel

4.3.1 Bulk flow

The approach used to model the dynamics of capillary rise in circular capillaries (refer section 1.3.2) can be extended to open channels [59]. A short review of the model is described below.

Consider a rectangular liquid column of constant cross-section ($D \times W$), and length h with a flat interface rising inside the channel. The forces acting on the liquid column are the same: capillary force driving the liquid opposed by the combination of inerital, viscous and gravitational forces. The fluid is assumed to be confined to the channel, completely filling its depth and with no fluid outside the channel. Further, assuming a fully developed, one-dimensional flow and a static advancing angle, the force balance on the liquid column, when simplified, results in an equation in terms of the liquid height h,

$$\frac{d}{dt}\left(h\frac{dh}{dt}\right) + \frac{k\mu}{\rho W D}h\frac{dh}{dt} + gh = \frac{\sigma\left((1+2\epsilon)\cos\theta - 1\right)}{\rho D}. \tag{4.1}$$

The capillary force driving the liquid is defined as the rate of the change in the free energy due to the liquid flow in the z-direction,

$$F_\sigma = -\frac{dE}{dz} \tag{4.2}$$

The change in free energy E due to the liquid filling a distance z of the empty channel is,

$$E = A_{LG}\sigma + (\sigma_{LS} - \sigma_{SG})A_{SL}. \tag{4.3}$$

The terms A_{LG} and A_{LS} represent the area of the liquid-gas and solid-liquid surfaces respectively. For a rectangular channel of width W and depth D, the liquid-gas and solid-liquid areas are $-Wz + DW$ and $2Dz + Wz$ respectively. Now using the areas and Young's relation (1.2) the free energy in the above equation simplifies to,

$$E = \sigma\left[-Wz + Dw + (2Dz + Wz)\cos\theta\right]. \tag{4.4}$$

The capillary force is,

$$F_\sigma = \sigma W\left[(2\epsilon + 1)\cos\theta - 1\right]. \tag{4.5}$$

The friction factor k is calculated by solving the fully developed flow in an open rectangular channel assuming no-slip at the channel walls and shear free liquid-gas interface at the open face. The expression for the friction factor k derived in [71] is given below,

$$k = \frac{1}{\epsilon^2 f(\epsilon)}, \tag{4.6}$$

where f is a function of aspect ratio ϵ given by,

$$f(\epsilon) = \frac{128}{\pi^5}\sum_{2n+1}^{\inf}\frac{1}{n^5}\left[\frac{n\pi}{4\epsilon} - \tanh\left(\frac{n\pi}{4\epsilon}\right)\right]. \tag{4.7}$$

Equation (4.1) along with the boundary conditions $h = 0$ and $\frac{dh}{dt} = 0$ at $t = 0$, are numerically solved using the standard ODE solver available (*scipy* package) in Python.

The liquid column rising inside the channel eventually reaches equilibrium at a fixed height h_o [59, 133] given by,

$$h_o = \frac{\sigma\left[(1 + 2\epsilon)\cos\theta - 1\right]}{\rho g D}. \tag{4.8}$$

The assumptions made in this model impact its comparison to the simulation results. The model assumes a liquid column with constant

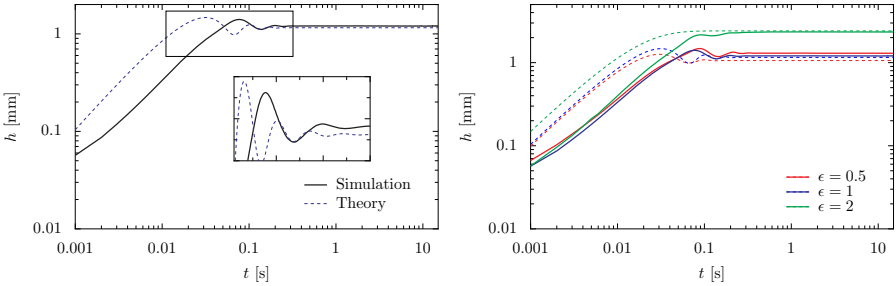

Figure 4.5: Comparison between theory (equation 4.1) and simulation for the evolution of meniscus height in the center of the channel at $\theta = 30°$. (a) For the open channel $W = D = F = 3$ mm and (b) For different aspect ratios (refer Table 4.1). The dashed lines represent the theoretical solution and the solid lines represent the simulation.

cross-section which completely fills the channel, and it does not account for the fluid external to the channel. This impacts the calculation of the viscous force on the fluid filling the channel, assuming a shear free boundary condition at the model interface, instead of a continuous shear stress across the transition between the fluid in the channel and that outside the channel. In addition, by assuming a flat interface at the top of the column, the actual shape of the meniscus is neglected in the model. This introduces an error in the predictions of the model for the gravitational and capillary forces, which in turn affects equilibrium height (h_o) prediction. For channels with dimensions much smaller than the capillary length ($\approx 200-500\ \mu$m), equation (4.8) agrees with the experimentally measured heights reported in the literature [59, 133]. The constant contact angle assumption made in this model, as discussed in section 1.3.2 leads to over prediction of the rate of rise.

Figure 4.5a compares the temporal evolution of meniscus height calculated from the simulation and the theory, at $\theta = 30°$. The liquid height at the start is lower for the simulation, which is mainly due to the initial meniscus height imposed in the simulation as explained in section 4.1. Despite the difference in initial height, both have the same rate of rise in the inertial regime, where the meniscus rises with a constant velocity. Be-

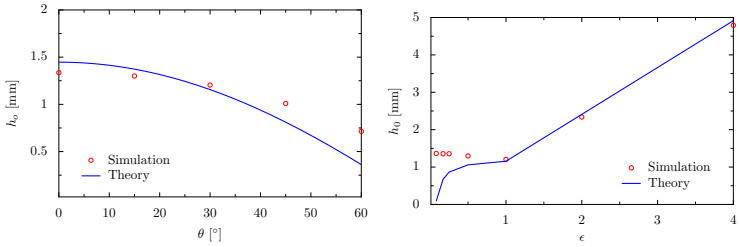

Figure 4.6: Comparison between theory (equation 4.8) and simulation for the equilibrium height. (a) For different contact angles in the open channel of dimensions: $W = D = F = 3$ mm. (b) For different aspect ratios (refer Table 4.1) at $\theta = 30°$.

cause of the shear free assumption at the channel open face, the friction factor k used in the model (4.1) underpredicts viscous drag and allows slightly larger oscillations (see the inset plot in Figure 4.5a) than the simulation. These inertial oscillations occur only when $Oh/Bo \ll 1$ [44]. The liquid reaches equilibrium immediately at the end of oscillations where the equilibrium height h_o computed in the simulation is very slightly higher than the theoretical height. Figure 4.5b also compares the height evolution between theory and simulation for different channel aspect ratios at $\theta = 30°$. Increasing the aspect ratio decreases the oscillations which again agrees with the criteria $Oh/Bo \ll 1$.

Figure 4.6 compares the equilibrium height between the simulations and the theory (equation (4.8)) for different contact angles and aspect ratios of the channel. At higher contact angles and at lower aspect ratios the theoretical height (4.1) is lower than the computed values. This disagreement can be attributed to the limitations of the model as described above. Furthermore, the computations show that decreasing the aspect ratio (Figure 4.6b) by decreasing the channel depth does not alter h_o. This weak dependence on the shallow channel depths was also observed in [133].

4.3.2 Rivulet flow

The rise of rivulets in the early stages when the bulk meniscus is also rising, is coupled with the bulk rise, as they share the same capillary pressure at the bulk meniscus [130]. As the bulk rise enters the visco-gravitational regime, it slows down, during which the rivulets slowly begin the transition to the corner flow regime. In the previous chapter, the time to reach 90% ($t_{90\%}$) of the equilibrium height h_0 was taken as the beginning of this transition stage. Here the same convention is followed, except for the cases where inertial oscillations are observed. In those cases, the transition time is taken as the time when the oscillations have disappeared. The height of the rivulet tip H is measured from the center of the bulk meniscus and the time origin is shifted as $T = t - t_{90\%}$. Figure 4.7 shows the

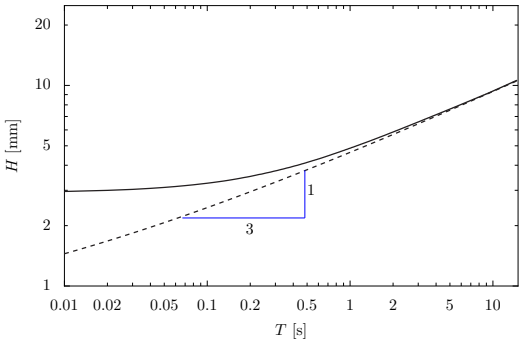

Figure 4.7: Temporal evolution of rivulet tip height in the open channel ($W = D = F = 3$ mm) at $\theta = 30°$. The dashed line is one third asymptotic fit obtained using least-squares method.

evolution of rivulet height at $\theta = 30°$, which enters the pure corner flow regime shortly after the bulk rise has reached equilibrium. In this regime, it rises according to the power-law, $H \sim T^{1/3}$, as shown in previous studies on grooves and other geometries [93–95, 134]. At long times, the rise of rivulets is characterized by its non-dimensional growth rate K calculated using the scaling relation (3.26) derived in the previous chapter. The fitting constant c_1 used in equation (3.26) is obtained from fitting H (from the simulations) with a least squares fit of the form: $c_1 T^{1/3} + c_2$, and B is the friction factor accounting for the influence of the contact angle. The values of B calculated in the previous chapter for square capillaries are

used here. Figure 4.8 compares the rise of rivulets in channels of different channel aspect ratios ϵ at $\theta = 30°$, where the growth rate K (inset plot in Figure 4.8) decreases slightly with increasing aspect ratio. Note that the influence of geometry comes through the thickness of the rivulet δ_o at its origin, i.e. close to the bulk meniscus.

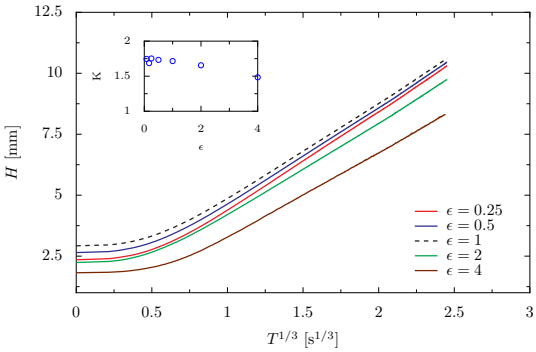

Figure 4.8: Temporal evolution of rivulet height in channels of different aspect ratios (refer Table 4.1) at $\theta = 30°$. The inset plot compares the non-dimensional rate K of rivulet growth with the aspect ratio.

Determining δ_o for open channels is complicated, hence δ_o is calculated based on the equivalent square capillary size w using equation (3.27). The radius of the bulk meniscus R_o, which in case of open channels can be approximated as $W/(2\cos\theta)$. The use of channel width over the depth is chosen since the capillary rise in the channel is weakly dependent on the depth [133]. The equivalent capillary size w is then calculated from the relation (3.12).

Figure 4.9 shows the dependence of rivulet rate on the rivulet thickness for the square capillaries (open) and the open channels (shaded) respectively. For $\delta_o/a \leq 0.3$, the rate K remains the approximately the same for both the geometries (square capillary and open rectangular channel), however at higher values the growth rate is slightly higher for open channels.

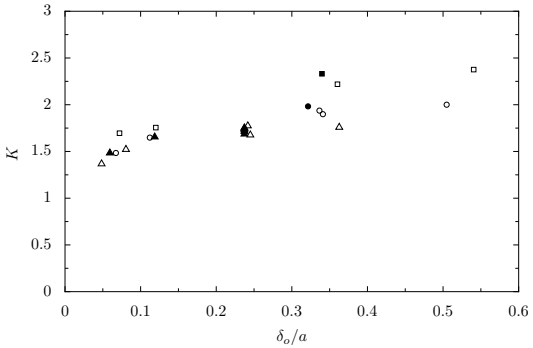

Figure 4.9: Dependence of rivulet growth rate K on the dimensionless thickness of the rivulet δ_o/a for square capillaries (open) and open channels (filled) respectively. The different symbols represent the different contact angles (square − 0°, circle − 15°, triangle − 30°).

Table 4.2: Equilibrium height inside the channel for different face widths at $\theta = 30°$. The channel width and depth was kept constant at 3.00 mm.

F (mm)	0.50	0.75	1.50	3.00	6.00	9.00	12.00
h_0 (mm)	1.19	1.19	1.20	1.20	1.21	1.21	1.21

4.3.2.1 Effect of outer face width

The effect of outer face width on the capillary rise inside the channel was also quantified by varying its width, with the channel depth and width held constant at 3.00 mm. The face width was varied between one-third to eight times the capillary length. Figure 4.10 shows the variation of the rivulet height and Table 4.2 lists the equilibrium height measured inside the channel for different face widths. Both the bulk rise inside the channel and the rivulet rise in the interior corner remain approximately the same for all face widths investigated (only 0.1% variation). Thus, for the channel sizes investigated, the capillary rise inside each channel in an array of connected channels can be modelled as though they were single and isolated.

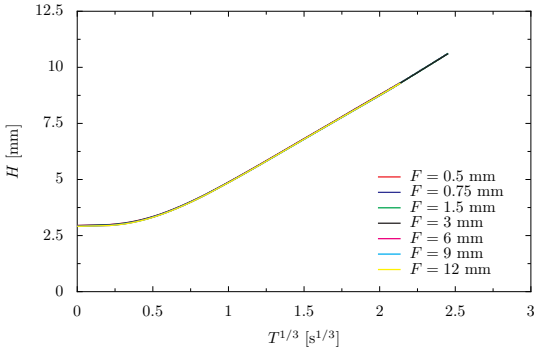

Figure 4.10: Rivulet rise in the interior corner for different face widths.

4.4 Capillary rise on the outer face and outer corner

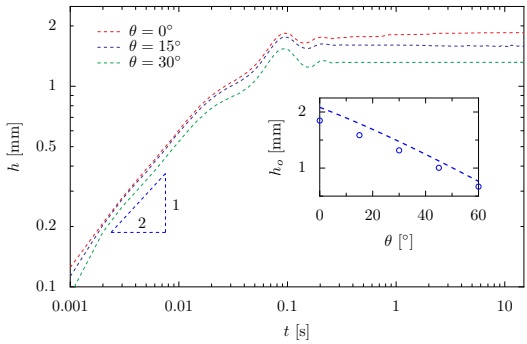

Figure 4.11: Temporal evolution of meniscus height at the center of the face for different contact angles in the open channel ($W = D = F = 3$ mm). The inset plot compares the equilibrium height h_0 between theory (dashed line) for rise against a planar wall and simulations (circles).

The dynamics of meniscus rise on the outer face is similar to the rise against an infinite planar wall [135, 136]. Figure 4.11 shows the temporal evolution of the meniscus height measured at the center of the face for different contact angles (3 mm × 3 mm × 3 mm). Inertia dominates

the early stages, where the meniscus rises according to the power-law: $h \sim t^{1/2}$ [136]. As seen in the inset Figure 4.11, at the end of oscillations the meniscus reaches equilibrium, where it attains a constant height close to that for an infinite planar wall given by $a\sqrt{2(1-\sin\theta)}$. From Table 4.3, it can be concluded that varying the channel aspect ratio does not influence the capillary rise on the outer face.

Table 4.3: Meniscus height measured inside the channel and on the outer face at equilibrium for different channel aspect ratios at $\theta = 30°$. The dimensions of the channel corresponding to the aspect ratio are listed in Table 1 in the article and the outer face width was kept constant at 3.00 mm.

	Equilibrium height (mm)		
ϵ	Channel center	Outer face	Outer corner
0.08	1.36	1.40	1.56
0.17	1.36	1.41	1.50
0.25	1.36	1.39	1.55
0.5	1.30	1.36	1.30
1.00	1.20	1.32	1.13
2.00	2.34	1.41	1.54
4.00	4.79	1.46	1.83

While rivulets are formed in the interior corner, the meniscus at the outer corner forms a cusp, as shown in the Figure 4.2. As described in section 1.3.4, the general condition for observing smooth meniscus on the corners of a rod is $3\pi/2 > \theta + \alpha_o > \pi/2$, where α_o is the half-angle of the outer corner [77]. This cusp is formed due to the strong positive capillary pressure generated by the meniscus as it nears the corner, which squeezes the liquid out. For the right angled corner ($\alpha_0 = 45°$) found here, a cusp is formed when $\theta < 45°$ and a smooth meniscus otherwise (see Figure 4.3). Note that the criteria for the formation of cusp is surprisingly the same as for the rivulet formation here.

The general condition for cusp formation at the outer corner is derived assuming the capillary force acting on either faces are the same. However in our geometry, the outer corner is formed between one of the channel walls and the outer face, where the capillary force on its sides are different. The capillary force on the outer face depends only on the contact angle,

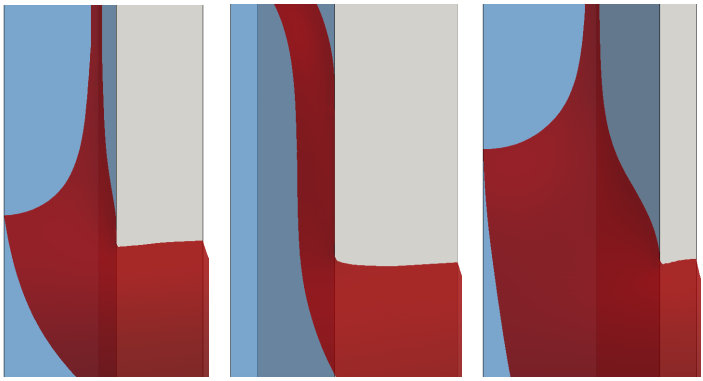

(a) $D = 0.75$ mm (b) $W = 0.75$ mm (c) $F = 0.75$ mm

Figure 4.12: Effect of change in dimensions of the channel or the outer face on the meniscus near the outer corner. The other dimensions were held constant at 3 mm and $\theta = 30°$ The channel walls are shaded in blue and the outer face in grey for clarity.

while inside the channel it also depends on the channel size. Thus when the channel size is larger than the capillary length ($\approx 2a$), the capillary force inside the channel is weak and also approximately equal to the force on the outer face, which results in the cusp as dictated by theory (refer Figure 4.2). But when any one or both of the channel dimensions are less than the capillary length, the capillary force inside the channel is higher than on the outer face, which leads to the meniscus at the outer corner being pulled up. This results in the formation of smooth meniscus even when $\theta < 45°$. Figure 4.12 illustrates such a scenario, where the dimensions of either the channel (depth or width) or the outer face is kept at 0.75 mm ($< a$). The meniscus arches slightly upwards when either W or $D < a$. Surprisingly, this smooth meniscus is also formed when for $F < a$ even if the channel size is above the capillary length.

4.5 Summary

In this chapter, the spontaneous rise of a Newtonian liquid in an array of connected, open rectangular channels is investigated using numerical simulations. The effect of channel aspect ratio, outer face width and the contact angle on the capillary rise inside the channel, on the outer face are analysed. The dynamics of the rise is characterized by measuring the meniscus height inside the channel and on the outer face.

The dynamics of the capillary rise inside the channel is compared with the one-dimensional model and a reasonable agreement is seen. Note that the model does not consider the rivulets in the corners and also the meniscus shape. Due to the latter limitation, the model underpredicts the equilibrium height especially at higher contact angles and also at shallow channel depths [133].

For $\theta < 45°$, rivulets are formed in the interior corner, which at long times grow according to the power law: $H \sim T^{1/3}$ as observed in the square capillary and also in literature for corners formed between different geometries [93–95]. Even though the rise of rivulets is universal, the simulations reveal that it is weakly dependent on the channel geometry. Increasing the channel aspect ratio increases the rate of rise only slightly as as observed in the previous chapter for square capillaries. This weak geometrical dependence comes through the rivulet thickness close to the bulk meniscus in the corner, where it originates. Further, a comparison between the open channels to its equivalent square capillaries show that the rivulet growth rate is slightly higher for the open channels.

The dynamics of meniscus rise on the outer face connecting the channels is similar to the rise against an infinite planar wall. The results agree with the theory for the equilibrium height and also with the recent findings [136] regarding its rise dynamics.

Varying the outer face width has no influence on the both the bulk and the rivulet rise inside the channel. This result leads to the conclusion that the even in a network of connected channels, the capillary rise in each channel behaves as though they were single and isolated. Similarly, varying the channel aspect ratio has negligible influence on the capillary rise on the outer face. Based on these results, it can be concluded that the coupling between the channel and outer face is almost non-existent for sizes larger or closer to capillary length.

The outer corner formed between the channel wall and the outer face have different capillary strengths on its either side. Surprisingly, it behaves as typical outer corner, when the forces on either side are nearly equal i.e, when the length scales are larger than the capillary length. A cusp is formed at the outer corner when $\theta < 45^\circ$ and a smooth meniscus otherwise [77]. But when the any one of the dimensions of either the channel or the outer face is smaller than the capillary length, a smooth meniscus is formed even when $\theta < 45^\circ$.

5 Forced wetting in square capillaries

In this chapter, two different cases of forced wetting are studied using square capillaries. In both cases, the long-time behaviour of the flow either in the bulk or in the rivulet under the influence of various parameters is of the main interest.

In the first case, liquid is pumped into the capillary at a constant flow rate and its effect on the dynamics of rivulets is discussed in section 5.1. The computational setup and the procedure are first described, which is followed by the discussions on the effect of various parameters on the rivulet dynamics. Using the lubrication approximation, the flow inside the rivulet is modelled in a similar fashion like in Chapter 4, where it was validated for spontaneous rise. In addition to the rivulets, the variation of apparent contact angle with the capillary number calculated from the bulk meniscus shapes is also discussed.

In section 5.2, the forced wetting by immersion of the square capillary is presented. First the experimental procedure and the setup used are described. The one-dimensional model described in section 1.3.2.2 for capillary rise is extended for this forced wetting situation, and compared with experiments. Using the model, the variation of the meniscus speed under immersion for different Bond numbers is presented. Finally, the results from the two cases are summarized in section 5.3.

5.1 Capillary pumping

The first case of forced wetting focusses on the dynamics of rivulets, where liquid is continuously pumped into the capillary at a constant flow rate. The influence of capillary size, liquid viscosity and the contact angle on the rivulet is studied. This forced wetting case is similar to the forced wetting experiments [20, 137–139] and other theoretical studies [96, 97, 110, 140, 141] conducted in cylindrical capillaries or slots between parallel plates, where the relationship between the apparent contact angle and the capillary number was studied.

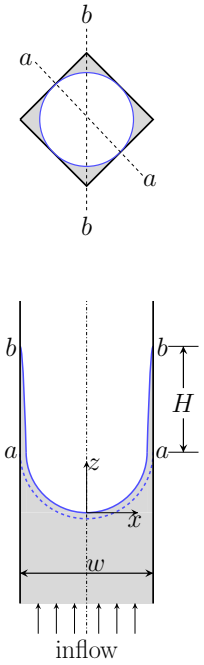

Figure 5.1: Schematic illustrating the capillary pumping. The dashed and solid blue lines represent the meniscus shapes along the center plane $a - a$ and the diagonal plane $b - b$.

5.1.1 Computational setup

Numerically, the forced wetting is achieved by continuously feeding the liquid from the bottom of the capillary at a constant volumetric flow rate, as shown in the Figure 5.1. The computational domain is the same as the one used for spontaneous wetting, which is described in section 3.1. The only change is in the inflow boundary condition at the bottom of the capillary, where the pumping speed U_o is specified. Since the capillary size is constant, varying the volumetric flow is essentially the same as changing the pumping speed. The capillary sizes chosen for this study are 0.6, 1, and 3 mm, whose mesh sizes and Bond numbers are given in section 3.1. The liquids used here are PDMS-20cSt and PDMS-100cSt, whose properties are given in Table 3.1.

Here, the capillary number is used as the scaling for the pumping speed, as conventionally done in the forced wetting studies [20, 96, 97, 110, 137–141], instead of the volumetric flow rate. The effect of the parameters such as capillary size and the contact angle on the rivulet height under varying Ca are also studied.

Initial observations Shortly after the start of the simulation (pumping), the flow reaches steady state, where the meniscus attains a shape, which remains constant thereafter and the meniscus rises at the pumping speed. Since in a square capillary rivulets form when $\theta < 45°$, two different meniscus profiles exists: one along the center plane $a - a$ and one along the diagonal plane $b - b$, which includes the rivulet, as shown in the sketch of Figure 5.1. The steady state is identified by monitoring the meniscus heights along the two planes measured relative to the center of the bulk meniscus. The meniscus profile in the steady state is used to characterize the flow.

5.1.2 Steady rivulet propagation at long times

Effect of initial interface shape Even though studies [142] have shown that the steady state interface shape in cylindrical capillaries is independent of initial conditions, it is essential to verify the same in the square capillary. The forced wetting here can be started either with a flat interface or with a developed meniscus where the rivulet has risen to a certain height. For the latter case, the simulation is started under the spontaneous rise mode for a few seconds, after which the forced wetting is started. Varying the duration of the spontaneous rise mode will vary the rivulet height available at the start of the forced wetting.

Figure 5.2 compares the temporal variation of the meniscus height along the two planes for the two different initial interface shapes at $Ca = 0.01$ for $w = 1$ mm and $\theta = 30°$. The liquid heights along the two planes at steady state are the same for the two cases, showing that the steady state characteristics of the flow are independent of the initial interface shape. This fact is also confirmed by the Figure 5.3, which illustrates the shape of the meniscus along the two planes remain the same for both cases. The only difference between the two initial shapes is in the time to reach the steady state along the diagonal plane, which varies due to the initial rivulet length. Starting with a flat interface shape the steady state can

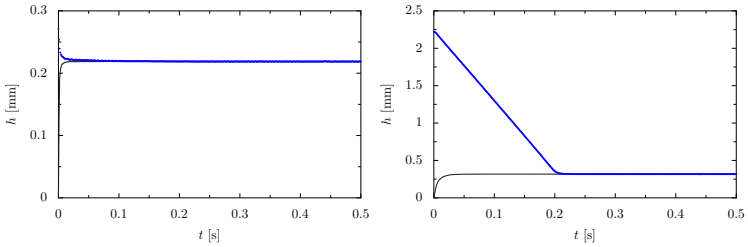

Figure 5.2: Effect of initial shape of the interface on the temporal variation of meniscus heights measured along the center plane $a - a$ in (a) and the diagonal plane $b - b$ in (b), at $Ca = 0.01$ for $w = 1$ mm and $\theta = 30°$. Both heights are measured relative to the center of the bulk meniscus. The solid lines in blue and black represent the two different initial conditions a flat interface and a developed meniscus respectively.

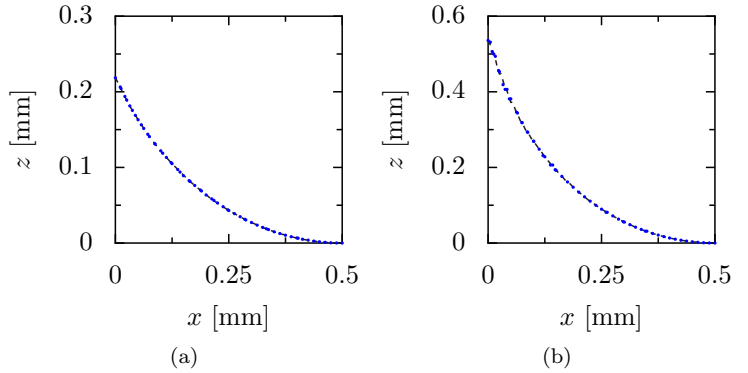

Figure 5.3: Effect of initial shape of the interface on steady state shape of the interface along the center plane $a - a$ in (a) and the diagonal plane $b - b$ in (b) at $Ca = 0.01$ for $w = 1$ mm and $\theta = 30°$. The dotted line in blue and the dashed line in black represent the two different initial conditions a flat interface and a developed meniscus respectively.

be quickly attained than with some initial rivulet length.

Parametric study Figure 5.4 compares the variation of rivulet height with the capillary number for different viscosities, capillary sizes and contact angles. A general trend observed in these curves is that the rivulet height decreases with increase in capillary number. The rivulet height remains the same for different viscosities, which justifies the choice of using capillary number as the scaling for the speed. The rivulet height increases with increasing capillary size, and decreases with increasing contact angle. These observations are similar to spontaneous rise situations, where the rivulet growth rate increases with capillary size and decreases with contact angle.

5.1.3 Long-wave approximation of the flow inside the rivulet

The flow inside the rivulet here is described using the lubrication approximation in a similar fashion like in the spontaneous rise situation (see section 3.3), where it was validated with the simulations.

Consider now a stationary flow in the rivulet in the coordinate system moving with the rivulet tip with the velocity U_0. In this coordinate system

$$\delta(z,t) = \delta(\zeta), \quad \zeta = U_0 t - z. \tag{5.1}$$

where ζ is the distance to a given point $\{z\}$ from the rivulet tip.

The volumetric flux through the rivulet cross-section in the moving coordinate system is zero. Therefore, the momentum balance equation (3.15) can be written in the form

$$U_0 = -\frac{g\rho\delta^2}{B\mu} + \frac{\sigma A\delta'}{B\mu} \tag{5.2}$$

where $\delta' \equiv \mathrm{d}\delta/\mathrm{d}\zeta$.

The solution of the ordinary differential equation (5.2) subject the initial conditions at the rivulet tip $\delta(\zeta = 0) = 0$ is

$$\delta = \Delta \tan\left[\frac{\sqrt{BCa}\zeta}{Aa}\right], \quad \Delta \equiv \sqrt{\frac{B\mu U_0}{\rho g}}, \quad a = \sqrt{\frac{\sigma}{\rho g}}. \tag{5.3}$$

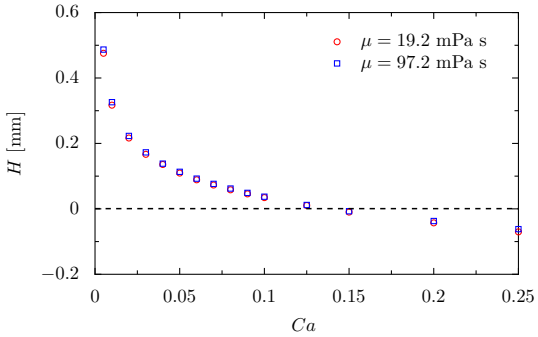

(a) Effect of viscosity at $\theta = 30°$ and $w = 1$ mm.

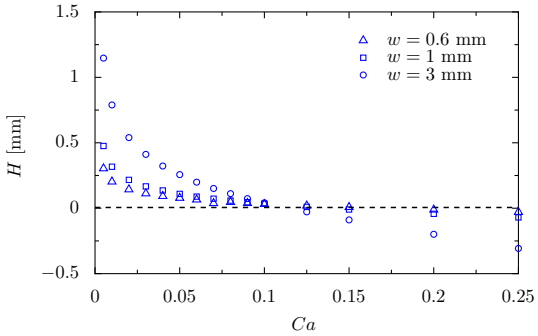

(b) Effect of capillary size at $\theta = 30°$.

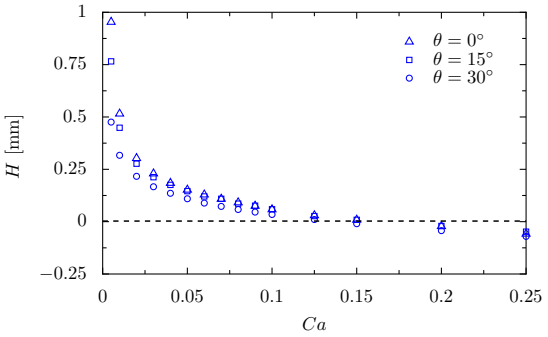

(c) Effect of contact angle for $w = 1$ mm.

Figure 5.4: Effect of the input parameters on the rivulet height at steady state. The dashed indicates the bulk meniscus position at the center of the capillary.

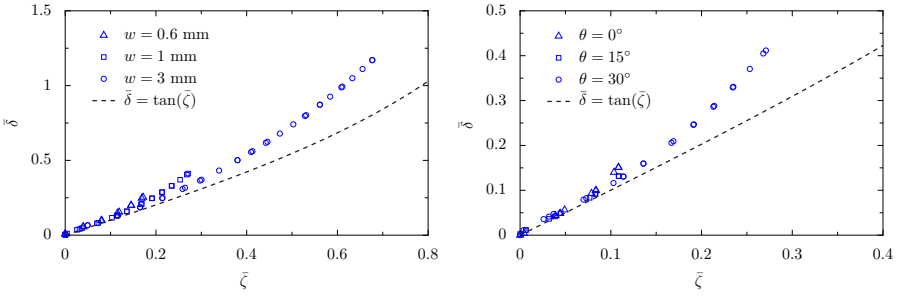

(a) $\theta_s = 30°$ (b) $w = 1$ mm

Figure 5.5: Comparison of the dimensionless rivulet profile predicted by the theory (5.4) with the simulations.

where λ_c is the capillary length. In non-dimensional form,

$$\bar{\delta} = \tan(\bar{\zeta}), \quad \bar{\delta} = \frac{\delta}{\Delta}, \quad \bar{\zeta} = \frac{\zeta\sqrt{BCa}}{Aa}. \tag{5.4}$$

Figure 5.5 compares the dimensionless computed rivulet profile with the equation (5.4), where excellent agreement close to the rivulet tip can be seen.

5.1.4 Variation of apparent contact angle with the capillary number

Forced wetting in capillaries and slots is one of the methods used to study the relationship between the apparent contact angle and the capillary number. The apparent contact angle is calculated here by extrapolating the static shape of the meniscus to the wall and measuring the angle it makes. This extrapolation is done here by fitting the meniscus shape in the outer region with a spherical cap, which is the static shape for the capillary. Using the radius R_{fit} of the fitted spherical cap, the apparent contact angle is calculated as,

$$\theta_D = \cos^{-1}\left(\frac{w}{2R_{fit}}\right). \tag{5.5}$$

The meniscus profile along the plane $b - b$ including the rivulets cannot be used since the curvature of the meniscus varies; the curvature of the meniscus in this plane varies due to the rivulet. So, the meniscus profile along the plane $a - a$ is used for calculating the apparent contact angles. The length of the outer region used for fitting is taken as $w/4$ and the meniscus shape was fitted with a circle, which gives the radius R_{fit}. Varying the length of region used for fitting by 100 μm changes the apparent contact angle by a maximum of 1°.

Figure 5.6a shows the variation of the apparent contact angle with the capillary number at three different microscopic contact angles (0°, 15°, 30°). The variation of the apparent contact angle in the form $\theta_D^3 - \theta^3$ remains nearly the same for all microscopic contact angles studied, and its variation with capillary number is linear as predicted by hydrodynamic theory. The dashed line represents the least squares fit made using the Cox's equation in the form $\theta_D^3 - \theta^3 = cCa$, where c is the fitting parameter. The fitting parameter characterizes the ratio of the inner l_s and outer length scales l_o. The effect of the outer scale length i.e., the capillary size on the apparent contact angle can be seen in the Figure 5.6b, where it increases slightly with the capillary size.

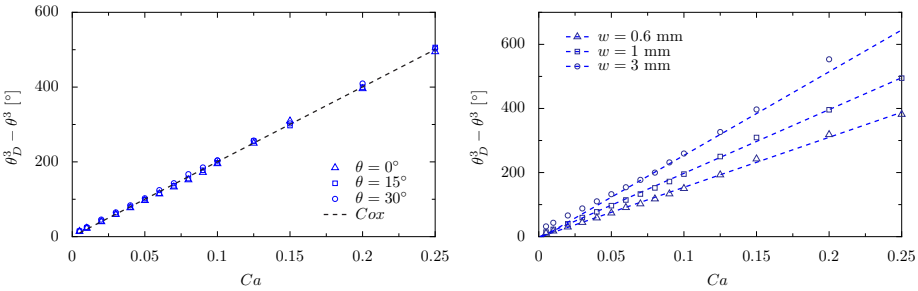

Figure 5.6: Variation of the apparent contact angle versus the capillary number. (a) For different microscopic contact angles for $w = 1$ mm. (b) For different capillary sizes at $\theta = 0°$. The dashed line represents the least squares fit made using the Cox's equation in the form: $\theta_D^3 - \theta^3 = cCa$, where c is the fitting parameter, which includes the ratio of length scales characterizing the inner and outer region.

5.2 Capillary immersion

Consider a square capillary being continuously immersed into a liquid pool at a constant speed U_o, as shown in the Figure 5.7. The viscous friction from the walls of the moving capillary pushes the liquid down trying to drag it as the capillary is steadily immersed. The temporal variation of the meniscus height h_a measured in the center of the capillary above the free surface of the pool is used to characterize the effect of forced wetting.

5.2.1 Experimental setup and procedure

The experiments were carried out in collaboration with Prof. Stephen Garoff, Dept. of Physics, Carnegie Mellon University, Pittsburgh, USA.

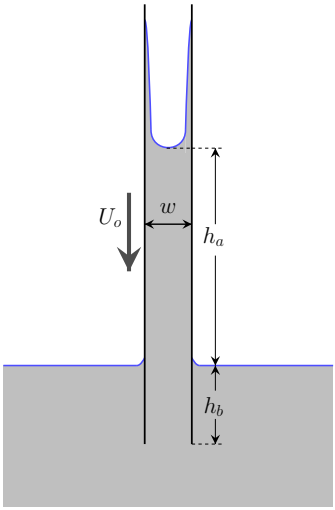

Figure 5.7: Steady immersion of a square capillary

Materials The liquid used for the experiments is methyl terminated PDMS (United Chemicals Technology Inc., 100cSt PS041) whose properties are $\rho = 960 \pm 0.01$ kg/m^3, $\mu = 0.104 \pm 0.005$ Pa s, and $\sigma = 19.9 \pm 0.4$ mN/m. Two square borosilicate glass capillaries (BST-070-14 and BST-070-1, Friedrich and Dimmock Inc.) of size 0.7 ± 0.07 mm and 1 ± 0.1 mm were used. The tubes were cleaned first by rinsing in xylene followed by Nochromix, and finally, rinsed in Millipore water. This treatment produces contact angles between 0° and 5° for PDMS on glass.

Experimental procedure The tubes were mounted vertically, and were translated at speeds from 0.2mm/s to 1.3mm/s by a translation stage (UTM100CC.1 Newport Corporation, Irvine, CA; Newport/Klinger MotionMaster 2000). The liquid was contained in a Teflon beaker, and filled just above its rim. After mounting, the tubes were first lowered until they just touched the surface of the liquid upon

which the spontaneous imbibition began, and the motor was immediately turned off. The spontaneous imbibition was allowed to reach completion. About 20s after the completion of spontaneous imbibition, the forced immersion started where the motor was turned on. The speed of the motor was constant to $\sim$ 5% throughout the forced immersion (see Appendix B). The final motor speeds and acceleration to that final speed were determined using the images of a ruler attached behind the tube. The motor accelerated to its final speed in less than 1s for all the motor speeds used. The meniscus was imaged until it moved below the bulk fluid level in the beaker. During the forced immersion, the varying stresses on tube caused it to flex in some experiments by as much as 15° from the vertical in some experiments. Each experiment was repeated at least two times.

The meniscus was imaged using a digital camera (model QPSCDNV, Q-See CCD Camera) at 30 frames/sec with a telecentric lens (Computar 55mm f/2.8) providing a field of view of 2 cm. The movie of the experiment was analyzed using NIS-Elements AR software. The position of the meniscus above the bulk fluid level in the beaker was chosen to be the lowest point of the bottom of the image of the meniscus which appeared at the center of the tube. The meniscus position was measured right from the start of the immersion.

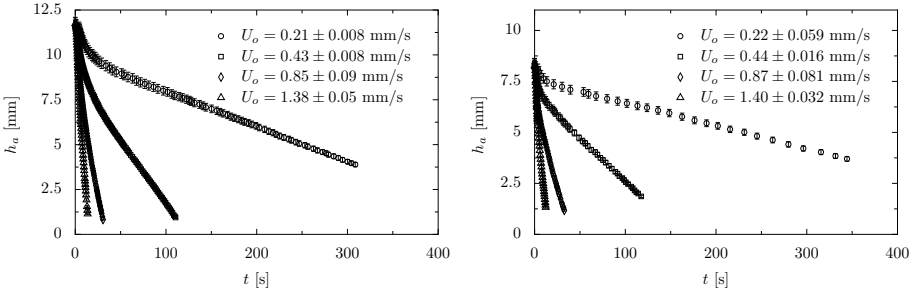

(a) $w = 0.7$ mm (b) $w = 1$ mm

Figure 5.8: Temporal variation of the meniscus height obtained from the experiments for different motor speeds.

Initial observations In Figure 5.8 the temporal variation of meniscus heights measured in the experiments at different speeds in two capillary

sizes are shown. At all speeds, the meniscus height decreases with time, eventually going below the liquid pool. Shortly after an initial period of adjustment, the meniscus height decreases almost linearly with time indicating that the meniscus descends at a constant speed. Thus, there are two stages observed during immersion: early stage where the initial transients occur, and late stage where the meniscus height decreases with a constant speed.

The slope of the curves in the late stage (where it is linear) as seen in the Figure 5.8, shows that the speed of the falling meniscus increases with increasing motor speed U_o. It also shows that increasing the capillary size decreases the speed of meniscus. This constant speed U_a is determined by fitting the linear region of the curves shown in the Figure 5.8 using least squares method. While fitting this linear regime, different portions of the curves (where it is linear) are used and the final constant speed is calculated by averaging the different speeds from these fits. The uncertainty in fitting the different regions is also calculated.

5.2.2 Model for capillary descent

The variation of meniscus height under immersion is modelled here by extending the capillary rise model presented in section 1.3.2.2. The assumptions of the original model also holds here, and the expressions for the forces acting on the liquid column are modified for the square capillary geometry.

The expressions for capillary force and gravitational forces are $4w\sigma\cos\theta$ and $\rho g w^2 h_a$ respectively. The viscous friction acts over the entire length of the liquid column, which in this case includes the height above h_a and below h_b the free surface of the pool (see Figure 5.7). The relative speed of the meniscus is $d(h_a+h_b)/dt$. Combining together, the viscous friction can be expressed as $k\mu(h_a+h_b)d(h_a+h_b)/dt$. The coefficient of friction k, accounting for the geometry, can be obtained from the solution for the fully developed laminar flow in the rectangular cross-section. The coefficient is given by the expression [58],

$$k = \frac{\pi^4}{8D^2}\left\{\sum_{n=0}^{\infty}\frac{1}{(2n+1)^4}\left(1-\frac{\tanh(r(n))}{r(n)}\right)\right\}^{-1}, \quad r(n)=\frac{(2n+1)\pi W}{2D}. \tag{5.6}$$

For a square capillary ($D = W = w$) it gives $k = 28.45$. Substituting all

the terms in the force balance and simplifying results in the equation,

$$\frac{d}{dt}\left((h_a+h_b)\frac{dh_a}{dt}\right) + \frac{7}{6}\pi w\frac{d^2h_a}{dt^2} + 0.225\left(\frac{dh_a}{dt}\right)^2 + gh_a + \frac{k\mu}{\rho w^2}(h_a+h_b)\frac{d(h_a+h_b)}{dt} = \frac{4\sigma\cos\theta}{\rho w}. \tag{5.7}$$

Since the capillary is immersed into the pool at constant motor speed U_o, the height of the liquid column inside the capillary below the pool is $h_b = U_o t$. The above equation is non-dimensionalized using the equilibrium height $h_o \approx (4\sigma\cos\theta)/(\rho g w)$, and the motor speed as the characteristic length and velocity scales

$$\left(\bar{h_a}+\bar{t}+b_1\right)\frac{d^2\bar{h_a}}{d\bar{t}^2} + 1.225\left(\frac{d\bar{h_a}}{d\bar{t}}\right)^2 + \left(\frac{d\bar{h_a}}{d\bar{t}}\right)\left[1+\frac{b_2 k}{ReBo}\left(\bar{h_a}+\bar{t}\right)\right] + \bar{h_a}\left(\frac{b_2 k}{ReBo}+\frac{b_2}{We}\right) + \frac{b_2 k}{ReBo}\bar{t} - \frac{b_2}{We} = 0 \tag{5.8}$$

The non-dimensional numbers used in the above equations are defined using the capillary size and motor speed as length and velocity scales respectively. The terms b_1 and b_2 are constants equal to $7\pi w/6h_o$ and $4\cos\theta$ respectively.

At long times, the inertial forces can be safely neglected, which further simplifies the equation,

$$\frac{d\bar{h_a}}{dt} = \left(\frac{Bo}{kCa}\right)\left(\frac{1-\bar{h_a}}{\bar{h_a}+\bar{t}}\right) - 1. \tag{5.9}$$

Both equations (5.8) and (5.9) do not have an analytical solution. Hence, they are solved numerically using a script written in python.

The model does not consider the rivulets rising in the corners, which are observed when $\theta < 45°$. It has been shown that the presence of rivulets does not introduce any additional dissipation [143], which justifies the model assumption. The equilibrium height used differs from the correct expression (see equation 3.11), but it is not relevant here since it is merely used a length scale for non-dimensionalization.

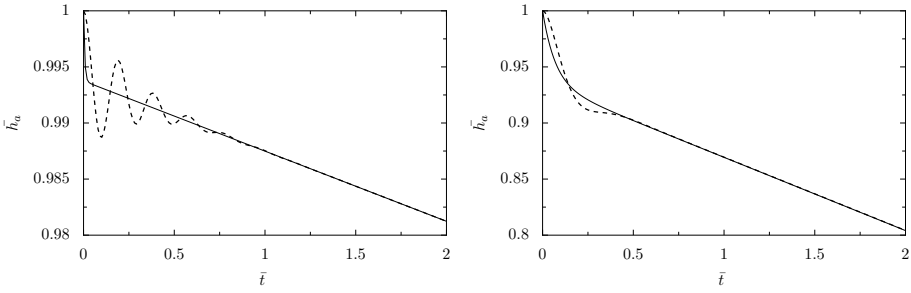

(a) $ReBo = 1.46$ (b) $ReBo = 3.53$

Figure 5.9: Influence of inertial effects on the rising liquid column. Dashed line represents the inertial solution (5.8) and the solid line represents the non-inertial solution (5.9).

Effect of inertia Before using equation (5.9) to predict the rise, it is essential to know the influence of inertia by comparing it with equation (5.8), which includes the inertial effects. Equation (5.8) indicates that the inertial effects will be important only when $ReBo \gg 1$. Figure 5.9 illustrates two such cases, where the inertial effects are amplified by increasing either the Bond number (Figure 5.9a) or the Reynolds number (Figure 5.9b). Increasing $ReBo > 1$ results in inertial oscillations, which are not captured by equation (5.9). These oscillations occur when $Oh/Bo \ll 1$, which is the criteria derived for observing inertial oscillations in spontaneous rise [44]. Despite the inability to capture the inertial oscillations in the early stage, the prediction in the late stage agrees well with the equation (5.8). Thus, for predicting the long-time behavior, equation (5.9) is sufficient.

Effect of initial height Varying the initial height ($h_a(t = 0)$) also affects the early stage behaviour as shown in the Figure 5.10, where three different initial heights are used in equation (5.9). Increasing the initial height changes the early stage behaviour, but the duration remains the same. This varying rise behaviour at the initial stage can be understood by looking at the variation of the magnitude of the forces with time. The capillary force is constant over the entire duration, while the gravitational force as well as the viscous friction depends upon the height $\bar{h_a}(\bar{t})$, which decreases with time. Moreover, the viscous friction also depends upon the relative velocity $d(h_a + h_b)/dt$, which is initially zero, but slowly increases

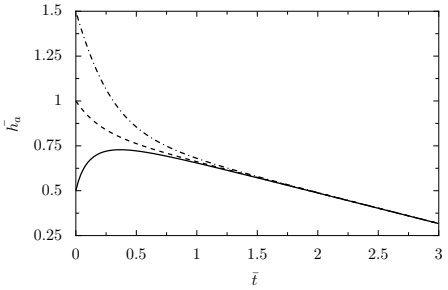

Figure 5.10: Effect of initial height on the temporal variation of the meniscus height.

with time.

At time $\bar{t} = 0$, setting $\bar{h_a} = 1$ implies that the starting height is the equilibrium height, where the capillary force and gravitational force are balanced. However, if it is anything other than one, it creates an imbalance right from the beginning. If $\bar{h_a}(\bar{t} = 0) < 1$, the capillary force is higher and it leads to the initial rise. But this initial rise does not reach h_o due to the increasing viscous friction. Similarly, if $\bar{h_a}(\bar{t} = 0) > 1$ the gravitational force is higher, it leads to the decreasing trend. Altogether, varying the initial height varies the magnitude of the two opposing forces which affects the early stage rise. But the variation of the meniscus height at long times, where it is linear, remains the same for all initial heights.

Effect of uncertainties in input parameters to the model Since the model requires input parameters, it is essential to know the effect of the uncertainties in these parameters on the model's prediction. The input parameters include the liquid properties (ρ, σ, μ), capillary size, contact angle and the motor speed. The effect of uncertainties in these parameters is characterized by calculating the speed of the meniscus height in the late stage, where it is linear. The speed here is also calculated by fitting the portion of the linear curve. Each input parameter was varied by 10% from its nominal value, while keeping the rest constant (at nominal values). Figure 5.11 shows the predicted speed by the model, at lowest and highest motor speeds used in the experiments for $w = 1$ mm. The uncertainty in the capillary size results in large deviation from the predicted speed at nominal values compared to other input parameters.

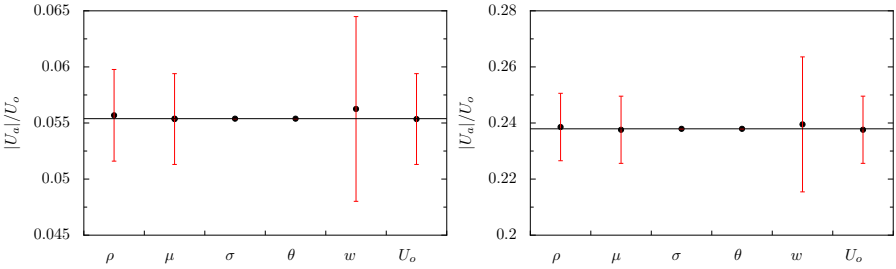

(a) $U_o = 0.2$ mm/s (b) $U_o = 1.32$ mm/s

Figure 5.11: Effect of uncertainties in the input parameters on the predicted speed in the late stage. The solid line represents the predicted speed calculated using nominal values for all the input parameters.

The roundedness of the corners increases the area of liquid contact with the wall, which results in increased resistance to the flow i.e., k increases. While the increase in the viscous friction parameter depending upon the degree of roundedness have been thoroughly examined in the context of corner flows [88, 91], the overall change in resistance k on the bulk flow is unknown. Although some experimental studies [59, 71], have calculated the mobility parameter from fitting the experimental data, the influence of the viscous friction coefficient cannot be ascertained. In addition to increasing the resistance, the roundedness of the corner also alters the effective capillary size, whose effect on the prediction was discussed above.

5.2.3 Comparison between experiments and model

Figure 5.12 compares the theoretical predictions for the temporal variation of the meniscus height with the experiments at for various sizes and speeds. There is an overall good agreement between the model and the experiment at all speeds. Note that no adjustable parameters have been used in the model. This agreement also confirms that the rivulets in the corner has no influence on the bulk flow even under forced wetting. The speed of the liquid column in the late stage is shown in Figure 5.13. The dashed line represents the predicted speed by the model calculated using nominal values. The shaded region represents the model's variation of

the speed by accounting for 10% uncertainty in the capillary size. The experimentally observed speeds fall within the region predicted by the model.

The variation of the predicted meniscus speed (using equation 5.9) with the capillary number is shown in Figure 5.14 for different Bond numbers. The capillary number based on the motor speed U_o is used as the parameter here instead of directly using U_o, since it emphasises the competition between the viscous drag (pulling the meniscus down) and the capillary force (pushing it up). The viscous friction coefficient is kept constant at 28.45. At very low capillary numbers ($Ca \leq 1 \times 10^{-4}$) the meniscus remains stationary (at its initial height), because the capillary force overcomes the viscous drag associated with the capillary immersion. The viscous drag starts to increase from $Ca > 1 \times 10^{-4}$, which results in the meniscus to descend at a steady speed. Increasing capillary number increases the meniscus speed. For $Bo \leq 0.01$, the variation of the meniscus speed with the capillary number is gradual, while at higher Bond numbers this variation becomes rapid reaching a meniscus speed, which thereafter remains nearly constant with Ca. The meniscus descends nearly at the immersion speed for $Bo = 1$ even at low capillary numbers ($Ca \geq 0.2$).

5.3 Summary

In this chapter, two forced wetting cases in square capillaries are studied using theory, experiments and numerical simulations. The long-time behaviour of the flow either in the bulk or in the rivulet under forced wetting is of the main interest.

In the first case, the forced wetting of rivulets is investigated using numerical simulations, where liquid is pumped into the capillary at a constant flow rate. The simulations show that the flow reaches steady state, where the meniscus attains a constant shape. The length of the rivulet steady state decreases with increasing capillary number, eventually resulting in air entrainment at $Ca \geq 0.15$. Increasing the capillary size increases the rivulet height, while increasing the contact angle decreases it, at a given capillary number. A theoretical solution for the rivulet profile is proposed using the lubrication approximation, which matches with the simulations for the rivulet profile close to the rivulet tip. The simulations also show that the apparent contact angles calculated from the meniscus

shapes follow Cox's law for all the capillary numbers studied.

In the second case, forced wetting by immersion of the capillary at a constant speed is studied. Experiments show that the bulk flow characterized by the meniscus height starts to descend shortly after the start of the immersion, at a steady speed. This capillary descent is modelled by extending the one-dimensional model for the capillary rise for the immersion. The model agrees with the experimental observations for the temporal variation of the meniscus height as well as for the constant meniscus speed observed at long times. Finally, the variation of the meniscus speed predicted by the model for different Bond numbers model is presented. The model predicts that the meniscus remains nearly stationary at very low capillary number ($Ca \leq 1 \times 10^{-4}$) and descends thereafter at a steady speed, which increases with the capillary number. With increasing Bond number, the variation of meniscus speed with the capillary number becomes rapid, which eventually becomes constant. At $Ca \geq 0.2$, the meniscus descends with the immersion speed for $Bo = 1$.

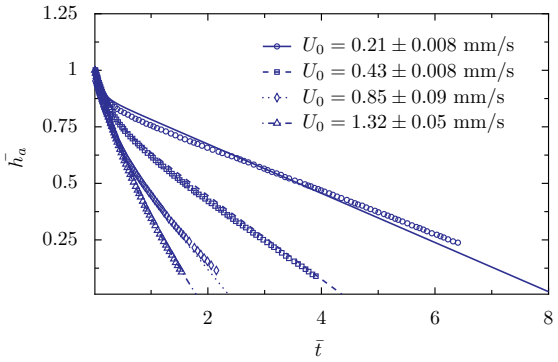

(a) $w = 0.7$ mm

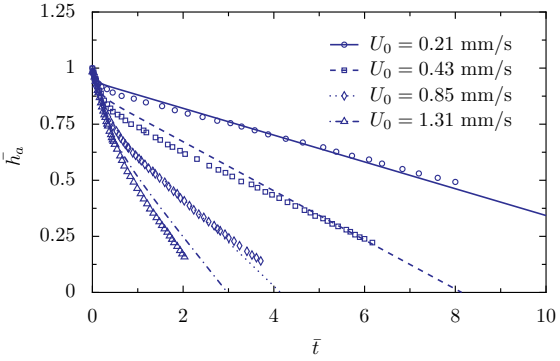

(b) $w = 1$ mm

Figure 5.12: Comparison between experiments and model (5.9) for the temporal variation of the meniscus height. The symbols represent the experiments and the lines represent the model.

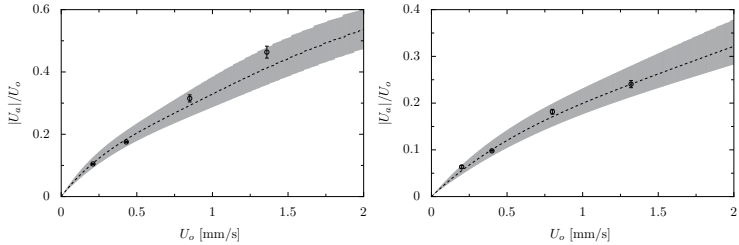

(a) $w = 0.7$ mm (b) $w = 1$ mm

Figure 5.13: Comparison between the theoretical predictions (5.9) and the experiments for the meniscus speed $|U_a|/U_o$ in the late stages. The dashed line represents the predicted speed by the model computed using nominal values to the input parameters. The shaded region represents the prediction by the model when the uncertainty in the capillary size is included.

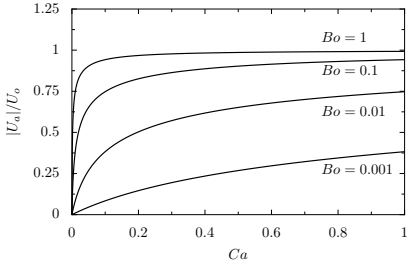

Figure 5.14: Variation of the predicted speed with the capillary number at different Bond numbers.

6 Summary and outlook

6.1 Summary

The objective of this thesis is to understand the dynamics of capillary driven flows in corners and their influence on the bulk flow. Accordingly, three studies focusing on the spontaneous and forced wetting in two model geometries were studied. The first two studies focused on the investigation of spontaneous rise in square capillaries and open rectangular channels. Forced wetting in square capillaries, focusing on the bulk flow and rivulet flow separately, was investigated in the final study.

The two model geometries studied in this work contains two types of corners: inner and outer. While rivulets are formed in the inner corner, the fluid near the outer corner forms a cusp. For the right-angled corners studied in the two model geometries, the condition for the formation of a rivulet in the inner corner and the formation of a cusp in the outer corner are the same, i.e., $\theta < 45°$. The condition for spontaneous rise in either capillary/open channel is $\theta < 90°$. So, the spontaneous rise in both the geometries includes both bulk flow and rivulet flow for $\theta < 45°$. The effect of various parameters on the flow in the two model geometries are characterized by using the meniscus height measured at different locations, and also by using the rivulet profile.

6.1.1 Spontaneous rise of rivulets in a square capillary

Numerical investigation of the spontaneous rise in the square capillary shows that the rise of rivulets can be split into two stages. In the early stage, the rise of rivulets is influenced by the bulk flow, since they share the same capillary pressure at the bulk meniscus. When the bulk flow enters the visco-gravitational regime during which it exponentially relaxes towards equilibrium, the rivulets start the transition towards the late stage i.e., pure corner flow. Shortly after the bulk flow reaches equilibrium, the rivulets enter the late stage, where it rises according to the one-third

asymptotic: $H \sim T^{1/3}$, which is also observed in open corners of different geometries.

Based on the theoretical analysis of the rivulet shape, three different regions are identified in the rivulet at late stages. The region close to the bulk meniscus, is complex and three-dimensional. It is followed by the intermediate region where the rivulet attains a near static shape. This static shape is described theoretically, which matches with simulations for the rivulet profile. Finally, the region close to the rivulet tip, where the flow was described using lubrication approximation, and a similarity solution was obtained by matching with the intermediate region. The thickness of the rivulet profile obtained from the solution matches with the computed profiles close to the tip, where it is valid. Based on the similarity solution, a scaling for the predicting the rate of rivulet growth is proposed. The dependence of the dimensionless growth rate K on the dimensionless initial rivulet thickness δ_o/a obtained from the numerical simulations shows that the function $K(\delta_o/a)$ is almost independent of the contact angle, liquid viscosity or surface tension. It also shows that the rivulet growth rate is weakly dependent on the geometry.

6.1.2 Spontaneous rise in open rectangular channels

The numerical investigation of the spontaneous rise in the open rectangular channel array describes the spontaneous rise inside the channel, on the outer face and also on the inner and outer corners. The effect of various parameters such as channel aspect ratio, outer face width and the contact angle on the spontaneous rise were studied.

The dynamics of the bulk flow inside the channel was compared with the one-dimensional capillary rise model, where a reasonable agreement between the two was observed at low contact angles. However, at higher contact angles and at shallow channel depths, the model underpredicts equilibrium height due to its assumption about the meniscus shape. The behaviour of the rivulets in the interior corner of the channel is the same as the one found in square capillaries. The one-third rise behaviour and the weak dependence on the geometry was also observed here.

The spontaneous rise of the liquid on the outer face connecting the channels is similar to the rise on an infinite planar wall. Moreover varying the outer face width has no influence on the both the bulk and the rivulet rise inside the channel.

The outer corner formed between the channel wall and the outer face have different capillary strengths on its either side. Surprisingly, it behaves as typical outer corner, when the forces on either side are nearly equal i.e, when the length scales are larger than the capillary length. A cusp is formed at the outer corner when $\theta < 45^\circ$ and a smooth meniscus otherwise [77]. But when the any one of the dimensions of either the channel or the outer face is smaller than the capillary length, a smooth meniscus is formed even when $\theta < 45^\circ$.

From this study, it can be concluded that the interactions between the flow inside the channel and the flow on the outer face were limited to altering the meniscus behaviour in the outer corner, in the sizes investigated.

6.1.3 Forced wetting in square capillaries

The dynamics of the bulk flow and the rivulet flow under forced wetting conditions were studied separately using two cases in a square capillary. In the first case, the forced wetting focusing on the rivulets in the corners was studied using numerical simulations. The simulations show that the rivulet reaches a fixed length at the steady state. This rivulet length decreases with the increasing capillary number. The flow inside the rivulet was modelled using lubrication approximation and a theoretical solution relating the rivulet thickness with the distance from the rivulet tip is proposed. The proposed solution matches with the rivulet profile close to the rivulet tip. The simulations also show that the apparent contact angle calculated from the meniscus shapes follow the Cox law at all the capillary numbers studied.

The immersion of the capillary at a constant speed was studied in the second case. Experiments were conducted for a range of speeds in two different capillary sizes. These experiments reveal that the bulk liquid starts descending at a steady speed shortly after the start of the immersion. This capillary immersion was modelled by extending the one-dimensional model originally derived for the capillary rise situation. The theoretical predictions by the model matches well with the experimental observations for both the meniscus height variation and its speed in the linear regime. Finally, the variation of the meniscus speed in the linear regime with the capillary number was predicted for different Bond numbers.

6.2 Outlook

Based on the results presented in this thesis, the following suggestions for future work are proposed.

- The algebraic VOF method used in this work is a promising tool to probe wetting in complicated geometries like textured surfaces. However, it still suffers from mesh dependency which needs to be addressed. The several mesh-dependent contact angle models proposed in the literature for other interface techniques should be extended for the algebraic VOF method.
- The possibility of applying the recently developed finite volume averaging method [144] to simulate the spontaneous rise of rivulets in polygonal capillaries should be explored. The main advantage of this technique over the traditional CFD techniques is that it reduces the computational cost involved significantly without losing the necessary information about the flow features.
- The proposed scaling relation for the rivulet growth rate in Chapter 3 implicitly depends upon the temporal variation of the rivulet height through the fitting factor. Thus it cannot be directly used to predict the rivulet rate in a given geometry. In order to predict the rivulet rate, an empirical correlation relating the rivulet rate with rivulet thickness should be developed. Using both experiments and simulations the rivulet rate must be determined in a wide range of geometries for building the correlation.
- In open channels of smaller sizes (of the order of microns), there is a possibility for the interactions between the flow inside the channel and the outer face to increase, which should be investigated. Also, these interactions should be studied under forced wetting conditions, which is important for applications such as dip coating.

A Grid convergence tests

Figures A.1 and A.2 show the temporal evolution of meniscus height measured in the center of the capillary, and inside the open channel for different mesh sizes. Despite the mesh-dependent results, the physical conclusions reported are independent of the mesh size. Differences in the final equilibrium height for different mesh sizes are shown in the Figure A.3, where the heights vary by no more than 5% within the mesh refinement.

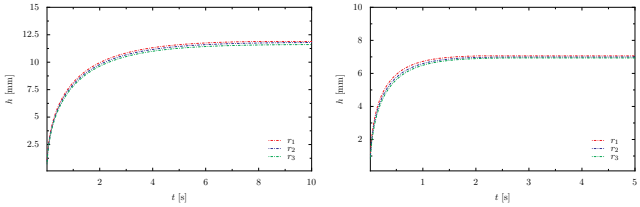

(a) $w = 0.6$ mm (b) $w = 1$ mm

(c) $w = 3$ mm (d) $w = 4.5$ mm

Figure A.1: Effect of mesh size on the temporal evolution of the meniscus height measured in the center of the square capillary. The contact angle is set at $\theta = 30°$. The variables r_1, r_2 and r_3 represent the different levels of refinement.

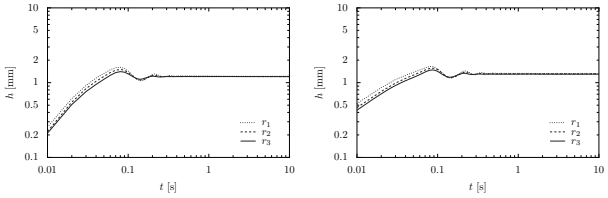

(a) $W = D = F = 3$ mm

(b) $D = 1.5$ mm

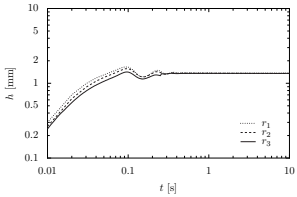

(c) $D = 0.75$ mm

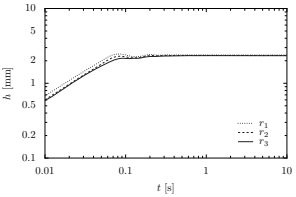

(d) $W = 1.5$ mm

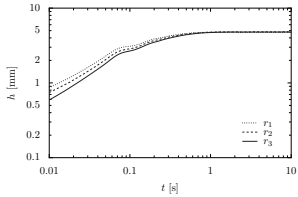

(e) $W = 0.75$ mm

Figure A.2: Effect of mesh size on the temporal evolution of the meniscus height measured in the center of the channel at $\theta = 30°$. The other dimensions were held constant at 3.00 mm in figures b-e. The variables r_1, r_2 and r_3 represent the different levels of refinement.

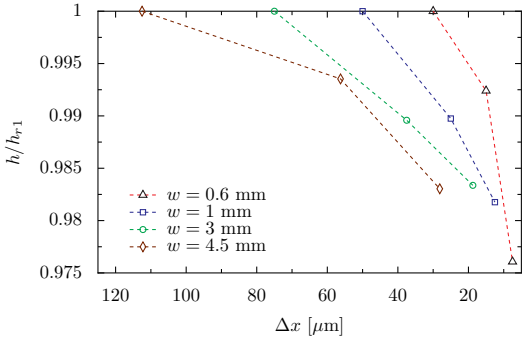

(a) Square capillary

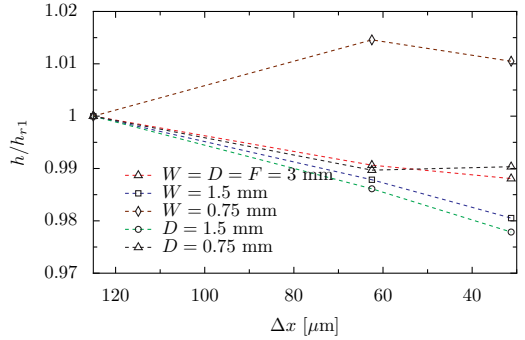

(b) Open channel

Figure A.3: Effect of mesh size on the equilibrium height of the meniscus measured in the center of capillary and inside the channel. The other dimensions were held constant at 3.00 mm. The equilibrium heights are normalized using the value h_{r1} in the coarsest mesh.

B Variation of the motor speed during immersion

When the translation stage is set to a constant speed during the immersion, the stage accelerates to the desired speed quickly at 5 mm/s^2. Even after achieving the desired speed, there are some slight variations in it, as seen in the Figure B.1. The nominal speed used in the model is calculated by taking the average of the speeds observed during the immersion. The solid line in the Figure B.1 represents the nominal speed.

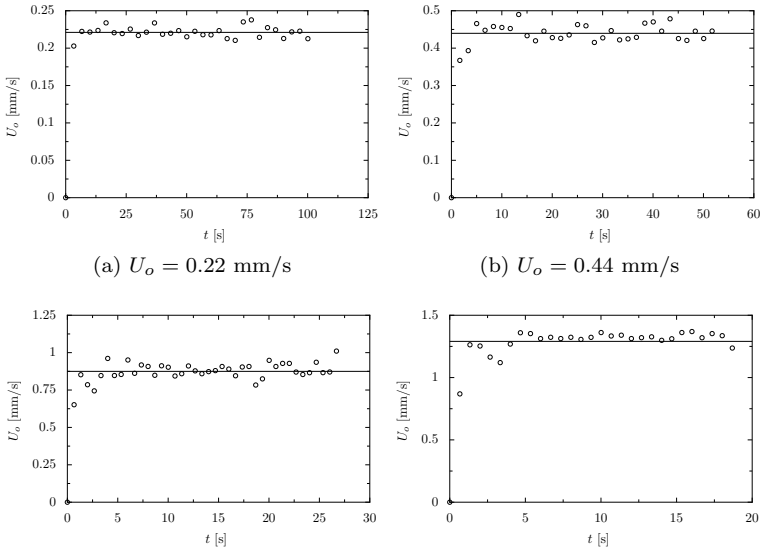

(a) $U_o = 0.22$ mm/s (b) $U_o = 0.44$ mm/s

(c) $U_o = 0.87$ mm/s (d) $U_o = 1.29$ mm/s

Figure B.1: Temporal variation of the motor speed in the translation stage during immersion. The solid line represents the average motor speed, which is represented as the nominal speed.

Bibliography

[1] T. M. Squires and S. R. Quake. Microfluidics: Fluid physics at the nanoliter scale. *Rev. Mod. Phys.*, 77:978–1016, 2005.

[2] K. W. Oh, K. Lee, B. Ahn, and E. P. Furlani. Design of pressure-driven microfluidic networks using electric circuit analogy. *Lab Chip*, 12(3):515–545, 2012.

[3] N. R. Morrow and G. Mason. Recovery of oil by spontaneous imbibition. *Curr. Opin. Colloid Interface Sci.*, 6(4):321–337, 2001.

[4] M. Piri and M. J. Blunt. Three-dimensional mixed-wet random pore-scale network modeling of two-and three-phase flow in porous media: I. model description. *Phys. Rev. E*, 71(2):026301, 2005.

[5] T. K. Tokunaga and J. Wan. Water film flow along fracture surfaces of porous rock. *Water Resour. Res.*, 33(6):1287–1295, 1997.

[6] A. G. Yiotis, A. G. Boudouvis, A. K. Stubos, I. N. Tsimpanogiannis, and Y. C. Yortsos. Effect of liquid films on the drying of porous media. *AIChE Journal*, 50(11):2721–2737, 2004.

[7] J. Schoelkopf, C. J. Ridgway, P. A. C. Gane, G. P. Matthews, and D. C. Spielmann. Measurement and network modeling of liquid permeation into compacted mineral blocks. *J. Colloid Interface Sci*, 227(1):119–131, 2000.

[8] J. Cen, R. Kitsomboonloha, and V. Subramanian. Cell filling in gravure printing for printed electronics. *Langmuir*, 30(45):13716–13726, nov 2014.

[9] C. Huh and L. E. Scriven. Hydrodynamic model of steady movement of a solid/liquid/fluid contact line. *J. Colloid Interface Sci.*, 35(1):85–101, 1971.

[10] D. Bonn, J. Eggers, J. Indekeu, J. Meunier, and E. Rolley. Wetting and spreading. *Reviews of Modern Physics*, pages 415–447, 2009.

[11] R. G. Cox. The dynamics of the spreading of liquids on a solid surface. Part 1. Viscous flow. *J. Fluid Mech.*, 168:169–194, 1986.

[12] R. G. Cox. The dynamics of the spreading of liquids on a solid surface. Part 2. Surfactants. *J. Fluid Mech.*, 168:195–220, 1986.

[13] E. Ramé, S. Garoff, and K. R. Willson. Characterizing the microscopic physics near moving contact lines using dynamic contact angle data. *Physical Review E - Statistical, Nonlinear, and Soft Matter Physics*, 70(3 1):1–9, 2004.

[14] O. V. Voinov. Hydrodynamics of wetting. *Fluid Dynamics*, 11(5):714–721, 1976.

[15] T. D. Blake and J. M. Haynes. Kinetics of liquid-liquid displacement. *J. Colloid Interface Sci.*, 30(3):421–423, 1969.

[16] T. D. Blake and J. De Coninck. The influence of solid-liquid interactions on dynamic wetting. *Adv. Colloid Interface Sci.*, 96(1-3):21–36, 2002.

[17] J. H. Snoeijer and B. Andreotti. Moving Contact Lines: Scales, regimes, and dynamical Transitions. *Annu. Rev. Fluid Mech.*, 45(1):269–292, 2013.

[18] P. Petrov and I. Petrov. A combined molecular-hydrodynamic approach to wetting kinetics. *Langmuir*, 8(11):1762–1767, 1992.

[19] M. J. de Ruijter, J. de Coninck, and G. Oshanin. Droplet spreading-partial wetting regime revisited. *Langmuir*, 15(20):2209–2216, 1999.

[20] R. L. Hoffman. A study of the advancing interface. I. Interface shape in liquid-gas systems. *J. Colloid Interface Sci.*, 50(2):228–241, 1975.

[21] T. S. Jiang, O. H. Soo-Gun, and J. C. Slattery. Correlation for dynamic contact angle. *J. Colloid Interface Sci.*, 69(1):74–77, 1979.

[22] S. F. Kistler. *Hydrodynamics of Wetting, in: John C. Berg (Ed.), Wettability.* Surfactant Science Series. Marcel Dekker, New York, 1993. p.311.

[23] P. G. de Gennes, F. Brochard-Wyart, and D. Quéré. *Capillarity and Wetting Phenomena.* Springer-Verlag New York, 2004.

[24] F. Hauksbee. Several experiments touching the seening spontaneous ascent of water. *Philos. Trans.*, 26:258–266, 1708.

[25] F. Hauksbee. An account of an experiment touching the ascent of water between two glass planes, in an hyperbolick. *Philos. Trans.*, 27:539–540, 1710.

[26] F. Hauksbee. An account of an experiment touching the direction of a drop of oil of oranges, between two glass planes, towards any side of them that is nearest pressed together. *Philos. Trans.*, 27:374–375, 1708.

[27] B. Taylor. Concerning the ascent of water between two glass plates. *Philos. Trans.*, 27(27):538, 1710.

[28] J. Jurin. An account of some experiments shown before the Royal Society; With an enquiry into the cause of the ascent and suspension of water in capillary tubes. *Phil. Trans.*, 30:739–747, 1718.

[29] I. Newton. *Opticks: or, A Treatise of the Reflexions, Refractions, Inflexions and Colours of Light*. William Innys, London, 1730.

[30] T. Young. An assay on the cohesion of fluids. *Philos. Trans.*, 95:65–87, 1805.

[31] P.S. de Laplace. *Supplément au livre X du Traitée de méchanique céleste*. Couvreier, Paris, 1806.

[32] J. W. Bullard and E. J. Garboczi. Capillary rise between planar surfaces. *Phys. Rev. E - Stat. Nonlinear, Soft Matter Phys.*, 79(1):4–10, 2009.

[33] J. Szekely, A. W. Neumann, and Y. K. Chuang. The rate of capillary penetration and the applicability of the washburn equation. *J. Colloid Interface Sci.*, 35(2):273–278, 1971.

[34] R. B. Bird, W. E. Stewart, and E. N. Lightfoot. *Transport Phenomena*. Wiley, New York, 1960. p.217.

[35] D. Quéré. Inertial capillarity. *Europhys. Lett.*, 39:533–538, 1997.

[36] D. Quéré. Rebounds in a capillary tube. *Langmuir*, 15:3679–3682, 1999.

[37] C. H. Bosanquet. On the flow of liquids into capillary tubes. *Philos.Mag*, 45(267):525–531, 1923.

[38] R. Lucas. Ueber das Zeitgesetz des kapillaren Aufstiegs von Flussigkeiten. *Kolloid-Zeitschrift*, 23(44):15–22, 1918.

[39] E. W. Washburn. The dynamics of capillary flow. *Phys. Rev.*, 17(3):273–283, 1921.

[40] E. K. Rideal. On the flow of liquids under capillary pressure. *Philos. Mag. Ser*, 6(44):1152–1159, 1922.

[41] B. Zhmud, F. Tiberg, and K. Hallstensson. Dynamics of capillary rise. *J. Colloid Interface Sci.*, 228(2):263–269, 2000.

[42] N. Fries and M. Dreyer. An analytic solution of capillary rise restrained by gravity. *J. Colloid Interface Sci.*, 320(1):259–63, apr 2008.

[43] S. Das, P. R. Waghmare, and S. K. Mitra. Early regimes of capillary filling. *Phys. Rev. E. Stat. Nonlin. Soft Matter Phys.*, 86(6 Pt 2):067301, dec 2012.

[44] S. Das and S. K. Mitra. Different regimes in vertical capillary filling. *Phys. Rev. E - Stat. Nonlinear, Soft Matter Phys.*, 87(6):1–7, 2013.

[45] A. Hamraoui, K. Thuresson, T. Nylander, and V. Yaminsky. Can a dynamic contact angle be understood in terms of a friction coefficient? *J. Colloid Interface Sci.*, 226(2):199–204, 2000.

[46] M. N. Popescu, J. Ralston, and R. Sedev. Capillary rise with velocity-dependent dynamic contact angle. *Langmuir*, 24(21):12710–12716, 2008.

[47] M. O'Loughlin, K. Wilk, C. Priest, J. Ralston, and M. N. Popescu. Capillary rise dynamics of aqueous glycerol solutions in glass capillaries: a critical examination of the Washburn equation. *J. Colloid Interface Sci.*, 411:257–64, dec 2013.

[48] R. Masoodi, E. Languri, and A. Ostadhossein. Dynamics of liquid rise in a vertical capillary tube. *J. Colloid Interface Sci.*, 389(1):268–72, jan 2013.

[49] R. P. Mayer and R. A. Stowe. Mercury porosimetry breakthrough pressure for penetration between packed spheres. *J. Colloid Sci.*, 20(8):893–911, 1965.

[50] H. M. Princen. Capillary phenomena in assemblies of parallel cylinders: I. Capillary rise between two cylinders. *J. Colloid Interface Sci.*, 30(3):359–371, 1968.

[51] H. M. Princen. Capillary phenomena in assemblies of parallel cylinders: II. Capillary rise in systems with more than two cylinders. *J. Colloid Interface Sci.*, 30(3):359–371, 1969.

[52] H. M. Princen. Capillary phenomena in assemblies of parallel cylinders: III. Liquid columns between horizontal parallel cylinders. *J. Colloid Interface Sci.*, 30(3):359–371, 1970.

[53] G. Mason and N. R. Morrow. Meniscus curvatures in capillaries of uniform cross-section. *J. Chem. Soc. Faraday Trans. 1 Phys. Chem. Condens. Phases*, 80(9):2375, 1984.

[54] J. Bico and D. Quéré. Rise of liquids and bubbles in angular capillary tubes. *J. Colloid Interface Sci.*, 247(1):162–166, 2002.

[55] P. Wu, H. Zhang, A. Nikolov, and D. Wasan. Rise of the main meniscus in rectangular capillaries: Experiments and modeling. *J. Colloid Interface Sci.*, 461:195–202, jan 2016.

[56] G. Mason. Capillary behaviour of a perfectly wetting liquid in irregular triangular tubes. *J. Colloid Sci.*, 141(1), 1991.

[57] L. Ronald Panton. *Incompressible Flow.* John Wiley and Sons Ltd., 1996.

[58] N. Ichikawa, K. Hosokawa, and R. Maeda. Interface motion of capillary-driven flow in rectangular microchannel. *J. Colloid Interface Sci.*, 280(1):155–164, 2004.

[59] F. F. Ouali, G. McHale, H. Javed, C. Trabi, N. J. Shirtcliffe, and M. I. Newton. Wetting considerations in capillary rise and imbibition in closed square tubes and open rectangular cross-section channels. *Microfluid. Nanofluidics*, 15(3):309–326, feb 2013.

[60] S. W. Tchikanda, R. H. Nilson, and S. K. Griffiths. Modeling of pressure and shear-driven flows in open rectangular microchannels. *Int. J. Heat Mass Transf.*, 47(3):527–538, 2004.

[61] R. H. Nilson, S. W. Tchikanda, S. K. Griffiths, and M. J. Martinez. Steady evaporating flow in rectangular microchannels. *Int. J. Heat Mass Transf.*, 49(9-10):1603–1618, 2006.

[62] W. Zheng, L. P. Wang, D. Or, V. Lazouskaya, and Y. Jin. Role of mixed boundaries on flow in open capillary channels with curved air water interfaces. *Langmuir*, 28(35):12753–12761, 2012.

[63] I. Catton and G. R. Stroes. A semi-analytical model to predict the capillary limit of heated inclined triangular capillary grooves. *J. Heat Transfer*, 124(1):162, 2002.

[64] S. K. Thomas, R. C. Lykins, and K. L. Yerkes. Fully developed laminar flow in trapezoidal grooves with shear stress at the liquid-vapor interface. *Int. J. Heat Mass Transf.*, 44:3397–3412, 2001.

[65] J. Suh, R. Greif, and C. P. Grigoropoulos. Friction in micro-channel flows of a liquid and vapor in trapezoidal and sinusoidal grooves. *Int. J. Heat Mass Transf.*, 44:3103–3109, 2001.

[66] R. R. Rye, J. A. Mann, and F. G. Yost. The flow of liquids in surface grooves. *Langmuir*, 12(2):555–565, jan 1996.

[67] R. R. Rye, F. G. Yost, and E. J. O'Toole. Capillary flow in irregular surface grooves. *Langmuir*, 14(14):3937–3943, 1998.

[68] L. A. Romero and F. G. Yost. Flow in an open channel capillary. *J. Fluid Mech.*, 322(-1):109, apr 1996.

[69] J. Berthier, K. A. Brakke, E. P. Furlani, I. H. Karampelas, V. Poher, D. Gosselin, M. Cubizolles, and P. Pouteau. Whole blood spontaneous capillary flow in narrow V-groove microchannels. *Sensors Actuators B Chem.*, 206:258–267, jan 2015.

[70] Y. Liu, A. Hansen, E. Block, N. R. Morrow, J. Squier, and J. Oakey. Two-phase displacements in microchannels of triangular cross-section. *J. Colloid Interface Sci.*, 507:234–241, 2017.

[71] D. Yang, M. Krasowska, C. Priest, M. N. Popescu, and J. Ralston. Dynamics of capillary-driven flow in open microchannels. *J. Phys. Chem. C*, 115(38):18761–18769, sep 2011.

[72] T. W. Sowers, R. Sarkar, S. E. Prameela, E. Izadi, and J. Rajagopalan. Capillary driven flow of polydimethylsiloxane in open rectangular microchannels. *Soft Matter*, 12(12):5818–5823, 2016.

[73] R. K. Lade, E. J. Hippchen, C. W. Macosko, and L. F. Francis. Dynamics of capillary-driven flow in 3D printed open microchannels. *Langmuir*, 33(12):2949–2964, 2017.

[74] D. Deng, Y. Tang, J. Zeng, S. Yang, and H. Shao. Characterization of capillary rise dynamics in parallel micro V-grooves. *Int. J. Heat Mass Transf.*, 77:311–320, oct 2014.

[75] P. J. Ponce de Leon and L. F. Velásquez-García. Optimization of capillary flow through open-microchannel and open-micropillar arrays. *J. Phys. D. Appl. Phys.*, 49(5):055501, 2016.

[76] P. Concus and R. Finn. On the behavior of a capillary surface in a wedge. *Appl. Math. Sci.*, 63(2):292–299, 1969.

[77] M. M. Alimov and K. G. Kornev. Singularities of Meniscus at the V-shaped Edge. *Mech. Res. Commun.*, 62:162–167, 2014.

[78] Kenneth A. Brakke. Minimal surfaces, corners, and wires. *The Journal of Geometric Analysis*, 2(1):11–36, Jan 1992.

[79] F. Chauvet, P. Duru, and M. Prat. Depinning of evaporating liquid films in square capillary tubes: Influence of corners' roundedness. *Phys. Fluids*, 22(11), 2010.

[80] A. de Ramos and R. L. Cerro. Liquid filament rise in comers of square capillaries: a novel method for the measurement of small contact angles. *Chem. Eng. Sci.*, 49(14):2395–2398, 1994.

[81] S. Girardo, R. Cingolani, S. Chibbaro, F. Diotallevi, S. Succi, and D. Pisignano. Corner liquid imbibition during capillary penetration in lithographically made microchannels. *Appl. Phys. Lett.*, 94(17):2007–2010, 2009.

[82] D. Yang, M. Krasowska, C. Priest, and J. Ralston. Dynamics of capillary-driven liquid-liquid displacement in open microchannels. *Phys. Chem. Chem. Phys.*, 16(44):24473–24478, 2014.

[83] J. Feng and J. P. Rothstein. Simulations of novel nanostructures formed by capillary effects in lithography. *J. Colloid Interface Sci.*, 354(1):386–395, 2011.

[84] A. Singhal and W. Somerton. Two-phase flow through a non-circular capillary at low Reynolds numbers. *J. Can. Pet. Technol.*, 1970.

[85] P. S. Ayyaswamy, I. Catton, and D. K. Edwards. Capillary flow in triangular grooves. *J. Appl. Mech.*, pages 332–336, 1974.

[86] R. Lenormand and C. Zarcone. Role of roughness and edges during imbibition in square capillaries. In *SPE-13264-MS*. Society of Petroleum Engineers, 1984.

[87] H. B. Ma, G. P. Peterson, and X. J. Lu. The influence of vapor-liquid interactions on the liquid pressure drop in triangular microgrooves. *Int. J. Heat Mass Transf.*, 37(15):2211–2219, 1994.

[88] T. C. Ranshoff and C. J. Radke. Laminar flow of a wetting liquid along the corners of a predominantly gas-occupied noncircular pore. *J. Colloid Interface Sci.*, 121, 1988.

[89] M. M. Weislogel and S. Lichter. Capillary flow in an interior corner. *J. Fluid Mech.*, 373:349–378, 1998.

[90] M. Dong and I. Chatzis. The imbibtion and flow of a wetting liquid along the corners of a square capillary Tube. *J. Colloid Interface Sci.*, 172:278–288, 1995.

[91] Y. Chen, M. M. Weislogel, and C. L. Nardin. Capillary-driven flows along rounded interior corners. *J. Fluid Mech.*, 566:235, 2006.

[92] M. M. Weislogel, J. A. Baker, and R. M. Jenson. Quasi-steady capillarity-driven flows in slender containers with interior edges. *J. Fluid Mech.*, 685:271–305, sep 2011.

[93] L. H. Tang and Y. Tang. Capillary rise in tubes with sharp grooves. *J. Phys. II*, 4:881–890, 1994.

[94] F. J. Higuera, A. Medina, and A. Liñán. Capillary rise of a liquid between two vertical plates making a small angle. *Phys. Fluids*, 20(10):102102, 2008.

[95] A. Ponomarenko, D. Quéré, and C. Clanet. A universal law for capillary rise in corners. *J. Fluid Mech.*, 666:146–154, jan 2011.

[96] J. Lowndes. The numerical simulation of the steady movement of a fluid meniscus in a capillary tube. *J. Fluid Mech.*, 101:631–646, 1980.

[97] I. B. Bazhlekov and A. K. Chesters. Numerical investigation of the dynamic influence of the contact line region on the macroscopic meniscus shape. *J. Fluid Mech.*, 329:137–146, 1996.

[98] F. G. Wolf, L. O. E. dos Santos, and P. C. Philippi. Capillary rise between parallel plates under dynamic conditions. *J. Colloid Interface Sci.*, 344(1):171–9, apr 2010.

[99] Y. Yamamoto, T. Ito, T. Wakimoto, and K. Katoh. Numerical simulations of spontaneous capillary rises with very low capillary numbers using a front-tracking method combined with generalized Navier boundary condition. *Int. J. Multiph. Flow*, 51:22–32, may 2013.

[100] G. Lu, X. D. Wang, and Y. Y. Duan. Study on initial stage of capillary rise dynamics. *Colloids Surfaces A Physicochem. Eng. Asp.*, 433:95–103, sep 2013.

[101] S. Girardo, S. Palpacelli, A. De Maio, R. Cingolani, S. Succi, and D. Pisignano. Interplay between shape and roughness in early-stage microcapillary imbibition. *Langmuir*, 28(5):2596–2603, feb 2012.

[102] R. Seemann, M. Brinkmann, E. J. Kramer, F. F. Lange, and R. Lipowsky. Wetting morphologies at microstructured surfaces. *Proceedings of the National Academy of Sciences*, 102(6):1848–1852, 2005.

[103] K. Khare, S. Herminghaus, J. C. Baret, B. M. Law, M. Brinkmann, and R. Seemann. Switching liquid morphologies on linear grooves. *Langmuir*, 23(26):12997–13006, 2007.

[104] S. Son, L. Chen, Q. Kang, D. Derome, and J. Carmeliet. Contact angle effects on pore and corner arc menisci in polygonal capillary tubes studied with the pseudopotential multiphase lattice boltzmann model. *Computation*, 4(1):12, 2016.

[105] H.G. Weller. A new approach to vof-based interface capturing methods for incompressible and compressible flow. Technical Report 04, OpenCFD Ltd, 2008.

[106] J. U. Brackbill, D. B. Kothe, and Zemach C. A continuum method for modeling surface tension. *J. Comput. Phys.*, 100(2):335 – 354, 1992.

[107] C. Kunkelmann. *Numerical modeling and investigation of boiling phenomena*. PhD thesis, Technische Universität Darmstadt, 2011.

[108] S. Batzdorf. *Heat transfer and evaporation during single drop impingement onto a superheated wall*. PhD thesis, Technische Universität Darmstadt, 2015.

[109] J. E. Pilliod and E. G. Puckett. Second-order accurate volume-of-fluid algorithms for tracking material interfaces. *J. Comput. Phys.*, 199(2):465 – 502, 2004.

[110] F. Y. Kafka and E. B. Dussan. On the interpretation of dynamic contact angles in capillaries. *J. Fluid Mech.*, 95(03):539, 1979.

[111] N. Linder, I. V. Criscione, A.and Roisman, H. Marschall, and C. Tropea. 3D computation of an incipient motion of a sessile drop on a rigid surface with contact angle hysteresis. *Theor. Comput. Fluid Dyn.*, 29(5-6):373–390, 2015.

[112] J. A. Moriarty and L. W. Schwartz. Effective slip in numerical calculations of moving-contact-line problems. *J. Eng. Math.*, 26(1):81–86, 1992.

[113] O. Weinstein and L. M. Pismen. Scale dependence of contact line computations. *Math. Model. Nat. Phenom.*, 3(1):98–107, 2008.

[114] L. M. Hocking. Sliding and spreading of thin 2D drops. *Q. J. Mech. Appl. Math.*, 34(January 1980):37–55, 1981.

[115] M. Renardy, Y. Renardy, and J. Li. Numerical simulation of moving contact line problems using a volume-of-fluid method. *J. Comput. Phys.*, 171(1):243–263, 2001.

[116] J. B. Dupont and D. Legendre. Numerical simulation of static and sliding drop with contact angle hysteresis. *J. Comput. Phys.*, 229(7):2453–2478, 2010.

[117] Yi Sui and Peter D. M. Spelt. Validation and modification of asymptotic analysis of slow and rapid droplet spreading by numerical simulation. *J. Fluid Mech.*, 715:283–313, 2013.

[118] S. Afkhami, S. Zaleski, and M. Bussmann. A mesh-dependent model for applying dynamic contact angles to VOF simulations. *J. Comput. Phys.*, 228(15):5370–5389, 2009.

[119] P. Sheng and M. Zhou. Immiscible-fluid displacement: Contact-line dynamics and the velocity-dependent capillary pressure. *Phys. Rev. A*, 45(8):5694–5708, 1992.

[120] D. Legendre and M. Maglio. Comparison between numerical models for the simulation of moving contact lines. *Comput. Fluids*, 113:2–13, 2014.

[121] Y. Sui and P. D. M. Spelt. An efficient computational model for macroscale simulations of moving contact lines. *J. Comput. Phys.*, 242:37–52, 2013.

[122] R. G. COX. Inertial and viscous effects on dynamic contact angles. *J. Fluid Mech.*, 357:S0022112097008112, 1998.

[123] F. Schönfeld and S. Hardt. Dynamic contact angles in CFD simulations. *Comput. Fluids*, 38(4):757–764, 2009.

[124] Hrvoje Jasak, Aleksandar Jemcov, and Zeljko Tukovic. Openfoam: A C++ library for complex physics simulations. In *Int. Workshop on Coupled Methods in Numerical Dynamics*, volume 1000, pages 1–20, Dubrovnik, Croatia, September 2007. IUC Dubrovnik, Croatia.

[125] Open∇Foam. the open source cfd toolbox. https://www.openfoam.com/.

[126] H. Jasak. *Error analysis and estimation for the finite volume method with applications to fluid Flows.* PhD thesis, Imperial College of Science, Technology and Medicine, 1996.

[127] H. Rusche. *Computational fluid dynamics of dispersed two-phase flows at high phase fractions.* PhD thesis, Imperial College of Science, Technology and Medicine, 2002.

[128] D. Santiago Márquez. *An extended mixture model for the simultaneous treatment of short and long scale interfaces.* PhD thesis, Universidata Nacional Del Litoral, 2013.

[129] R.I. Issa. Solution of the implicitly discretised fluid flow equations by operator-splitting. *J. Comput. Phys.*, 62(1):40 – 65, 1986.

[130] M. M. Weislogel. Compound capillary rise. *J. Fluid Mech.*, 709:622–647, oct 2012.

[131] N. Fries and M. Dreyer. The transition from inertial to viscous flow in capillary rise. *J. Colloid Interface Sci.*, 327(1):125–8, nov 2008.

[132] M. M. Weislogel. Some analytical tools for fluids management in space: Isothermal capillary flows along interior corners. *Adv. Sp. Res.*, 32(2):163–170, 2003.

[133] M. Tani, R. Kawano, K. Kamiya, and K. Okumura. Towards combinatorial mixing devices without any pumps by open-capillary channels: fundamentals and applications. *Sci. Rep.*, 5(October 2014):10263, 2015.

[134] V. T. Gurumurthy, I. V. Roisman, C. Tropea, and S. Garoff. Spontaneous rise in open rectangular channels under gravity. *J. Colloid Interface Sci.*, 527:151–158, 2018.

[135] C. Clanet and D. Quéré. Onset of menisci. *J. Fluid Mech.*, 460:131–149, 2002.

[136] D. Okiely, J. P. Whiteley, J. M. Oliver, and D. Vella. Inertial rise of a meniscus on a vertical cylinder. *J. Fluid Mech.*, 768:R2, 2015.

[137] R. J. Hansen and T. Y. Toong. Interface behavior as one fluid completely displaces another from a small-diameter tube. *J. Colloid Interface Sci.*, 36(3):410–413, 1971.

[138] M. Bracke, F. Voeght, and P. Joos. The kinetics of wetting: the dynamic contact angle. *Trends Colloid Interface Sci. III*, 149:142–149, 1989.

[139] J. E. Seebergh and J. C. Berg. Dynamic wetting in the low capillary number regime. *Chem. Eng. Sci.*, 47(17-18):4455–4464, 1992.

[140] M. Fermigier and P. Jenffer. An experimental investigation of the dynamic contact angle in liquid-liquid systems. *J. Colloid Interface Sci.*, 146(1):226–241, 1991.

[141] W. Boender, A. K. Chesters, and A. J. van der Zanden. An approximate solution of the hydrodynamic problem associated with receding liquid-gas contact lines. *Int. J. Multiph. Flow*, 17(5):661–676, 1991.

[142] Y. Sui and Peter D. M. Spelt. Sustained inertial-capillary oscillations and jet formation in displacement flow in a tube. *Phys. Fluids*, 23(12), 2011.

[143] S. Girardo, S. Palpacelli, A. De Maio, R. Cingolani, S. Succi, and D. Pisignano. Interplay between shape and roughness in early-stage microcapillary imbibition. *Langmuir*, 28(5):2596–2603, 2012.

[144] A. Yelkhovsky and W. V. Pinczewski. Finite volume solution for two-phase flow in a straight capillary. *Phys. Rev. Fluids*, 044003:1–15, 2018.

List of Figures

List of Tables